

Hydraulic characterization of fractured and porous aquifers by induced polarization and hydraulic tomography

Dissertation

**zur Erlangung des
Doktorgrades der Naturwissenschaften (Dr. rer. nat.)**

der

Naturwissenschaftlichen Fakultät III
Agrar- und Ernährungswissenschaften,
Geowissenschaften und Informatik
der Martin-Luther-Universität Halle-Wittenberg

vorgelegt von

Lukas Römhild



Tag der Verteidigung:

16. Oktober 2024

Deutscher Titel:

*Hydraulische Charakterisierung von geklüfteten und porösen Grundwasserleitern
mittels Induzierter Polarisierung und Hydraulischer Tomographie*

Gutachter:

Prof. Dr. Peter Bayer

Prof. Dr. Matthias Bucker

Abstract

The accurate characterization of aquifer heterogeneities in terms of hydraulic parameters is an essential precondition for groundwater modeling tasks. Therefore, a reliable prediction of flow and transport processes at a given site strongly depends on the accuracy of conducted field experiments, and likewise on the robustness of the available data processing and inversion techniques to derive the hydraulic conductivity K and its structural features at different scales. This thesis develops several new inversion approaches that allow inferring a K -distribution based on induced polarization (IP) and/or hydraulic tomography (HT) data.

Geophysical methods are considered appealing for performing such imaging tasks due to their great efficiency in the field. In particular, IP has frequently been used to infer hydraulic parameters in situ. Based on the conceptual similarities between groundwater flow and electrical conduction processes, various petrophysical relations between IP parameters and hydraulic properties have been derived from laboratory experiments. They can be used to estimate K , typically within unconsolidated sediments. In a novel approach, these petrophysical laws are directly incorporated into an IP inversion procedure, so that the spatial distribution of K is a straight result of the inversion, and no additional processing steps are required. The new method is implemented and tested synthetically on an aquifer analog data set, revealing that structural features can be reconstructed with high resolution and accuracy, and that the K -estimates are reliable, especially when being calibrated with measured hydraulic data. This is underlined by performing synthetic transport modeling experiments, where using the IP inversion results yields tracer plumes that are comparable with those derived from the original data set. The results highlight the great potential of the IP method for providing hydraulic information relevant to groundwater modeling tasks.

However, K -estimates based on geophysical data always bear a significant amount of uncertainty due to the approximative character of the petrophysical relations and their dependency on specific assumptions for the geological setting. In contrast, hydraulic methods, such as HT, test for the hydraulic parameters directly, and are

therefore more reliable for K -quantification. Performing a travel time inversion of HT data is an easy and computationally efficient approach for processing hydraulic information. Therefore, it serves as a reference point for comparing results from new inversion methods throughout this thesis.

Since the classical travel time approach is based on continuum models, it is often not suitable for fractured rock. In such cases, discrete fracture network (DFN) models can be used to infer individual fractures from the HT data. However, in some rock types, both fracture and matrix flow are hydraulically relevant and should be considered. To combine the two model assumptions, a hybrid DFN inversion is developed that accounts for groundwater flow through the matrix and individual fractures. The new approach is tested on a field data set from a fractured-porous site in Göttingen, Germany. It is shown that the experimental data are fitted more precisely by the hybrid DFN inversion compared to a purely fracture-based approach and to a travel time inversion. Furthermore, the subsurface model based on the hybrid approach is more suitable to predict heat tracer tests that have also been conducted at the site.

In the final step, a joint inversion for IP and HT is implemented, which allows for computing a common K -distribution that is supported equally by both data types. The proposed approach leverages the complementary strengths of both methods in terms of sensitivity distribution, practically achievable spatial resolution, and reliability of K -estimates. The joint inversion approach utilizes the aforementioned IP- K inversion, as well as a travel time approach for the HT data. It is tested on a horizontally layered synthetic model case to illustrate the potential of jointly inverting the data, and the advantages compared to individual inversions. In addition, it is shown how petrophysical uncertainties contained in the IP data can be corrected automatically by including the typically more reliable K -estimates from HT.

All new inversion methods developed in this thesis facilitate a more accurate characterization of aquifer heterogeneities, i.e., high resolution imaging of hydraulic conductivity K . However, the specific field method, the acquisition setup of the experiments, and the actual data processing and inversion techniques always have to be chosen carefully based on the geological setting. Future research should thus focus on applying the new inversion methodologies to more field cases to enhance the experience regarding the applicability to certain in situ conditions. Ultimately, the combined application of geophysical and hydraulic methods is an important step towards more reliable groundwater modeling results, leading to a better understanding and prediction of flow and transport processes.

Zusammenfassung

Die genaue Charakterisierung von Aquiferheterogenitäten hinsichtlich hydraulischer Parameter ist eine wichtige Voraussetzung für Grundwassermodellierungsaufgaben. Dabei hängt eine verlässliche Vorhersage der Fließ- und Transportprozesse an einem Standort enorm von der Robustheit der verfügbaren Datenprozessierungs- und Inversionstechniken für die genutzten Aquifercharakterisierungsmethoden ab. Im Rahmen dieser Arbeit werden daher verschiedene neue Inversionsansätze entwickelt, welche die Berechnung der hydraulischen Leitfähigkeit K aus Messungen der Induzierten Polarisation (IP) und/oder Hydraulischer Tomographie (HT) erlauben.

Geophysikalische Methoden gelten aufgrund ihrer Effizienz in der Feldanwendung als vielversprechend für die in-situ-Bestimmung hydraulischer Parameter. Auf Grundlage der konzeptionellen Ähnlichkeiten von Grundwasserfließ- und elektrischen Leitfähigkeitsprozessen konnte mittels Laborexperimenten bereits eine Vielzahl petrophysikalischer Zusammenhänge zwischen IP-Parametern und hydraulischen Eigenschaften hergeleitet werden, die für die K -Abschätzung insbesondere in Lockersedimenten Anwendung finden. Diese Gesetzmäßigkeiten werden nun direkt in die IP-Inversion integriert, sodass die K -Verteilung ein direktes Inversionsergebnis ist und keine zusätzlichen Prozessierungsschritte notwendig sind. Die Methode wird für einen Aquiferanalog-Datensatz implementiert und mittels synthetisch erzeugter Messdaten getestet. Dabei kann eine hochaufgelöste Rekonstruktion der Strukturelemente erreicht werden und die K -Abschätzung ist insbesondere dann zuverlässig, wenn eine Kalibrierung mit hydraulischen Daten erfolgt. Dies wird durch synthetische Transportmodellierungsexperimente unterstrichen, bei denen die IP-Inversionsergebnisse Tracerdurchbrüche korrekt vorhersagen.

Allerdings sind die K -Schätzungen aus geophysikalischen Daten stets jenen Unsicherheiten unterworfen, die aus dem approximativen Charakter der petrophysikalischen Zusammenhänge sowie aus deren eingeschränkter Anwendbarkeit für spezifische Standortbedingungen erwachsen. Im Gegensatz dazu können pumpetestbasierte Methoden die hydraulischen Parameter auf direktere Weise herleiten, sodass die K -Quantifizierung oft zuverlässiger ist. Für die Nutzung von HT-Daten ist die Lauf-

zeitinversion ein beliebter, weil rechenzeiteffizienter Ansatz, der daher im Rahmen dieser Arbeit als Referenz zur Bewertung weiterer Ergebnisse herangezogen wird.

Da klassische laufzeitbasierte Inversionen jedoch auf Kontinuumsmodellen beruhen, sind sie für geklüftete Gesteine meist unzureichend. Stattdessen sollten *discrete fracture networks* (DFNs) verwendet werden, um ein Netzwerk diskreter Klüfte aus den HT-Daten abzuleiten. In einigen Materialien sind allerdings sowohl Einzelklüfte als auch die Gesteinsmatrix hydraulisch relevant. Um beide Modellannahmen zu verbinden, wird eine hybride DFN-Inversion entwickelt, die Fließprozesse durch die Matrix und durch Einzelklüfte berücksichtigt. Dieser neue Ansatz wird an HT-Felddaten getestet, die an einem porös-geklüfteten Standort in Göttingen gewonnen wurden. Dabei wird mit dem hybriden Ansatz ein verbesserter Datenfit im Vergleich zu klassischer DFN- und zur Laufzeitinversion erreicht. Das Untergrundmodell aus der hybriden DFN-Inversion eignet sich zudem besser für die Modellierung von ebenfalls am Standort durchgeführten Wärmetransportversuchen.

Den Schlusspunkt der Arbeit bildet die Implementierung einer *Joint Inversion* für IP und HT, welche die Berechnung einer durch beide Datentypen gleichermaßen gestützten K -Verteilung erlaubt. Das Konzept fußt auf den komplementären Eigenschaften der beiden Methoden bezüglich Sensitivitätsverteilungen, räumlichem Auflösungsvermögen und der Verlässlichkeit der K -Abschätzung. Die Implementierung der *Joint Inversion* basiert auf dem o.g. IP- K Inversionsansatz sowie der laufzeitbasierten HT-Inversion. Diese Methodik wird an einem synthetischen Beispielmmodell getestet und mit den entsprechenden Einzelinversionen verglichen. Außerdem wird gezeigt, dass die aus den petrophysikalischen Annahmen resultierenden Unsicherheiten automatisch durch die Einbeziehung verlässlicherer HT-basierter K -Abschätzungen korrigiert werden.

Die im Rahmen dieser Arbeit entwickelten Inversionsansätze erlauben somit eine genauere und verlässlichere Charakterisierung von Aquiferheterogenitäten. Jedoch muss die Auswahl der im jeweiligen Fall geeigneten Methoden, Akquisitionsgemetrien und Datenprozessierungs- und Inversionstechniken stets mit Bedacht und im Hinblick auf das vorliegende geologische Setting erfolgen. Künftige Forschungsaktivitäten sollten sich daher vor allem mit der Anwendung der neuen Inversionstechniken auf verschiedenartige Feldbeispiele beschäftigen, um den Erfahrungshorizont bezüglich der Anwendbarkeit der Methoden in bestimmten geologischen Kontexten zu erweitern. Letztlich kann die kombinierte Anwendung geophysikalischer und hydraulischer Methoden zu mehr Verlässlichkeit bei der Grundwassermodellierung und einem besseren Verständnis von Fließ- und Transportprozessen beitragen.

Contents

Abstract	I
Zusammenfassung	III
Glossary	IX
List of Figures	XI
Publications	XIII
Aims and Objectives	1
1.1 Introduction	2
1.2 Induced polarization methods for estimating hydraulic conductivity .	3
1.2.1 Models for the IP effect	4
1.2.2 Petrophysical relations for K-estimation from IP data	7
1.3 Hydraulic tomography at porous and fractured sites	9
1.3.1 Continuum-based modeling approaches	9
1.3.2 Fracture-based modeling approaches	11
1.4 Inverse problems	13
1.4.1 Mathematical background	13
1.4.2 Joint inversion	15
Imaging hydraulic conductivity in near-surface aquifers by complementing cross-borehole induced polarization with hydraulic experiments. Römhild, L., Fiandaca, G., Hu, L., Meyer, L. and Bayer, P. - Advances in Water Resources, 170: 104322 (2022)	17
2.1 Introduction	19
2.2 Materials and Methods	21
2.2.1 Bolstern aquifer analog	22
2.2.2 Induced Polarization	25
2.2.3 Hydraulic Tomography	33

2.2.4	Tracer Experiments	36
2.3	Results	36
2.3.1	HT and IP Inversion Results	36
2.3.2	Transport Simulation	41
2.4	Conclusions	46
Hybrid discrete fracture network inversion of hydraulic tomography data from a fractured-porous field site. Römhild, L., Ringel, L.M., Liu, Q., Hu, L., Ptak, T. and Bayer, P. - Water Resources Research 60: e2023WR036035 (2024)		49
3.1	Introduction	51
3.2	Methods	53
3.2.1	Site description and data acquisition	53
3.2.2	Continuum-based travel time inversion	55
3.2.3	Hybrid DFN inversion	56
3.3	Inversion results	60
3.3.1	Travel time inversion result	60
3.3.2	Hybrid DFN inversion results: individual realizations	62
3.3.3	Hybrid DFN inversion results: fracture probability map	63
3.3.4	Influence of matrix characteristics	65
3.4	Validation with thermal tracer test data	67
3.4.1	Field experiments	67
3.4.2	Simulation of the field experiments	67
3.4.3	Comparison between measured and predicted thermal response	68
3.5	Discussion	72
3.6	Conclusions and Outlook	75
Joint inversion of induced polarization and hydraulic tomography data for hydraulic conductivity imaging. Römhild, L., Fiandaca, G. and Bayer, P. - Geophysical Journal International 238(2): 960–973 (2024)		77
4.1	Introduction	79
4.2	Methods	82
4.2.1	Induced polarization	82
4.2.2	Hydraulic tomography	86
4.2.3	Inversion	88
4.2.4	Synthetic model	90

4.3	Inversion results	92
4.3.1	Individual HT and IP inversion results	92
4.3.2	Joint inversion results	93
4.3.3	Influence of petrophysical bias	94
4.3.4	Comparison of structural similarity	95
4.4	Discussion	99
4.5	Conclusions	101
Synopsis		103
5.1	Summary and conclusions	104
5.2	Outlook	107
Bibliography		111
Appendix		139
A.1	Strategy of the exponential calibration	140
A.2	Full forward model and IP inversion result	142
A.3	Supporting Information on Römhild et al. (2024a)	144
Acknowledgements		XV
Curriculum vitae		XVII
Declaration		XXI

Glossary

a_f	fracture aperture
c	Cole-Cole frequency exponent
C	calibration coefficient
\mathbf{C}_α	calibration matrix
\mathbf{d}	data vector
d	density
D	diffusivity
D_+	diffusion coefficient of the Stern layer
f	frequency
f_α	conversion factor for hydraulic travel times
F	formation factor
$F()$	forward operator
g	gravitational acceleration
h	hydraulic head
i	imaginary unit
\mathbf{J}	Jacobian matrix
k	permeability
K	hydraulic conductivity
K_{eff}	effective hydraulic conductivity
L	likelihood function
m	cementation exponent (in Archie's law)
\mathbf{m}	model vector
m_0	intrinsic chargeability
M	number of parameter values in the model vector
n	number of Debye relaxations
\mathbf{n}	normal vector
N	number of observations in the data vector
$p()$	probability (in Bayesian formulation)
$q()$	proposal distribution (in Bayesian formulation)

Glossary

Q	source/sink term
S_{por}	inner surface area
S_s	specific storage
t	time
t_α	hydraulic travel time / early time
\mathbf{W}_d	data weight matrix
α	calibration exponent
Γ	domain boundary
ε	ray path
ζ	zeta potential
η	dynamic viscosity
θ	DFN model parameter set
ξ	calibration percentile
σ	data variance
σ^*	electrical conductivity (* denotes complex quantities)
σ'	real part of electrical conductivity
σ''	imaginary part of electrical conductivity
σ_0	DC conductivity
σ_{el}	electrolytic conductivity
σ_{int}	interface conductivity
σ_w	pore water conductivity
τ_σ	relaxation time (of Cole-Cole model in conductivity form)
ϕ	phase angle
Φ	porosity
Φ_d	data-model misfit
ψ	update probability
ω	angular frequency

List of Figures

1.1	Polarization mechanisms in porous media.	5
1.2	Continuum vs. fractured models.	11
2.1	Workflow for IP- K inversion and hydraulic calibration.	22
2.2	Bolstern aquifer analog: Location and data set.	23
2.3	Methodological comparison of IP and HT.	24
2.4	HT and IP inversion results for the Bolstern data set.	37
2.5	Histograms of K -estimation accuracy for the Bolstern data set.	40
2.6	Transport modeling results - snapshots of tracer plumes.	42
2.7	Transport modeling results - tracer breakthrough curves.	44
3.1	Location of the field site and acquisition geometry of HT experiments.	54
3.2	Travel time processing and inversion result.	61
3.3	DFN result: individual realization and fracture probability map.	62
3.4	Measured vs. modeled pressure response curves for HT experiments.	64
3.5	Influence of matrix parameters on the inversion results.	66
3.6	Snapshots of thermal tracer test simulations using COMSOL.	69
3.7	Comparison of measured data from the thermal tracer test with simulated data using the travel time and DFN inversion results.	69
3.8	Measured and predicted temperature response for fractures A and B.	71
4.1	General setup of IP experiments and illustration of data processing.	85
4.2	General setup of HT experiments and illustration of data processing.	88
4.3	Synthetic model and setup of HT and IP experiments.	91
4.4	Results of individual HT and IP inversion, as well as joint inversion.	94
4.5	Inversions results with petrophysical bias factors.	96
4.6	Comparison of structural similarity index for the inversion results.	97

Publications

The following three publications are part of this thesis (cumulative thesis).

Chapter 2 has been published as:

Römhild, L., Fiandaca, G., Hu, L., Meyer, L. and Bayer, P. (2022a): Imaging hydraulic conductivity in near-surface aquifers by complementing cross-borehole induced polarization with hydraulic experiments. *Advances in Water Resources*, 170, 104322. <https://doi.org/10.1016/j.advwatres.2022.104322>

Chapter 3 has been published as:

Römhild, L., Ringel, L.M., Liu, Q., Hu, L., Ptak, T. and Bayer, P. (2024a): Hybrid discrete fracture network inversion of hydraulic tomography data from a fractured-porous field site. *Water Resources Research*, 60, e2023WR036035. <https://doi.org/10.1029/2023WR036035>

Chapter 4 has been published as:

Römhild, L., Fiandaca, G. and Bayer, P. (2024b): Joint inversion of induced polarization and hydraulic tomography data for hydraulic conductivity imaging. *Geophysical Journal International*, 238(2), 960–973. <https://doi.org/10.1093/gji/ggae197>

Summary of author contributions:

Römhild et al. (2022a), Chapter 2:

Conceptualization: L.R., G.F., L.H. and P.B.; Methodology: L.R., G.F., L.H. and L.M.; Investigation: L.R., L.H. and L.M.; Data curation: L.R.; Writing - original draft: L.R.; Writing - review & editing: G.F., L.H., L.M. and P.B.; Visualization: L.R.; Software: G.F.; Supervision: G.F. and P.B.; Project administration: P.B.

Römhild et al. (2024a), Chapter 3:

Conceptualization: L.R., L.M.R., Q.L. and L.H.; Methodology: L.R. and L.M.R.; Investigation: L.R. and L.M.R.; Data curation: L.R., Q.L. and T.P.; Writing - original draft: L.R.; Writing - review & editing: L.M.R., Q.L., L.H., T.P. and P.B.; Visualization: L.R.; Software: L.R. and L.M.R.; Supervision: Q.L., L.H. and P.B.; Resources: T.P. and P.B.; Project administration: T.P. and P.B.

Römhild et al. (2024b), Chapter 4:

Conceptualization: L.R., G.F. and P.B.; Methodology: L.R. and G.F.; Investigation: L.R.; Data curation: L.R.; Writing - original draft: L.R.; Writing - review & editing: G.F. and P.B.; Visualization: L.R.; Software: L.R. and G.F.; Supervision: G.F. and P.B.; Project administration: G.F. and P.B.

I.

Aims and Objectives

1.1 Introduction

In times of a changing climate (IPCC, 2023), the reliability of groundwater resources becomes an increasingly immanent topic for many societies in various regions of the world (Earman & Dettinger, 2011; Green et al., 2011; Taylor et al., 2013; Amanambu et al., 2020; Barbieri et al., 2023). Monitoring and management of aquifers is crucial for ensuring the availability and quality of this vital freshwater resource (Gorelick & Zheng, 2015; Dillon et al., 2019; Rau et al., 2020; Condon et al., 2021). Therefore, groundwater flow and transport processes in the subsurface have to be understood correctly not only in its entirety, but also at a local scale for specific field cases (Refsgaard et al., 2012; Woodward et al., 2016; Guo et al., 2019). In particular, groundwater modeling tools play a key role in understanding and predicting some of these processes, such as contaminant transport (Comunian et al., 2011; Karatzas, 2017), groundwater discharge and recharge (Döll & Fiedler, 2008; Mogaji et al., 2015), interaction with rivers or seawater (Carrera et al., 2010; Brunner et al., 2017; Epting et al., 2018; Costall et al., 2020), and within geothermal applications (Griebler et al., 2016; Guo et al., 2022; Zhao et al., 2022).

To achieve reliable groundwater modeling results, accurate and high-resolution information about the distribution of hydraulic conductivity K and its heterogeneities at different scales within the domain of interest is indispensable (Huysmans et al., 2008; Zech et al., 2016). One-dimensional borehole data alone are often too sparse to cover all relevant structural features, and therefore not sufficient for providing a distribution of K that can be used for modeling tasks (De Marsily et al., 2005; Yu & Michael, 2022). Instead, tomographic methods can be used to map the K -heterogeneities with higher resolution (Cirpka et al., 2011; Ringel et al., 2024). These methods are either based on hydraulic stimulation (i.e., cross-borehole pumping tests), or estimate the hydraulic properties from geophysical data using petrophysical approximations (Binley et al., 2015). The subsequent section 1.2 introduces the geophysical method of induced polarization (IP), considering its ability to infer the relevant K -information based on the conceptual similarities between groundwater flow, and electrical conduction and polarization phenomena. Afterwards, the concept of hydraulic tomography (HT) is elaborated in section 1.3, which also includes a comparison between continuum- and fracture-based modeling approaches. Finally, section 1.4 delves into the topic of inverse problems, and illustrates the potential of jointly inverting IP and HT data for a common K -distribution.

1.2 Induced polarization methods for estimating hydraulic conductivity

More than a century has passed since the first observation of the IP effect by Schlumberger (1920). It was discovered while performing classical resistivity measurements when the abrupt termination of current injection did not trigger an instantaneous but slow decay of voltage as a result of charge storage effects in the subsurface, particularly in the presence of metallic sulfides (Seigel et al., 2007). To this day, IP field experiments are still often conducted with the same (or slightly modified) instrumentation and acquisition geometries as classical geoelectrical measurements, with two electrodes injecting a current into the subsurface, and two other electrodes recording the resulting voltage signal (Zarif et al., 2017). Typical acquisition geometries include surface profiles, 2D arrays, as well as cross-borehole setups.

In time-domain IP (TDIP) surveys, the voltage decay curves as a response to a step function of current injection are analyzed for retrieving the information about electrical conduction and polarization properties of the ground. TDIP experiments are often preferred for field surveys due to the wider availability of instruments and typically smaller acquisition times (Maurya et al., 2018b). However, measurements can also be performed in the frequency domain by injecting an alternating current and observing the phase shift of the resulting voltage signal. By covering a wide frequency range, the spectral properties of the IP effect can be captured directly. Due to a more straight-forward interpretation of the data and potentially higher accuracy, this method of spectral induced polarization (SIP) is mostly used for laboratory experiments (Kemna et al., 2012; Revil et al., 2014), but can also be applied in the field yielding results consistent with TDIP (Martin et al., 2020).

Although rooted in mineral exploration, the fields of application for the IP method have diversified in the last decades. Most prominently, the new sub-disciplines of biogeophysics (Atekwana & Slater, 2009; Kessouri et al., 2019) and hydrogeophysics (Binley et al., 2015; Day-Lewis & Bathija, 2022) have emerged, focusing on using the method for studying biological materials and their activity, as well as groundwater-related parameters and processes, respectively. This was facilitated by a more detailed understanding of the origins of the IP effect, leading to the development of a wide range of conceptual and mathematical models describing the electrical polarization phenomena.

1.2.1 Models for the IP effect

The IP effect is caused by a variety of electrochemical processes that allow a reversible storage of charges within the rock additional to pure conduction (Lesmes & Morgan, 2001; Bücker et al., 2019). In the high-frequency range ($> 10^3$ Hz), the so-called Maxwell-Wagner polarization is often dominant (Maxwell, 1873; Wagner, 1914), resulting from discontinuities in electrical conductivity between phase (solid, liquid, gas) interfaces. However, this phenomenon is not of particular interest for most practical applications of the IP method, and thus the focus is typically on lower frequencies (10^{-5} – 10^3 Hz). There, the presence of electron conducting particles can also produce a strong IP response, commonly referred to as electrode polarization (e.g., Pelton et al., 1978). However, since these materials are typically absent in sedimentary environments, this type of polarization is also not considered within this thesis.

Instead, diffusion-related decays of gradients in ion concentration are the main contributors to the IP effects that are of interest within hydrogeophysical applications. These processes are associated with the electrical double layer (EDL), i.e., the interface between the mostly negatively charged rock matrix and the pore space, which adsorbs charged ions from the pore fluid (Helmholtz, 1879; Revil & Glover, 1997) (Fig. 1.1a). As a result, an overall increase of electrical potential (Fig. 1.1b), ion concentration, and consequently electrical conductivity σ (Fig. 1.1c) towards the EDL can be observed.

When an external electric field is applied, three different EDL-related phenomena occur. First, the Stern layer polarization describes the tangential displacement of counterions in the Stern layer that is formed at the surface of a mineral (Schwarz, 1962) (Fig. 1.1d). This causes the ions of the diffuse layer to also be displaced, leading to an additional polarization component known as diffuse layer polarization (Dukhin et al., 1974). As a third contribution, the so-called membrane polarization is particularly pronounced at pore throat restrictions being blocked with cations (Marshall & Madden, 1959) (Fig. 1.1e).

Due to the finite velocity of ion displacements, part of the observed voltage response to the external electrical field is delayed, resulting in the gradual decays of voltage described in the previous section. Mathematically, this can be expressed in terms of a complex-valued and frequency-dependent electrical conductivity σ^*

$$\sigma^*(\omega) = \sigma_{\text{el}} + \sigma_{\text{int}}^*(\omega), \quad (1.1)$$

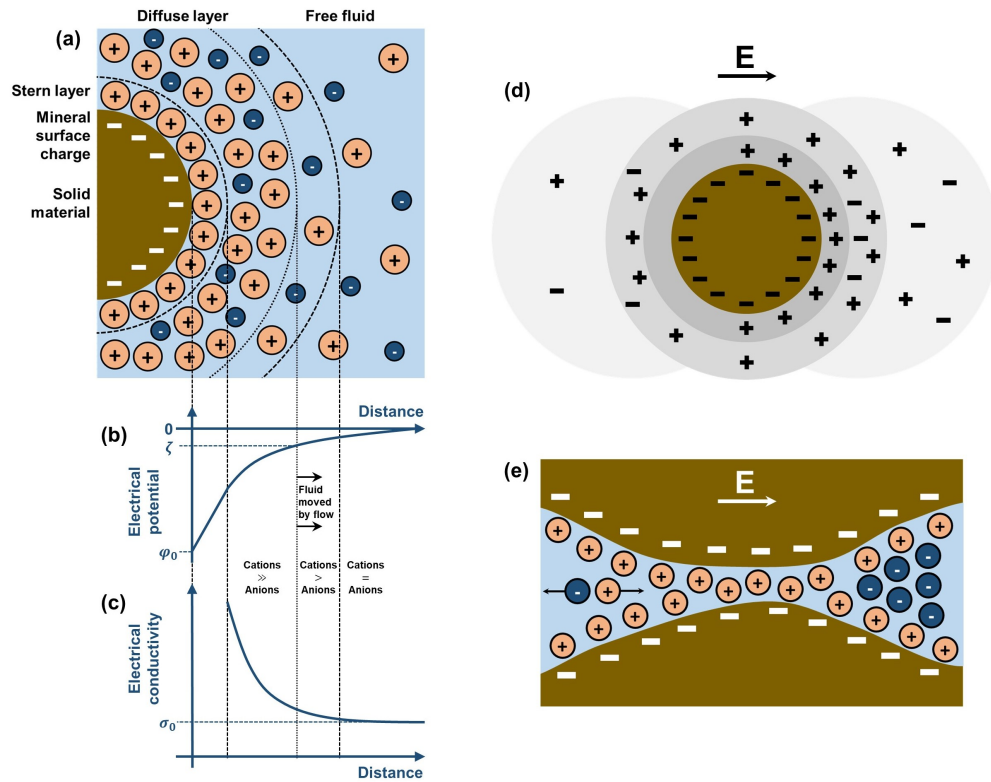


Figure 1.1: **(a)** The electrical double layer (EDL) forms at a negatively charged mineral surface. **(b)** Electrical potential (with zeta potential ζ). **(c)** Electrical conductivity (with DC conductivity σ_0) at the EDL. **(d)** Stern and diffuse layer polarization at a mineral grain. **(e)** Pore throat restriction with the blocking of ions in the diffuse layer (membrane polarization). Inspiration for the figures was taken from Binley & Slater (2020) and Bucker et al. (2019).

being a superposition of electrolytic conductivity σ_{el} in the free pore space, commonly described by Archie's law (Archie, 1942), and interface conductivity σ_{int}^* , with $\omega = 2\pi f$ being the angular frequency, and the * denoting complex quantities (e.g., Olhoeft, 1985). It can also be written in terms of real and imaginary part (σ' and σ'' , respectively), or as magnitude $|\sigma^*|$ and phase angle ϕ

$$\sigma^*(\omega) = \sigma'(\omega) + i\sigma''(\omega) = |\sigma^*| \cdot e^{i\phi}, \quad (1.2)$$

where i is the imaginary unit.

To describe the complex conductivity resulting from those polarization mechanisms, different analytical and mechanistic models have been developed (e.g., Vine-

gar & Waxman, 1984; Leroy & Revil, 2009; Revil, 2012; Bückner & Hördt, 2013; Bückner et al., 2019). They typically relate the IP response to other petrophysical parameters, like the formation factor F , or the inner surface area S_{por} . Such models are crucial for gaining a more detailed understanding of different polarization mechanisms and their relevance depending on different influencing parameters, especially in the context of highly accurate SIP laboratory experiments. However, they are usually too complicated for being used to evaluate field data. In such cases, simpler phenomenological models can be employed that often describe the spectral behavior of the complex conductivity quite accurately, though they are based less on the actual processes in the pore space.

For rock and soil types with a wide distribution of grain or pore sizes, the constant phase angle (CPA) model is considered a good approximation (Börner et al., 1996; Weller et al., 1996; Lajaunie et al., 2016). It assumes that the conductivity is characterized by the same phase angle ϕ over the complete frequency range. If, instead, the data exhibit a single, dominant polarization peak at a certain frequency, the Cole-Cole model is commonly used to describe the spectral behavior of σ^* (Cole & Cole, 1941; Pelton et al., 1978; Tarasov & Titov, 2013):

$$\sigma^*(\omega) = \sigma_0 \left[1 + \frac{m_0}{1 - m_0} \left(1 - \frac{1}{1 + (i\omega\tau_\sigma)^c} \right) \right]. \quad (1.3)$$

There, σ_0 is the DC conductivity, m_0 the intrinsic chargeability as defined by Seigel (1959), τ_σ the relaxation time, and c the frequency exponent. Although originally derived for electrode polarization using an equivalent electrical circuit model, it can also be a good approximation for sediments with a narrow distribution of grain or pore sizes (Revil et al., 2014). However, if multiple sources of polarization (i.e., more than one peak in the spectrum) are present, the more flexible Debye decomposition approach allows for obtaining objective parameters for the interpretation of such data (Nordsiek & Weller, 2008; Zisser et al., 2010; Weigand & Kemna, 2016). This is often regarded as the most generalized model space for IP data since any arbitrary complex conductivity spectrum can be represented by a superposition of n Debye relaxations:

$$\sigma^*(\omega) = \sigma_0 \left[1 - \sum_n m_n \left(1 - \frac{1}{1 + (i\omega\tau_n)} \right) \right]^{-1}, \quad (1.4)$$

with m_n as chargeability, and τ_n as relaxation time of contribution n . Further re-parameterizations of the Cole-Cole model have been proposed by Fiandaca et al. (2018a), such as the maximum phase angle (MPA) model, the maximum imaginary

conductivity (MIC) model, and the minimum imaginary resistivity (MIR) model.

All these parameter sets can potentially serve as model spaces for the inversion of IP data, yielding a spatial distribution of electrical parameters in the subsurface to explain observed data of IP field experiments (Hönig & Tezkan, 2007; Gazoty et al., 2012; Doetsch et al., 2015). If those were conducted in the time domain (TDIP), a Fourier transform has to be applied within the inversion procedure in order to retrieve frequency domain parameters (Fiandaca et al., 2012, 2013). The subsequent interpretation of such subsurface models in terms of hydraulic properties relies on petrophysical relations derived from laboratory experiments.

1.2.2 Petrophysical relations for K-estimation from IP data

Based on the conceptual similarities between the flow of groundwater and electric currents, approximate petrophysical relations have been found linking the IP parameters with hydraulic properties. In particular, the hydraulic conductivity K (or, interchangeably, permeability k) of porous rock is governed by the same pore space properties as the polarization mechanisms described in the previous section 1.2.1. Therefore, most petrophysical equations incorporate representations of two primary pore space characteristics: First, a pore volume parameter, such as porosity Φ or formation factor F can be derived from the electrolytic part of conductivity σ_{el} . Since a higher pore volume typically correlates with increased values in both K and σ_{el} , those two parameters are assumed proportional, resulting in an inverse relationship between K and F . Second, an increase in inner surface area S_{por} is mostly related to stronger polarization effects due to a greater density of EDLs. Therefore, an increase in the imaginary part of conductivity σ'' is observed, but K is usually lower due to higher tortuosity of the pore space, thus demonstrating an inverse relationship between K and σ'' . Such petrophysical laws can be found by systematic laboratory measurements, that also allow for quantification of additional empirical parameters. The approach found by Weller et al. (2015) for unconsolidated and fully saturated sediments belongs to this category, containing F as a measure for the volumetric properties, and σ'' accounting for the polarization strength:

$$k = \frac{1.08 \cdot 10^{-13}}{F^{1.12} (\sigma''(1 \text{ Hz}))^{2.27}}. \quad (1.5)$$

However, other studies suggest that instead of σ'' , the Cole-Cole relaxation time τ_{σ} can be a more appropriate parameter in some contexts. This parameter can serve

as a measure of characteristic hydraulic length scales, such as pore throat size or grain size, thus allowing for the quantification of hydraulic parameters. For instance, Revil et al. (2012b) proposed the relation

$$k = \frac{\tau_{\sigma} D_{+}}{4F}, \quad (1.6)$$

where D_{+} denotes the diffusion coefficient of the Stern layer. The discussion about the applicability of those two approaches for certain field settings is still ongoing (e.g., Weller et al., 2016), but it is important to note that they are based on similar principles and are therefore not necessarily contradictory.

Several studies have already used such petrophysical equations to estimate K from IP field data (e.g., Hördt et al., 2009; Attwa & Günther, 2013; Maurya et al., 2018a). However, these relations have always been applied after the inversion for IP parameters in a separate step. This sequential procedure usually makes an interpretation of the results in terms of hydraulic parameters more ambiguous, because starting models for the inversion, regularization parameters, prior information, and error estimation procedures can only be defined in terms of the electrical parameters, and not for K .

To overcome these issues, the first objective of this thesis consists in the development of an inversion procedure that allows for direct computation of K from TDIP data (Chapter 2). The petrophysical relations (Eq. 1.5 and 1.6) can be incorporated into the inversion directly by a re-parameterization of the Cole-Cole model space in terms of hydraulic properties. To retrieve the full spectral content, the inversion is based on the method of Fiandaca et al. (2012, 2013), and combines the petrophysical approaches of both Weller et al. (2015) and Revil et al. (2012b) to increase the robustness against varying field conditions. This new approach is expected to allow for better applicability of IP methods to aquifer characterization tasks, and to provide highly resolved K -information required for groundwater modeling.

Hypothesis 1:

Time-domain induced polarization data can be inverted directly for a hydraulic conductivity subsurface model.

1.3 Hydraulic tomography at porous and fractured sites

Inspired by tomographic setups commonly used for geophysical methods, similar acquisition schemes have been adapted for aquifer characterization approaches using hydraulic stimulation. Gottlieb & Dietrich (1995) first proposed the concept of hydraulic tomography (HT), which is based on sequential pumping tests at isolated depth intervals within a borehole, and the observation of the resulting pressure response at other nearby intervals. By performing these experiments for all source receiver combinations, the whole domain of interest can be covered, providing higher-resolution insights into the heterogeneities of hydraulic properties compared to traditional pumping tests. Other hydraulic methods utilized in this context comprise classical slug tests (Butler Jr., 2019), methods based on natural variations in hydraulic head like river stage tomography (Xia et al., 2023), or simplified and therefore more time-efficient versions of the HT concept (Brauchler et al., 2013b). In contrast to geophysical methods (such as IP), the hydraulic properties are derived directly from hydraulic experiments, and therefore no approximate petrophysical assumptions have to be applied. However, conducting pumping tests is often time-demanding and requires sophisticated equipment, limiting the number of feasible experiments considering the financial constraints. This typically sets restrictions to the achievable spatial resolution and also results in a high level of non-uniqueness of the inverse problem (Bohling & Butler Jr., 2010).

Nevertheless, HT has been used frequently in the field to image subsurface heterogeneities in sedimentary aquifers (Bohling et al., 2007; Berg & Illman, 2013; Cardiff et al., 2020; Zhao & Illman, 2022; Luo et al., 2023), for investigating faults and fractures in the context of nuclear waste deposits and geothermal sites (Illman et al., 2009; Zha et al., 2015; Klepikova et al., 2020; Ringel et al., 2022), or to identify preferential flow paths at mining sites (Mao et al., 2018; Wang et al., 2021b; Qiu et al., 2024). Various data processing and inversion techniques have been developed that can be used depending on the specific site characteristics. In particular, there typically is a clear distinction between porous and fractured media, which requires specialized modeling approaches.

1.3.1 Continuum-based modeling approaches

Continuous models are commonly preferred for describing the spatial distribution of physical properties in porous aquifers. In these models, structural features, such as sand and clay lenses or different sedimentary layers, usually exhibit smooth bound-

aries. Such continuous aquifer models require a discretization, on which the forward and inverse problem can be defined (Fig. 1.2a). Each discretization element stores an average value of the parameter inside, and the variability of this parameter with respect to neighboring elements can often be defined by smoothness constraints.

The simplest type of discretization in 2D is a rectangular grid, describing the heterogeneous features in the form of a pixel map. For solving the forward and inverse problem on such grids, finite difference methods are typically employed. In contrast, triangular meshes require the utilization of finite element modeling for performing these tasks. As an alternative to equidistant cell boundaries, adapted grids can be used that allow for a local refinement of cells in areas of higher heterogeneity (Vesnaver & Böhm, 2000; Mehl et al., 2006). Furthermore, staggered grids represent superpositions of individual rectangular grids with a relatively coarse resolution that are shifted among each other (Vesnaver & Böhm, 2000; Brauchler et al., 2003; Hu et al., 2015; Divahar et al., 2024). They require running the forward calculation multiple times for each iteration but yield a higher resolution of the result without leading to ill-posed inverse problems. In addition, continuous models may also be stored in the form of pilot points, and the actual parameter distribution is interpolated between those points based on the geostatistical properties of the aquifer (Jimenez et al., 2013; Illman, 2014; Poduri & Kambhammettu, 2021).

Various inversion techniques for HT data have been developed based on continuous models. Geostatistical approaches comprise the simultaneous successive linear estimator (Berg & Illman, 2011; Yeh & Liu, 2000), quasi-linear estimator (Kitanidis, 1995; Cardiff et al., 2020), or ensemble Kalman filter (Sánchez-León et al., 2020). They are based on geostatistical prior models that assume a certain spatial correlation of hydraulic properties. In contrast, a travel time inversion of HT data requires fewer prior assumptions, and also less computational effort since it does not simulate a complete groundwater flow model (Brauchler et al., 2003). Instead, the approach is based on the eikonal equation, which can be derived from the groundwater flow equation (Vasco et al., 2000) and solved by ray-tracing techniques, such as Dijkstra's algorithm (Dijkstra, 1959).

Due to the wider availability of established tools for discretizing a model based on the continuum assumption (e.g., Geuzaine & Remacle, 2009), fractured rock is also modeled with this approach quite frequently (Hao et al., 2008; Zha et al., 2015). Although main flow channels can be captured, the identification of individual fractures requires a different type of model.

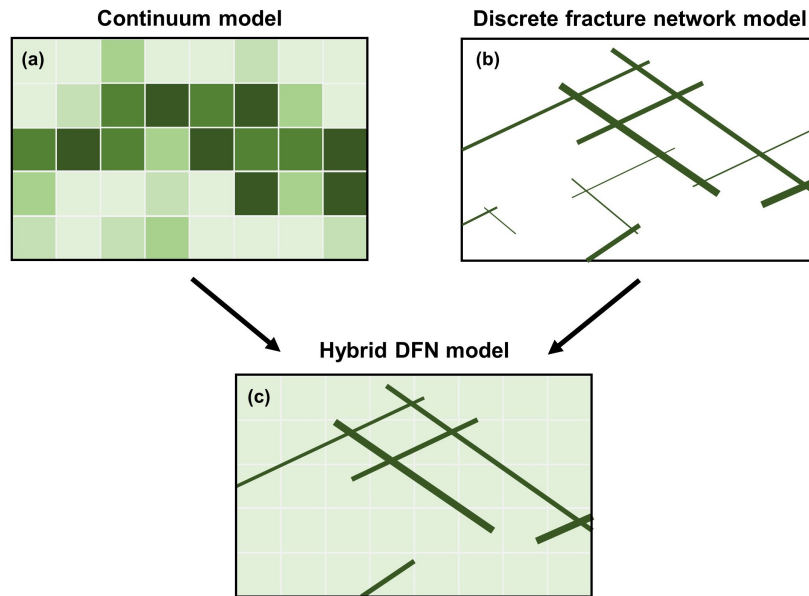


Figure 1.2: Illustration of the hybrid discrete fracture network (DFN) model approach (c), combining both continuum (a) and DFN models (b).

1.3.2 Fracture-based modeling approaches

In most crystalline and metamorphic rock, groundwater flow is predominantly maintained by individual fractures, while the rock matrix is typically assumed to be impermeable. Fracture networks can therefore represent the preferential pathways for flow and transport within these types of rock (Adler & Thovert, 1999; Berkowitz, 2002). Correctly characterizing such networks is essential for different applications such as constructing and operating geothermal sites (Gan & Elswort, 2016; Make-donska et al., 2020; Liu et al., 2021), evaluating the suitability of potential nuclear waste disposal facilities (Tsang et al., 2015; Hadgu et al., 2017; Li et al., 2022b), assessing the excavation damaged zone around tunnels (De La Vaissiere et al., 2014; Lei et al., 2017b; Vazaios et al., 2019), or predicting flow and transport processes in fractured freshwater reservoirs (Neumann, 2005; Parker et al., 2012; Li et al., 2020).

To account for their special characteristics, discrete fracture network (DFN) models have been developed that approximate the fractures as discrete line elements (in a 2D domain), or as planar 2D objects (in a 3D domain), and often neglect the matrix completely (Adler et al., 2013; Lei et al., 2017a; Berre et al., 2019) (Fig. 1.2b). Each fracture can be described by a parameter set that contains an average aperture

a_f , hydraulic conductivity K_f , specific storage $S_{s,f}$, as well as positional parameters. The forward simulation requires solving the partial differential equation for pressure diffusion in a fracture mid-plane

$$a_f S_{s,f} \frac{\partial h}{\partial t} - \nabla_T (a_f K_f \nabla_T h) = a_f Q, \quad (1.7)$$

within a finite element framework (e.g., Ringel et al., 2021). There, h is the hydraulic head, and Q is a source/sink term. The gradient ∇_T is evaluated in the fracture plane.

For the inversion of HT data following Ringel et al. (2021), each iteration may comprise the insertion or deletion of a fracture, or a parameter update for a fracture, with the aim of minimizing the overall data misfit. This is usually implemented based on stochastic procedures, which consequently results in a stochastic representation of the fracture network (e.g., a fracture probability map). DFN inversion approaches have recently been applied to different types of HT field data acquired in crystalline rock (Klepikova et al., 2020; Fischer et al., 2020; Ringel et al., 2021, 2022).

However, some rock types may also exhibit characteristics of both model types, i.e., individual fractures and a permeable matrix. In particular, this dualism is often observed for different types of sandstone and claystone (Liu & Manga, 2009; Zhang et al., 2020; Wang et al., 2022). Discretization and modeling approaches for these so-called fractured porous media have been reviewed by Berre et al. (2019). They require the simultaneous implementation of both continuum models for considering matrix flow, and DFN models for incorporating individual fractures (Fig. 1.2c). These hybrid models may capture the hydraulic processes in such media more accurately, thereby yielding better inversion results in terms of minimization of misfit to the experimental HT data, and consequently a more reliable representation of the actual aquifer properties. The development of such a hybrid DFN inversion procedure, including its application to field data, is the second objective of this thesis (Chapter 3). It is expected that the subsurface models achieved by the hybrid approach are favorable compared to both continuum- and DFN inversion when predicting flow and transport processes at fractured porous sites.

Hypothesis 2:

A combination of continuum- and fracture-based modeling approaches yields more accurate and reliable inversion results using hydraulic tomography data.

1.4 Inverse problems

1.4.1 Mathematical background

Most geophysical and hydrogeological imaging methods, such as IP and HT, require solving an inverse problem to achieve a subsurface model of the parameters of interest based on the experimental data (Zhdanov, 2015; Binley & Slater, 2020). In any inversion framework, a forward problem needs to be defined that describes the physical processes for the respective method, i.e., how a given distribution of the model parameters in the subsurface generates the observed data. Generally, this forward problem can be defined as

$$\mathbf{d} = F(\mathbf{m}), \quad (1.8)$$

where \mathbf{d} is the data vector containing N observations, \mathbf{m} is the model vector containing M parameter values, and F is the forward operator describing the physical system, often by differential equations. In practice, this formulation needs to be reversed to find the model parameters based on a given set of input data. Consequently, the inverse problem can be defined by

$$\mathbf{m} = F^{-1}(\mathbf{d}). \quad (1.9)$$

In most cases, this problem is non-linear, and the forward operator F is non-invertible, so the inverse solution needs to be obtained iteratively. Additional challenges in solving the inverse problem may arise due to inherent measurement errors or noise contaminating the data, by the discretization of the differential equations, by simplifications in the underlying physics (including petrophysical assumptions, scaling issues, dimensionality restrictions, anisotropy, etc.), and consequently non-uniqueness of the inverse problem.

A wide range of inversion strategies has been developed based on different types of input data, forward models, and specific requirements for the characteristics of the result. As a first category, deterministic approaches aim at minimizing the misfit between the observed data and the hypothetical data derived from a forward simulation (Eq. 1.8) for a given model. The optimization is implemented in an iterative process that updates the model vector, so that the result of the forward simulation moves towards the experimental data. An example of such a strategy is the utilization of the Gauss-Newton solution (e.g., Oldenburg & Li, 1994; Loke &

Dahlin, 2002; Binley & Slater, 2020), where the equation

$$(\mathbf{J}^T \mathbf{W}_d^T \mathbf{W}_d \mathbf{J}) \Delta \mathbf{m} = \mathbf{J}^T \mathbf{W}_d^T (\mathbf{d} - F(\mathbf{m}_k)) \quad (1.10)$$

needs to be solved for the parameter update $\Delta \mathbf{m}$. There, \mathbf{W}_d is the data weight matrix, a diagonal matrix containing the reciprocal of the standard deviation of each measurement, and \mathbf{m}_k is the current model vector at iteration k . Furthermore, \mathbf{J} is the Jacobian (or sensitivity) matrix given by

$$J_{i,j} = \frac{\partial F(\mathbf{m}_k)_i}{\partial m_j} \quad (1.11)$$

with $i = 1, 2, \dots, N$ and $j = 1, 2, \dots, M$. The new parameter set \mathbf{m}_{k+1} can then be obtained by

$$\mathbf{m}_{k+1} = \mathbf{m}_k + \Delta \mathbf{m} \quad (1.12)$$

Different types of damping and regularization terms are often employed in practice for handling the non-uniqueness of the problem, and to improve the geological realism of the subsurface model (Mojabi & LoVetri, 2009; Lelièvre & Farquharson, 2013; Wu, 2017; Benning & Burger, 2018). Within the inversion, the data-model misfit Φ_d given by

$$\Phi_d = (\mathbf{d} - F(\mathbf{m}))^T \mathbf{W}_d^T \mathbf{W}_d (\mathbf{d} - F(\mathbf{m})) \quad (1.13)$$

is minimized. A satisfactory solution is typically obtained when the chi-squared statistic

$$\chi^2 = \frac{\Phi_d}{N} \quad (1.14)$$

is close to one. In this thesis, both the IP- K inversion developed in Chapter 2, as well as the travel time inversion for HT data used in all subsequent chapters, are based on the Gauss-Newton approach.

In addition to deterministic methods, stochastic approaches can also be used for solving the inverse problem. Within this category, Bayesian inversion procedures are typically employed (e.g., Jackson & Matsuura, 1985; Ulrych et al., 2001). This statistical inference starts with a prior probability of model parameters $p(\mathbf{m})$ and derive the posterior probability based on the data \mathbf{d} following Bayes' theorem (Bayes, 1763)

$$p(\mathbf{m}|\mathbf{d}) = \frac{p(\mathbf{m})p(\mathbf{d}|\mathbf{m})}{p(\mathbf{d})}, \quad (1.15)$$

where the notation $p(\mathbf{X}|\mathbf{Y})$ describes the probability of an event \mathbf{X} given the event \mathbf{Y} . More specifically, $p(\mathbf{d}|\mathbf{m})$ is often referred to as the likelihood function that quantifies the likelihood of a data set given a set of model parameters. The inverse problem is then solved by determining the parameter set that corresponds to the maximum likelihood. However, the stochastic nature of the approach allows for the computation of a distribution of posterior models together with its associated likelihoods. This is often achieved by implementing a Markov chain Monte Carlo (MCMC) search in the parameter space (Green, 1995; Chib, 2001), generating multiple plausible models and evaluating their individual likelihood.

These stochastic approaches allow for a better evaluation of the uncertainty within inversion results (Bagnardi & Hooper, 2018; Ringel et al., 2022; Zhang et al., 2024), e.g., due to measurement errors or non-uniqueness of the solution, as well as an easier integration of prior models from various types of data sources (Ramirez et al., 2005; Linde et al., 2015). However, such methods are computationally more expensive than deterministic inversions, and therefore applications to large data sets or model domains with high dimensionality are rarely feasible. Within this thesis, the (hybrid) DFN inversion approach (Chapter 3) is based on Bayesian methods.

1.4.2 Joint inversion

For many hydrogeophysical applications, the complexity of the subsurface cannot be captured by a single data type. Instead, geophysical as well as hydraulic methods have individual advantages and limitations in terms of sensitivity distribution, reliability of parameter estimates, spatial resolution, or practical feasibility. To combine the abilities of multiple methods, joint inversion approaches have been developed that minimize the data misfit of both data types and invert for a common distribution of the model parameters (Linde & Doetsch, 2016). Joint inversion procedures are well-established tools for a variety of geophysical applications, where different types of experiments are conducted at the same site to achieve more informative results (e.g., Gao et al., 2012; Mollaret et al., 2020; Turco et al., 2021).

The idea of jointly inverting electrical and hydraulic data in the context of aquifer characterization has already been expressed in both the hydrogeological community (e.g., Bohling & Butler Jr., 2010), and among hydrogeophysicists (e.g., Slater, 2007). In particular, when imaging heterogeneities in hydraulic conductivity K , results obtained from IP may have a high spatial resolution due to potentially small electrode spacing, but bear a significant amount of uncertainty in K -quantification introduced by the petrophysical assumptions (section 1.2). In contrast, K -estimates

from HT are highly reliable, but data sets are often sparse due to the time and financial demands of the pumping experiments (section 1.3). Therefore, a joint inversion of both IP and HT data for a common K -distribution is expected to benefit from a combination of the complementary strengths of these methods. Since the petrophysical relations between IP parameters and K are only valid in fully saturated, unconsolidated sediments, the joint inversion approach will be restricted to these environments (section 1.2.2). Consequently, fractures are not relevant in such settings, and therefore continuum models (section 1.3.1) can be applied for discretizing the model space for both methods. Due to its computational efficiency, the travel time inversion approach for HT data seems most appealing for a joint inversion. Furthermore, it does not require any prior assumptions, and the joint inversion can be performed in a deterministic framework (section 1.4.1) for both methods. The development of such an inversion scheme is the third objective of this thesis (Chapter 4).

Hypothesis 3:

A joint inversion of induced polarization and hydraulic tomography data improves the spatial resolution, accuracy and reliability of the hydraulic conductivity estimation by combining the complementary abilities of both methods.

II.

Imaging hydraulic conductivity in near-surface aquifers by complementing cross-borehole induced polarization with hydraulic experiments

Lukas Römhild¹,
Gianluca Fiandaca²,
Linwei Hu^{3,4},
Laura Meyer¹,
Peter Bayer¹

¹ Institute of Geosciences and Geography, Martin Luther University Halle-Wittenberg

² Department of Earth Sciences "Ardito Desio", Università degli Studi di Milano

³ Institute of Geosciences, Christian Albrechts University Kiel

⁴ GeoAnalysis-Engineering GmbH, Schauenburgerstraße 116, 24143, Kiel

Advances in Water Resources 170 (2022) 104322

<https://doi.org/10.1016/j.advwatres.2022.104322>

Abstract

Precise information about the spatial distribution of hydraulic conductivity (K) in an aquifer is essential for the reliable modeling of groundwater flow and transport processes. In this study, we present results of a new inversion procedure for induced polarization (IP) data that incorporates petrophysical relations between electrical and hydraulic parameters, and therefore allows for the direct computation of K . This novel approach was successfully implemented for the Bolstern aquifer analog by performing synthetic IP experiments with a combined surface and cross-borehole setup. From these data, the distribution of K was retrieved with high accuracy and resolution, showing a similar quality compared to images achieved by hydraulic tomography. To further improve the quantitative estimates of K , we use synthetic pumping test data to inform two novel calibration strategies for the IP inversion results. Both calibrations are especially helpful for correcting a possible bias of the IP inversion, e.g., due to resolution limitations and/or to bias in the underlying petrophysical relations. The simulation of tracer experiments on the retrieved tomograms highlights the accuracy of the inversion results, as well as the significant role of the proposed calibrations.

2.1 Introduction

Tomographic methods have evolved as a promising family of hydrogeological field investigation techniques for imaging the hydraulic conductivity (K) distribution (Yeh & Liu, 2000; Vasco et al., 2000; Jimenez et al., 2013; Zhao & Illman, 2018; Pouladi et al., 2021). They rely on sending and recording multiple signals at different positions of an aquifer. By processing all signals together, the spatial distribution of hydraulic parameters is reconstructed. The choice of a tomographic configuration for identification of subsurface structures is rooted in geophysical exploration (Gottlieb & Dietrich, 1995; Yeh & Lee, 2007). Accordingly, tomographic concepts based on classical hydrogeological field techniques with hydraulic stimulation or tracer signals often adopt data inversion principles that are established in geophysics (Hu et al., 2011; Kong et al., 2018; Ringel et al., 2021). Vice versa, especially near surface geophysical techniques such as ground penetrating radar, electrical resistivity tomography or electromagnetic induction are tuned to not only identify geological but also hydraulic structures (Slater, 2007; Linde et al., 2006; McLachlan et al., 2021).

Still, hydraulic or tracer tomography is not fully established in practice. A major reason is the rather high experimental demand for installation of field equipment and borehole devices (Bohling & Butler Jr., 2010; Brauchler et al., 2013b; Cardiff et al., 2013; Klepikova et al., 2020). Fast applicability in the field is an advantage of many geophysical techniques. However, a common shortcoming is that aquifer heterogeneities are described by geophysical proxy parameters. As classical geophysical exploration techniques do not test hydraulic properties directly, their capacity to provide meaningful hydrogeological insight in aquifers is limited. Ideally, geophysical and hydrogeological information is thus jointly processed for obtaining hydrogeophysical tomograms to benefit from the advantages of both approaches (Irving & Singha, 2010; Vilhelmsen et al., 2014; Ahmed et al., 2016).

In the growing research field of hydrogeophysics (Binley et al., 2015) a strong focus is on electrical methods due to their ability of sensing pore space properties that govern the hydraulic parameters (Revil et al., 2012a; Wang et al., 2021a). However, imaging hydraulic conductivity requires the separation of pore volume and pore surface properties, which cannot be achieved by conventional geoelectrical methods. As a remedy, the additional information contained in induced polarization (IP) measurements about electrical polarization effects at the pore-matrix-interface can be used to quantitatively separate these properties (Slater, 2007).

To link the electrical parameters of IP measurements with the hydrogeological parameters, we mainly rely on empirical relations derived from laboratory measurements. The first quantitative relation between IP parameters and K was established by Börner et al. (1996). Since then, a variety of other empirical laws has been derived by spectral induced polarization (SIP) laboratory measurements (Slater & Lesmes, 2002; Binley et al., 2005; Revil & Florsch, 2010; Titov et al., 2010; Revil, 2012; Attwa & Günther, 2013; Weller et al., 2015; Robinson et al., 2018).

Most of the IP parameters that are valuable for estimating K are defined in the frequency domain, as e.g., the Cole-Cole parameters (Cole & Cole, 1941; Pelton et al., 1978), and can therefore be most easily derived from SIP measurements. However, although some applications of SIP in the field do exist (Kemna et al., 2012; Orozco et al., 2012; Gallistl et al., 2018), this method is mainly used for the electrical characterization of rocks in the laboratory (Revil et al., 2014; Börner et al., 2017; Römhild et al., 2019), whereas for field campaigns time domain IP (TDIP) measurements are most common (Kemna et al., 2004; Gazoty et al., 2012; Doetsch et al., 2015). This gap can be overcome by using a Fourier transform within the IP inversion procedure, so that TDIP data can be inverted for frequency domain parameters, such as Cole-Cole parameters (Fiandaca et al., 2012, 2013) or other re-parameterizations of the Cole-Cole model (Fiandaca et al., 2018a). This approach yields results of a similar quality compared to frequency domain measurements (Madsen et al., 2017), but often has an advantage in terms of acquisition time (Maurya et al., 2018b; Martin et al., 2020).

In several studies, K has already been estimated from these electrical parameters at field scale (Hördt et al., 2009; Attwa & Günther, 2013; Maurya et al., 2018a). However, the petrophysical relations mentioned above have always been applied after the inversion for IP parameters, making the interpretation in terms of hydraulic parameters ambiguous. Instead, incorporating the petrophysical laws into the inversion procedure allows the direct computation of the K -distribution in the subsurface from the measured IP data. Although ambiguities might also be reduced with strong structural priors such as training images (Pirrot et al., 2017), a petrophysical inversion approach can have further advantages. By introducing a new parameterization, parameter correlations can be reduced, and the direct inversion for K makes it easier to study its uncertainties and how data errors propagate to model errors. It also allows to apply the regularization to the actual hydraulic parameters instead of the electrical parameters and simplifies the integration of prior models that are often given as a distribution of K . Petrophysical inversion strate-

gies have already been applied in other contexts, such as permafrost sites (Mollaret et al., 2020), gas hydrate systems (Turco et al., 2021) or reservoir characterization (Gao et al., 2012), but mostly with the aim of establishing a joint inversion.

While our new IP- K inversion approach has already been mentioned briefly in conference abstracts (Fiandaca et al., 2021; Martin et al., 2021), we now present the complete methodology and a detailed assessment of the results for the first time. We are aiming to show the abilities and limitations of this deterministic inversion for imaging K -heterogeneities in near-surface aquifers by performing synthetic modeling and inversion tests on aquifer analog data with a combined surface and cross-borehole IP setup. We compare those results with data derived from synthetic hydraulic tomography (HT) experiments using a similar setup. Our main goal is to achieve a distribution of K that would yield a correct solute transport simulation. For this purpose, a straightforward calibration strategy of complementing IP inversion with hydraulic information is introduced.

In the following, we briefly explain the methodological concepts of IP and HT, as well as our new IP- K inversion approach. As the study site for simulating a synthetic cross-hole HT and IP application, a sedimentary aquifer analog is implemented to compare the abilities of the two methods in imaging decimeter-meter scale K -heterogeneities with varying point spacing. The performance of the new calibration strategy is evaluated and all findings are discussed with special emphasis on the applicability of the suggested methodology within field campaigns.

2.2 Materials and Methods

Fig. 2.1 gives an overview of the procedures applied in this study. The Bolstern aquifer analog (Heinz et al., 2003) serves as the input data set for the forward modeling of IP data and the HT synthetic experiments. The achieved data sets are then used for the respective inversion (the new IP- K inversion procedure and an HT travel time inversion). Additionally, we achieve an effective hydraulic conductivity K_{eff} as an average value for the whole domain by a small set of seven pumping tests and use it to calibrate our inversion results. To assess the quality of those calibrations and the performance of the two methods in general, we finally conduct tracer transport simulations with the achieved K tomograms and evaluate them based on imaged tracer plumes as well as depth-integrated tracer breakthrough curves.

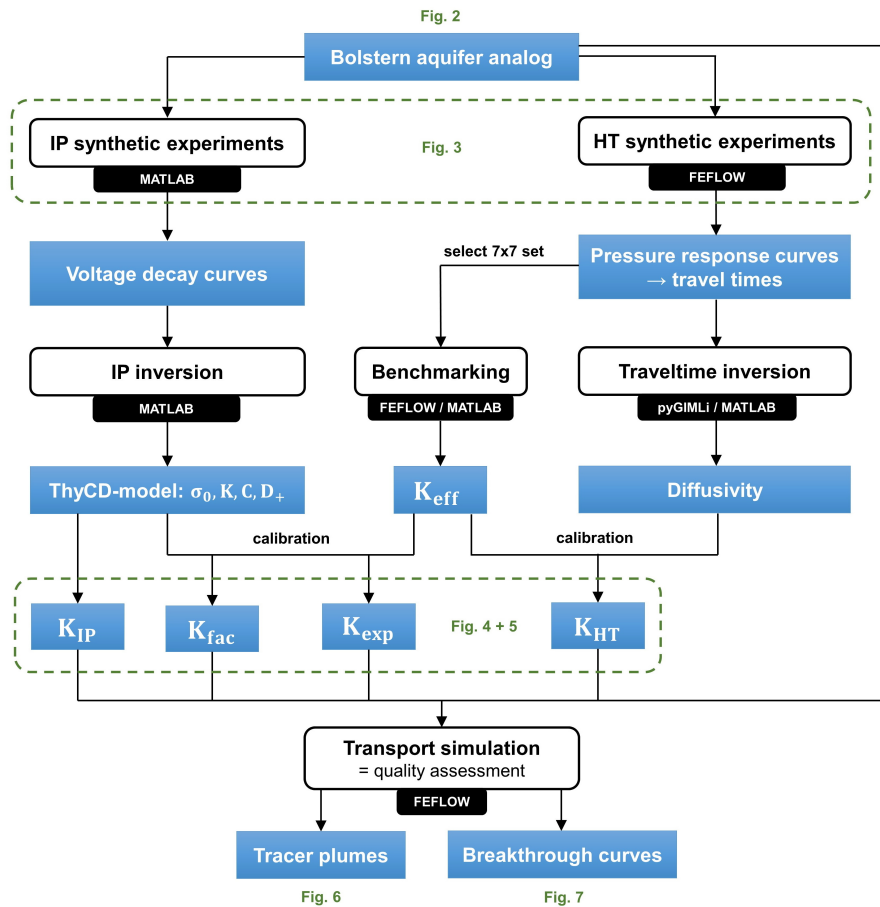


Figure 2.1: Workflow for imaging K in heterogeneous aquifers with induced polarization (IP, left section) and hydraulic tomography (HT, right section). Blue boxes represent any type of data and black boxes contain the different processing steps. The green labels refer to the other figures in this work.

2.2.1 Bolstern aquifer analog

The Bolstern aquifer analog data set (Heinz et al., 2003) was derived from an outcrop analog study of fluvial deposits located near Bolstern (SW-Germany, see Fig. 2.2a) within the paleo-discharge zone of the Rhine glacier. The analog study comprises a rectangular $20 \text{ m} \times 7 \text{ m}$ 2D cross-section (Fig. 2.2b), which is built up by a mosaic of hydrofacies units that were delineated from the outcrop wall at a resolution of 0.05 m . The hydrofacies units represent nearly hydraulically homogeneous units with K derived from grain size analysis, as well as porosity information. The hydrofacies accord with the sedimentary lithofacies, and this is

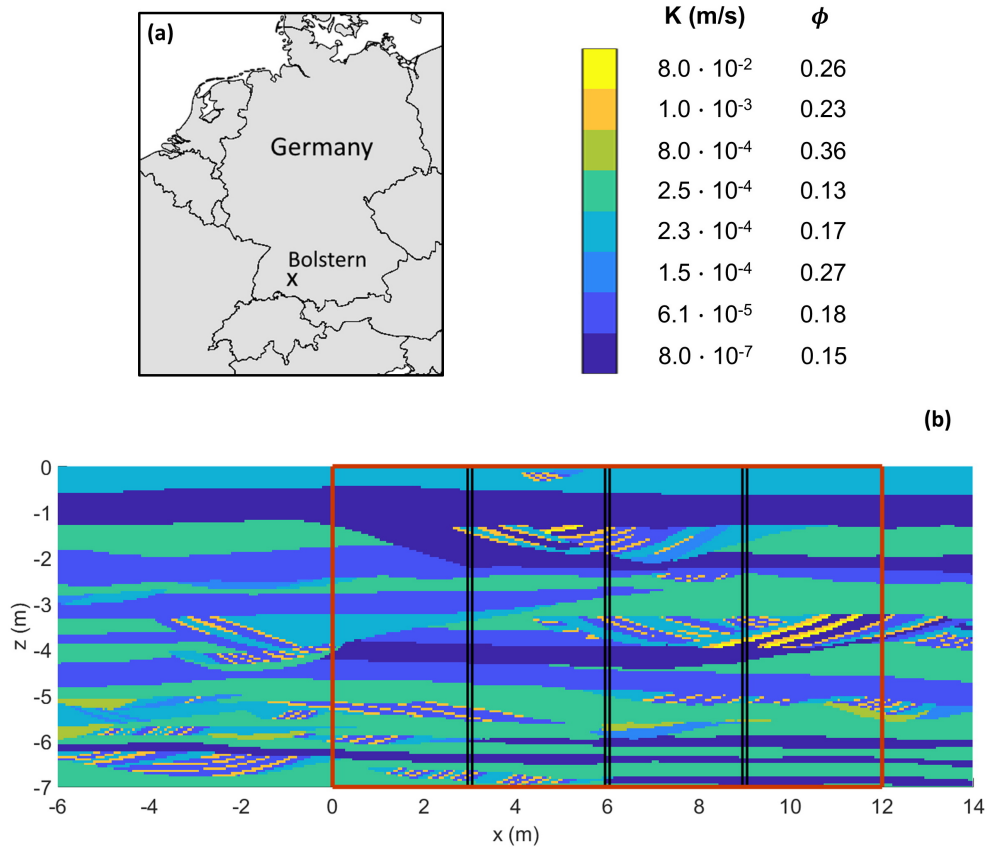


Figure 2.2: **(a)** Location of the Bolstern aquifer analog in SW-Germany and **(b)** visualization of the data set as a 2D cross-section including the heterogeneities of hydraulic conductivity K and porosity ϕ . The red rectangle indicates the section of the data set used in this work and the black lines represent the three hypothetical boreholes at $x = 3$ m, 6 m and 9 m.

reflected in the structural features of the analog, with heterogeneous layers and cross beddings as a common characteristic for many sedimentary unconsolidated aquifers. The Bolstern analog has already been used as a realistic test case for modeling contaminant transport in previous work (Höyng et al., 2015).

We use a section of the whole analog between $x = 0$ m and 12 m (which corresponds to $x = 6$ m and 18 m in the original nomenclatures of Heinz et al. (2003)), covering the whole depth range from $z = 0$ m to -7 m (red rectangle in Fig. 2.2b). For all simulated virtual experiments we assume to have three boreholes at $x = 3$ m, 6 m and 9 m (black lines in Fig. 2.2b).

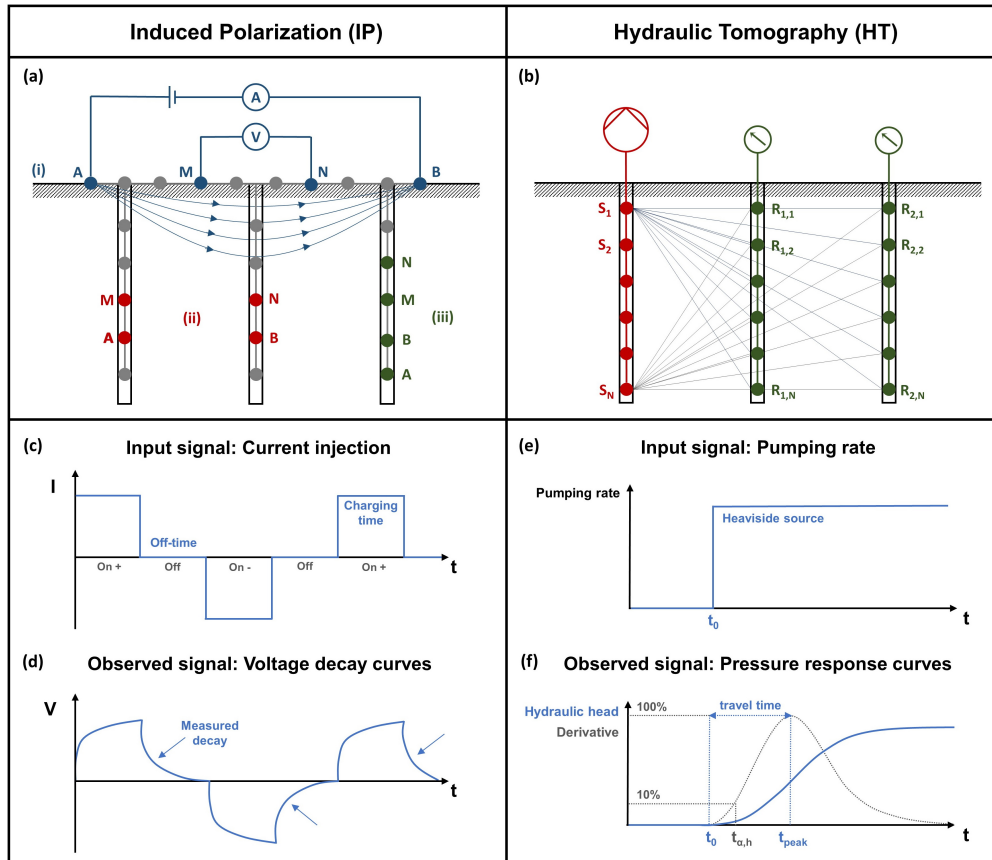


Figure 2.3: Comparison of induced polarization (left section) and hydraulic tomography (right section) experimental setups as well as simplified input and output signals. **(a)** Typical IP setup with current electrodes A, B and voltage electrodes M, N distributed (i) on a surface profile, (ii) as a cross-borehole setup or (iii) in a single borehole. **(b)** Typical HT setup with source points $S_1 \dots S_N$ (pumping locations) in the left borehole and receiver points $R_{1,1} \dots R_{2,N}$ (observation locations) in the two other boreholes. **(c)** Input signal of the injected current: rectangular function with alternating polarity. **(d)** Observed voltage signal: decay curves reacting to the injected current and the polarization effects in the rock's pore space. **(e)** Pumping signal in the source points following a Heaviside function. **(f)** Observed pressure response curves at the receiver points with peak time t_{peak} and early time $t_{\alpha,h}$ according to the 10%-diagnostics approach.

2.2.2 Induced Polarization

Electrical rock properties

The electrical conductivity σ^* of a rock is generally considered to be a frequency-dependent and complex-valued quantity (Olhoeft, 1985)

$$\sigma^*(\omega) = \sigma_{el} + \sigma_{int}^*(\omega) \quad (2.1)$$

consisting of electrolytic conductivity σ_{el} and interface conductivity σ_{int}^* , with ω being the angular frequency and the * denoting complex quantities. It can be written in terms of real and imaginary part (σ' and σ'' , respectively) or as magnitude $|\sigma^*|$ and phase angle ϕ

$$\sigma^*(\omega) = \sigma'(\omega) + i\sigma''(\omega) = |\sigma^*| \cdot e^{i\phi}, \quad (2.2)$$

where i is the imaginary unit. The electrolytic part is controlled by the conduction through a rock's pore space and thus depends on pore volume properties as described by Archie's Law (Archie, 1942)

$$\sigma_{el} = \frac{\sigma_w}{F} = \Phi^m \cdot \sigma_w, \quad (2.3)$$

where σ_w is the pore water conductivity, $F = \Phi^{-m}$ is the formation factor, Φ is porosity and m is the empirical cementation exponent. This formulation assumes fully saturated conditions.

The interface conductivity σ_{int}^* , however, may contain contributions from a variety of electrical polarization phenomena that are mainly related to the interface between rock matrix and pore space. If electronically conductive minerals, such as graphite or pyrite, are absent, as it is mostly the case in sedimentary environments, diffusion-related polarization connected to the electrical double layer (EDL) at the pore-matrix-interface is dominant (Marshall & Madden, 1959; Schwarz, 1962).

While standard geoelectrical methods are only sensitive to the real part σ' of the electrical conductivity, IP measurements can retrieve information about the imaginary part σ'' as well. This is either done by conducting spectral induced polarization (SIP) measurements in the frequency domain and then converting the magnitude and phase angle information to a complex electrical conductivity, or by performing time domain induced polarization (TDIP) measurements and full-decay spectral inversion (Fiandaca et al., 2012, 2013; Madsen et al., 2020). We will focus on the latter option since the acquisition time is smaller in the field (Maurya et al.,

2018b) and a good retrieval of spectral properties is achievable when a wide time range is used in acquisition (Madsen et al., 2017), for instance through the analysis of full-waveform recordings (Olsson et al., 2016).

A typical TDIP field setup is similar to a standard DC geoelectrics setup with a sequence of quadrupoles injecting a current with two electrodes (A, B) and measuring the resulting voltage with two other electrodes (M, N). A simplified setup is shown in Fig. 2.3a. The sequence is typically distributed along a 2D profile on the surface, e.g., following a gradient protocol (i), and can be complemented by cross-borehole measurements (ii) or quadrupoles in a single borehole (iii). For the synthetic experiments carried out within this study, a combination of the three options shown in Fig. 2.3a is used, but a variety of other sequences is possible (Bing & Greenhalgh, 2000). While surface IP measurements are becoming a more widely used method, field examples of cross-borehole IP are still rare (Kemna et al., 2004; Binley et al., 2016; Bording et al., 2019).

To extract meaningful parameters from IP data, the Cole-Cole model is commonly used to describe the spectral behavior of σ^* (Cole & Cole, 1941; Pelton et al., 1978; Tarasov & Titov, 2013):

$$\sigma^*(\omega) = \sigma_0 \left[1 + \frac{m_0}{1 - m_0} \left(1 - \frac{1}{1 + (i\omega\tau_\sigma)^c} \right) \right]. \quad (2.4)$$

Here, σ_0 is the DC conductivity, m_0 the intrinsic chargeability as defined by Seigel (1959), τ_σ the relaxation time and c the frequency exponent.

Based on petrophysical relations found in laboratory studies, the electrical properties of a rock can be used to predict hydraulic conductivity K . In the following, we make use of two different approaches. First, Revil (2012) found a relation for permeability k (and hence hydraulic conductivity K) based on relaxation time τ_σ , formation factor F and the diffusion coefficient of the Stern layer D_+ :

$$k = \frac{\tau_\sigma D_+}{4F}. \quad (2.5)$$

A powerlaw fit of $R^2 = 0.88$ was reported for the used set of clean saturated sand samples. The relation is based on the idea that τ_σ can be treated as a measure for typical scale lengths (e.g., pore throat size), that in return govern the hydraulic conductivity. The volumetric properties are accounted for by F as a measure for effective porosity. At first sight, this approach does not include any empirical parameters and should be straight-forward to use. However, while τ_σ and F can be

directly derived from the IP measurements, the diffusion coefficient D_+ can only be estimated, typically depending on the clay content. Revil et al. (2015) give the following values for clean sand and clay:

$$\begin{aligned} D_{+,sand} &= 1.3 \cdot 10^{-9} \cdot \text{m}^2 \text{s}^{-1}, \\ D_{+,clay} &= 3.8 \cdot 10^{-12} \cdot \text{m}^2 \text{s}^{-1}, \end{aligned} \quad (2.6)$$

However, other laboratory findings are raising doubt about the existence of two distinct values for D_+ (Weller et al., 2016). Instead, an apparent diffusion coefficient D_a can be introduced that may cover a much wider range of values, although its physical significance remains unclear. In our study, in which sand-clay mixtures are actually reflected in a wide range of K -values, we still use the two values given by Revil et al. (2015) to compute a distribution of D_+ directly from K by imposing an interpolation in logarithmic space. However, the purpose of this simplification is only the simulation of realistic τ_σ -values (according to Eq. 2.5) within the forward modeling.

The second petrophysical approach was introduced by Weller et al. (2015). It uses the formation factor F and the imaginary part σ'' evaluated at a frequency of 1 Hz for permeability estimation:

$$k = \frac{\alpha}{F^\beta (\sigma''(1 \text{ Hz}))^\gamma} \quad (2.7)$$

with the empirical parameters $\alpha = 1.08 \cdot 10^{-13}$, $\beta = 1.12$ and $\gamma = 2.27$ for unconsolidated and fully saturated sediments. The coefficient of determination is reported as $R^2 = 0.862$ and an additional degree of uncertainty lays in the applicability of the empirical parameters α , β and γ in the given geological setting.

Furthermore, we use a relationship between imaginary and real part of surface conductivity found by Weller et al. (2013):

$$\sigma''(1 \text{ Hz}) = l \cdot \sigma'_{\text{int}}(1 \text{ Hz}) \quad (2.8)$$

with $l = 0.042 \pm 0.022$, but imposing the relation at the frequency $f = (2\pi\tau_\sigma)^{-1}$ (Fiandaca et al., 2018b).

Finally, the conversion from permeability k to hydraulic conductivity K can be achieved by

$$K = \frac{d \cdot g}{\eta} \cdot k, \quad (2.9)$$

where d is the density of the pore fluid, g the gravitational acceleration and η the dynamic viscosity of the pore fluid. Assuming a groundwater temperature of 10°C we use the approximation

$$K = 7.5 \cdot 10^6 \cdot k. \quad (2.10)$$

For more details on the petrophysical background we refer to Fiandaca et al. (2018b) and the references therein.

Clearly, all petrophysical laws between hydraulic and electrical parameters are only approximations that bear a significant amount of uncertainty. Additionally, due to the regularization applied within the inversion, the petrophysical relationships of the tomograms are also resolution-dependent (Hermans & Irving, 2017). Although we will show how these regularization-induced errors as well as a simple bias in the petrophysical relations can partly be corrected by our proposed calibrations, their intrinsic scatter can barely be reduced by these procedures. Especially in strongly heterogeneous aquifers (like the Bolstern aquifer) this uncertainty can be significant, easily spanning one to two orders of magnitude (e.g., Hördt et al. (2009)). In addition, further parameters (like the cementation exponent m) that are approximated as constants, might be spatially variable (Schön, 2015; Yue, 2019). Therefore, petrophysical relations actually present in the field are often far from the laws derived in the lab (e.g., Benoit et al. (2019)), so that not only the inherent uncertainty, but also the applicability of those relations in a given field setting are limiting factors for the quality of the inversion result. Synthetic experiments should always be regarded as best case scenarios showing the upper limit of K -prediction quality that may be achieved in a field application. However, even best-case scenarios are anything but trivial, and insights from synthetic studies are important means to judge the role of procedural assumptions for an inversion and the resolution capability of the proposed methods.

Forward modeling

For defining the input data set used within the forward simulation, the WhyCDF model space

$$\mathbf{m}_{\text{WhyCDF}} = \{\sigma_w, K, D_+, F, c\} \quad (2.11)$$

was used. The WhyCDF acronym indicates the model parameters, i.e. water and hydraulic conductivity σ_w and K , respectively, diffusion coefficient D_+ and formation factor F (the frequency exponent c is not specified in the acronym). The idea of re-parameterizing the model space is based on Fiandaca et al. (2018a), now

being extended by directly imposing the petrophysical relations (Eq. 2.1, 2.2, 2.4, 2.5, 2.7, 2.8 and 2.10) onto the objective function. Therefore, the conversion from hydrological to electrical parameters is part of the modeling process and not a separate procedure. The two petrophysical approaches by Revil (2012) and Weller et al. (2015) are simultaneously used by forcing them to yield the same permeability k . The five different input parameters were set up in the following way:

- Water conductivity σ_w was assumed to be constant at 100 mS/m, which is a realistic value for groundwater (Schön, 2015).
- Hydraulic conductivity K was directly imported from the Bolstern data set (Heinz et al., 2003).
- The diffusion coefficient D_+ was derived from K by interpolation in log-space from the sand-clay values suggested by Revil et al. (2015), thereby imposing realistic τ_σ -values on the data.
- The formation factor F was computed from the porosity information contained in the Bolstern data set by assuming a constant cementation exponent of $m = 1.3$ as a realistic value for unconsolidated sediments (Schön, 2015).
- The frequency exponent of the Cole-Cole model c was assumed to be constant at 0.5.

The full data set (hydraulic conductivity K , diffusion coefficient D_+ and bulk conductivity σ_0 including both F , σ_w and σ'_{int}) is shown in section A.2.

The synthetic IP experiments are based on a setup consisting of one surface profile over the entire length of the data set ($x = 0 \dots 12$ m) as well as electrodes in three hypothetical boreholes at $x = 3$ m, 6 m and 9 m. We consider this to be a realistic setup within a field study that should allow resolving the heterogeneities of the aquifer within the whole domain. Furthermore, the same setup of boreholes is expected to work well for HT, so that the results of the two methods can be compared directly. In practice, the same boreholes could be used to conduct all the experiments.

To simulate realistic field conditions, Gaussian noise of 2% and 10% magnitude was added after the forward simulation to resistivity and IP data, respectively. Field data can mostly be fitted with this level of error, as for instance demonstrated in Maurya et al. (2018a). Some exemplary decay curves with added noise and error bars of the assumed standard deviation model are depicted in section A.2.

We run the forward simulation in 2D following Fiandaca et al. (2013) with three different electrode spacings - 1 m, 0.5 m and 0.25 m - to assess the impact of varying spacings on the inversion (in terms of computational performance and ability to image K -heterogeneities). The sequence follows a commonly used gradient protocol for the surface profile and borehole quadrupoles according to the cases (i), (ii) and (iii) shown in Fig. 2.3a, with IP time gates ranging from 0.003 s to 12 s. The total number of quadrupoles (from which the total duration of a field experiment might be estimated) are 162 for 1 m spacing, 885 for 0.5 m spacing and 2866 for 0.25 m spacing.

Inversion

The inversion was performed in the ThyCD model space

$$\mathbf{m}_{\text{ThyCD}} = \{\sigma_0, K, D_+, c\} \quad (2.12)$$

consisting of total (DC) conductivity σ_0 , hydraulic conductivity K , diffusion coefficient D_+ and frequency exponent c . All four parameters are space-dependent and uncoupled during the inversion, but the spatial variability of each parameter can be adjusted by setting horizontal and vertical constraints.

While a model space with five parameters (like WhyCDF) is convenient as input for a forward simulation, it is not possible to invert for both the formation factor and the water conductivity, since the effects of both parameters on DC conductivity cannot be separated. Consequently, the water conductivity is considered a prior information in the inversion, and the total DC conductivity is used for the parameterization of the inversion result. This choice is supported by the results of Markov chain Monte Carlo modeling performed with different parameterizations (Fiandaca et al., 2021), where the ThyCD model space turned out to be the most suitable and is therefore used for this work. Again, it should be stressed that the conversion from electrical to hydrological parameters is an inherent part of the inversion and not a separate procedure.

Although we refer to the diffusion coefficient as D_+ here, it might also be interpreted as an apparent diffusion coefficient D_a (Weller et al., 2016) in the inversion results. We also performed additional inversion tests with a different model space, where D_+ is replaced by τ_σ , so that Eq. 2.5 (Revil, 2012) is actually not used. The distribution of K remains almost identical, which shows that Eq. 2.7 (Weller et al., 2015) alone can also be sufficient for the inversion of TDIP data.

The data space of the inversion consists of the DC data and the full decays of the quadrupole sequence. The objective function, which contains the squared data misfit and smoothness regularization terms for vertical and horizontal constraints, is minimized through an iterative Gauss-Newton approach (Fiandaca et al., 2013).

We ran all the codes on a standard desktop PC with an 8-core i7-9700K 3.6 GHz processor and 32 GB RAM. The runtime for one iteration is about one minute for the 1 m spacing electrode sequence, 7-8 minutes for the 0.5 m sequence and around 30 minutes for the 0.25 m sequence, which adds up to a total inversion runtime of several hours (depending on the number of iterations) in the last case. This shows that also the inversion of field data can mostly be conducted on standard PC equipment.

Calibration with hydraulic data

Identification and resolution of K -heterogeneity is in particular relevant for performing transport modeling. Therefore, it is especially crucial to obtain accurate K -estimates in the preferential flow paths and thus in areas of high K . However, the strongest IP signal (e.g., in terms of chargeability) is typically measured in materials with low K since they have a higher inner surface area and therefore a more pronounced polarization connected to the EDL. In contrast, in the high- K -zones the IP signal is relatively weak, so that the K -estimates in the preferential flow paths are less supported by the IP data and might be less accurate. Considering these unfavorable properties of IP, resulting tomograms may resolve structural features very well but they are not very reliable with respect to the hydraulic characterization of preferential flow paths. Additionally, the uncertainties of the petrophysical relations linking electrical and hydraulic properties, as well as regularization effects might produce a bias in K -prediction. As a remedy, we suggest calibrating the IP inversion result by incorporating information gathered from pumping test data.

In the synthetic example, we retrieve the effective hydraulic conductivity K_{eff} as a single value for the whole domain by performing synthetic pumping tests on the Bolstern data set using Feflow. The procedure is inspired by the approach of Wu et al. (2005). A setup of seven pumping locations in the left borehole and seven observation points in the right borehole is used (see section A.1, part c). The pumping tests are carried out in exactly the same way as the HT experiments (see section 2.2.3). Additionally, we set up a model with homogeneous K and perform the same experiments. The optimal K -value of the homogeneous model is chosen by minimizing the cumulative RMS-misfit when comparing these hypothetical

pressure response curves with those of the Bolstern data set (“benchmarking”). We consider the value for K producing the smallest misfit to be the effective hydraulic conductivity K_{eff} and found the following value for the Bolstern aquifer analog:

$$K_{\text{eff}} = 7 \cdot 10^{-5} \frac{\text{m}}{\text{s}}. \quad (2.13)$$

In practice, K_{eff} may be inferred from the transmissivity that is estimated by conducting a single standard pumping test at the site.

We suggest two different approaches to use K_{eff} for calibrating the IP inversion results: (i) calibration with a constant factor (factor calibration) and (ii) calibration with a flexible calibration matrix using an exponential relationship (exponential calibration).

The first option consists of a simple multiplication of the inversion result \mathbf{K}_{IP} with the calibration coefficient C , so that the geometric mean of the calibration result \mathbf{K}_{fac} will be equal to K_{eff} :

$$\mathbf{K}_{\text{fac}} = \mathbf{K}_{\text{IP}} \cdot C, \quad (2.14)$$

$$C = \frac{K_{\text{eff}}}{\text{mean}(\mathbf{K}_{\text{IP}})}. \quad (2.15)$$

This calibration is based on the assumption that K_{eff} should be close to the geometric mean of the K -values of the original data set \mathbf{K}_{orig} (considering only the inner part between the boreholes), which for the Bolstern aquifer analog is found to be

$$\text{mean}(\mathbf{K}_{\text{orig}}) = 3.75 \cdot 10^{-5} \frac{\text{m}}{\text{s}}. \quad (2.16)$$

K_{eff} is slightly higher than this value, because it is typically more sensitive to the preferential flow paths (and therefore to areas with high K), especially in a highly anisotropic medium with pronounced horizontal layering as present in the Bolstern aquifer. However, we would still propose using the geometric mean of the K -field since this does not require any a priori assumptions about structural features or anisotropy in a field setting.

The exponential calibration attempts taking into account the different sensitivities of IP experiments and pumping tests by introducing a flexible calibration matrix \mathbf{C}_α . The concept of this approach is visualized in section A.1, already including the results for different parameterizations. The calibration matrix is made up by

$$\mathbf{C}_\alpha = e^{\alpha \cdot \mathbf{K}_{\text{IP}}} \quad (2.17)$$

and the calibration result \mathbf{K}_{exp} is achieved by computing the Hadamard product between \mathbf{C}_α and the inversion result \mathbf{K}_{IP} :

$$\mathbf{K}_{\text{exp}} = \mathbf{C}_\alpha \circ \mathbf{K}_{\text{IP}}. \quad (2.18)$$

For low K -values (strong IP effect), the elements in \mathbf{C}_α will be close to one, so that the inversion result is not changed by the calibration, whereas for higher K -values (weak IP effect) the impact of the calibration generally becomes stronger. However, the overall strength and direction of the calibration is determined by the exponent α , which is chosen according to the pumping test data. We iterate over a wide range of values for α in order to minimize the misfit between the geometric mean of the calibration result \mathbf{K}_{exp} and K_{eff} .

$$\left| \text{mean} \left(\mathbf{K}_{\text{exp}} \right]_{\xi}^{100\%} \right) - K_{\text{eff}} \left| \xrightarrow{\alpha \in \mathbb{R}} \min! \quad (2.19)$$

Since K_{eff} is often higher than the actual geometric mean of K (as shown above for the Bolstern aquifer), we do not use the whole data set to compute the geometric mean within this calibration, but neglect a certain percentile ξ with the lowest K -values. The impact of ξ is visualized in section A.1: for very low values (close to 0%) the result is likely to be over-corrected, whereas for too high values an under-correction will occur. However, we find that the optimal percentile ξ can be estimated by visual assessment of the uncalibrated inversion result, and the function $\alpha(\xi)$ as shown in part (b) of section A.1 allows for an evaluation of the impact of different ξ -values on the calibration result. Typically, the optimal value for ξ will rise with increasing electrode spacing since smoothing effects lead to more extensive areas of low K . We finally choose $\xi = 30\%$ for 0.25 m spacing, $\xi = 35\%$ for 0.5 m spacing and $\xi = 50\%$ for 1 m spacing. Undoubtedly, this choice is to some extent subjective, and more experience and testing will be needed to choose the best value for ξ in other applications.

2.2.3 Hydraulic Tomography

General concept

Hydraulic tomography (HT) requires hydraulic stimulation (e.g., pumping or slug tests) with several observation points at different locations to generate a tomographical configuration, similar to many geophysical tomography methods (Fig. 2.3b). The pressure response measured at the observation point is used to invert the

stratigraphic structure, i.e. the spatial distribution of hydraulic diffusivity, hydraulic conductivity and specific storage. The main inversion algorithms consist of geostatistics-based and travel time-based methods. The geostatistical methods for HT inversions can be predicated on a variety of algorithms, including simultaneous successive linear estimator (Berg & Illman, 2011; Yeh & Liu, 2000), quasi-linear estimator (Cardiff et al., 2020; Kitanidis, 1995) or ensemble Kalman filter (Sánchez-León et al., 2020). A common feature of these approaches is that they require a priori geostatistical models to assume the spatial correlation of the hydraulic parameters. In contrast, travel time methods used for HT inversion (Brauchler et al., 2003, 2013a) are based on an eikonal equation, which is transferred from the groundwater flow equation (Vasco et al., 2000) and can be solved by ray-tracing or particle tracking techniques. Compared to the first class of methods, this approach requires much less computational effort since it does not simulate in a complete groundwater flow model. Additionally, it does not require any prior assumptions about the geostatistical model, which can be highly uncertain due to the sparse measurements and various application scales. However, the travel time-based approach has limitations in reproducing the hydraulic parameters in low-permeability areas due to the low ray coverage. Although many studies prove that the structure of the formation can be readily reconstructed, a sequential inversion scheme is still required for a more accurate quantification of the hydraulic parameters (Hu et al., 2011, 2015; Jimenez et al., 2013).

Forward modeling

The synthetic HT experiments were simulated using the software Feflow (Diersch, 2014). The model domain was discretized by irregular triangular meshing. The initial hydraulic head in the whole domain is set to zero and we apply constant-head boundaries at the two sides. The hydraulic conductivity values were assigned to the mesh according to the values of the Bolstern aquifer analog, whereas the specific storage coefficient was assumed to be homogeneous at $S_s = 10^{-4} \text{ m}^{-1}$ according to typical values found in literature (Kuang et al., 2020). Source points were placed at the hypothetical borehole at $x = 3 \text{ m}$, whereas receiver points were placed at $x = 6 \text{ m}$ and $x = 9 \text{ m}$. Three different scenarios were simulated with varying vertical spacing of respectively 0.25 m, 0.5 m and 1 m within the boreholes. Therefore, the setups are similar to the IP experiments and the quality of the results can be directly compared. At the receiver points, the hydraulic head was recorded during the pumping tests, which are sequentially carried out from top to bottom.

The pumping signal is a Heaviside function with a constant rate of 1 l/s, as shown in Fig. 2.3e.

The resulting pressure response curves were imported to Matlab for further processing. All source-receiver-combinations with a ray path angle larger than 60° were filtered out since the layered stratigraphy typical for a shallow porous medium can be better resolved by reducing those large-angle ray paths (Brauchler et al., 2007). The 10% diagnostic (Brauchler et al., 2003) is selected for the inversion, meaning that the early time $t_{\alpha,h}$ is picked where the derivative value reached 10% of the maximum derivative at the observation point (Fig. 2.3f). Hence, the data space consists of all source and receiver coordinates (except the filtered ones) as well as the respective early times. The travel time information was contaminated with a noise level of 3%, similar to Doetsch et al. (2010) and Hu et al. (2017).

Inversion

Hydraulic travel time of a pumping test is defined as a line integral in which the pumping-induced pressure is generated at the source point x_1 and travels along the path ε before reaching the receiver point x_2 :

$$\sqrt{t_{\alpha,h}} = \frac{1}{\sqrt{6f_{\alpha,h}}} \int_{x_1}^{x_2} \frac{d\varepsilon}{\sqrt{D(\varepsilon)}}, \quad (2.20)$$

where $t_{\alpha,h}$ is the early time and $f_{\alpha,h}$ is a conversion factor (Brauchler et al., 2003). The subscript h indicates the usage of a Heaviside source. Similar to the seismic travel time inversion, Eq. 2.20 is resolved using ray tracing techniques, and the inverted slowness can be converted to the hydraulic diffusivity D . In this study, the open-source framework pyGIMLi is utilized to invert the hydraulic travel times, which is based on the generalized Gauss-Newton method (Rücker et al., 2017; Günther et al., 2006) and where the forward operator for calculating the travel times uses Dijkstra's algorithm (Dijkstra, 1959). As a final step, we use the factor calibration approach introduced for IP to translate the achieved diffusivities \mathbf{D} to a hydraulic conductivity distribution \mathbf{K}_{HT} that is in agreement with K_{eff} . This procedure replaces the common approach of multiplying with a specific storage coefficient S_s ($K = D \cdot S_s$), which is typically also assumed as homogeneous.

2.2.4 Tracer Experiments

We want to assess the quality of the inversion results by performing synthetic tracer experiments using the achieved K -images and compare the results to those obtained by modeling with the original Bolstern data set.

The corresponding simulations were conducted using Feflow in the area between the hypothetical boreholes ($x = 3 \text{ m} \dots 9 \text{ m}$). Steady-state hydraulic conditions were assumed, and constant heads assigned to the model boundaries induce a hydraulic gradient of 0.001 between the inflow and outflow borders. A conservative tracer was injected as a hypothetical line source with a constant rate of 1 mg/l at the upstream border of the model domain ($x = 3 \text{ m}$, left borehole). The longitudinal and vertical transverse dispersivities were set to $2.5 \cdot 10^{-2} \text{ m}$ and $2.5 \cdot 10^{-4} \text{ m}$, respectively, according to the values given in Höyng et al. (2015).

2.3 Results

2.3.1 HT and IP Inversion Results

Fig. 2.4c gives an overview of all the inversion results for the different methods and spacings. The original Bolstern data set is given at the top (Fig. 2.4a), where the grey numbers (1) - (5) indicate the most important highly permeable layers. Those layers are only subjectively defined to make it easier to refer to certain features in the text, but we will also show that they are responsible for the major tracer fingers found in the transport simulation presented below. Also note that the K -images derived from HT comprise only the domain between the boreholes (between $x = 3 \text{ m}$ and $x = 9 \text{ m}$), whereas IP has the ability to image areas left and right of that domain as well, although with decreasing sensitivity. We show all the inversion results as images of K to allow a direct comparison.

The HT travel time inversion produced meaningful results that reveal the most important structures and overall good estimates of K . With 0.25 m and 0.5 m spacing, all the highly permeable layers (1) - (5) can be reconstructed at the correct locations and with well-estimated K -values. However, smaller heterogeneities, as e.g., within layer (2), cannot be resolved and some inversion artifacts are visible in the results, as e.g., a decrease in K in the direct vicinity of the left borehole. The inversion result for 1 m spacing misses the uppermost layer (1) since no source and receiver locations are present in this part of the aquifer. However, the other layers (2) - (5) are still visible, although smoothing effects are becoming more pronounced.

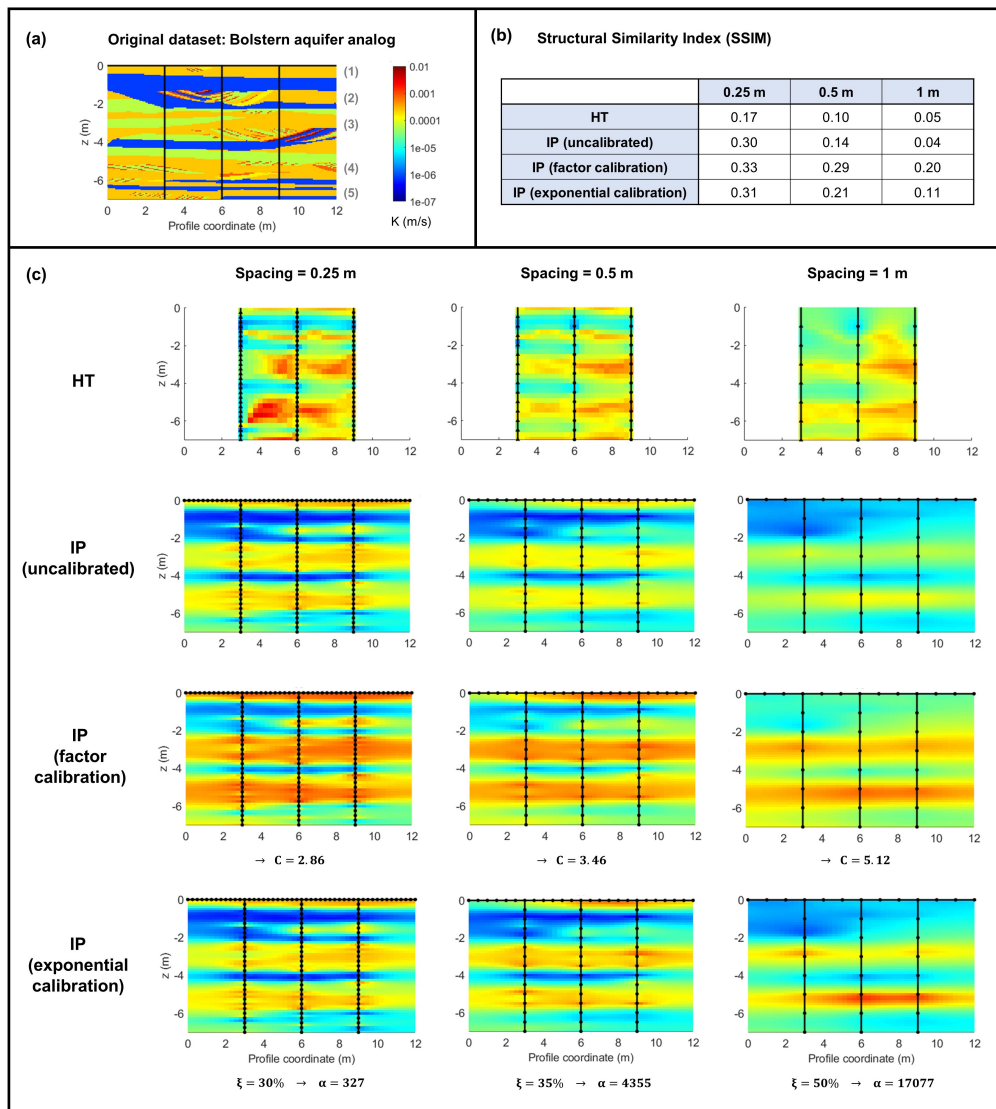


Figure 2.4: (a) The original data set of the Bolstern aquifer analog. The colorbar for K also applies to all inversion results. (b) Structural similarity index (SSIM) of the inversion results compared to the original data set. (c) Overview of all inversion results for HT, IP and the two different IP calibrations for varying spacing of pumping locations / electrodes, given as images of K .

The travel time inversion typically yields integrated values along the different ray paths, which in our case produces an offset between K -values left and right of the central borehole. Although the general trend of the major layers is correct and the inversion results reflect the true behavior of the original data set, local

K -heterogeneities are not always attributed to the exact location, but are smeared along the respective section of the ray path, creating a sharp border at the central borehole.

For IP we show the uncalibrated results for K as well as the images achieved by the new factor calibration and exponential calibration procedures. Note that the ThyCD inversion of IP data always yields a set of parameters, of which only K is shown in Fig. 2.4. An example of the complete set of parameters is given in A.2.

Firstly, we focus on the uncalibrated IP results. With 0.25 m electrode spacing, the aquifer heterogeneities are correctly reconstructed in terms of structural behavior and K -quantification. The highly permeable layers (1) - (4) are clearly retrieved by the inversion, but layer (5) can hardly be reproduced. Obviously, the sensitivity in this lowest part is small due to a very limited number of quadrupoles. However, when it comes to resolving smaller heterogeneities within the layers, IP yields slightly better results than HT and the attribution of certain K -heterogeneities to their exact location is more reliable.

When increasing the electrode spacing, smoothing effects introduced by the regularization become more pronounced and this effect is much stronger compared to the HT results. During IP measurements, one quadrupole integrates over an area of at least three times the spacing also in vertical direction, whereas for HT the integrative behavior is mainly related to the horizontal direction (along the ray path). Therefore, HT can resolve the borders between horizontal layers quite well, while this becomes much more difficult for IP. Another effect of the regularization is that the K -values, especially in the highly permeable layers, are typically under-estimated for larger electrode spacing. Therefore, we cannot expect to achieve correct transport simulations using those results. This can be overcome by using the new calibration procedures employed in the following.

The factor calibration leads to an overall increase in K for all three spacings since the value for K_{eff} is higher than the geometric mean of the inversion results. This yields an improvement in K -estimation especially for the larger spacings (0.5 m and 1 m), where the K -values of the most permeable layers are now predicted more correctly. However, an over-estimation of K can be observed in the less permeable zones. This drawback can be overcome by the exponential calibration, which leaves the lowest K -values unchanged and only adjusts the permeable zones to the pumping test data, as described in section 2.2.2. This effect is clearly visible in the results: now the K -estimates are very close to the original data set in all parts of the aquifer and for all three spacings. The exponential calibration typically

sharpens the contrast of the resulting image, thereby diminishing the smoothing effects especially for larger electrode spacings.

To quantify the reproduction quality of aquifer structures, we calculate the structural similarity index (SSIM) for each inversion result compared to the original data set (Fig. 2.4b). This metric is commonly used in image processing and measures the similarity between two images by taking into account luminance, contrast and structural information (Wang et al., 2004). It is bounded between 0 and 1, while the latter value indicates perfect similarity. We use the Python package “scikit-image” (van der Walt et al., 2014) to calculate the SSIM and find it to be a useful measure to assess the quality of the inversion results.

For all methods, a decreasing SSIM with increasing spacing can be observed due to lower data density and stronger smoothing effects. This behavior is expected and corresponds to the visual assessment of the inversion results. Generally, the lowest SSIM is computed for the HT results (between 0.17 and 0.05). Although the major layers are retrieved correctly, the method is not capable of retrieving the true structural behavior on smaller scales. The IP results yield relatively high SSIM values for the smallest spacing (0.30), indicating a good reproduction of the structural features. However, increasing the electrode spacing leads to a stronger decline of the SSIM compared to HT, showing again that smoothing effects are more pronounced for IP in this example. The factor calibration can strongly improve the structural reproduction, with the SSIM slightly increasing for 0.25 m spacing and strongly increasing for 0.5 m and 1 m spacing. While measurements with small spacing and therefore high data density cannot be improved much further by the calibration, the results achieved with larger spacing strongly benefit from this procedure. The exponential calibration is less successful in improving the structural information of the results, but still yields higher SSIM values compared to the uncalibrated IP tomograms.

To further evaluate the prediction quality of the K -estimates, we show histograms of the ratio between the estimated and the true value for each cell of the inversion result (Fig. 2.5). To perform the comparison, the values of the 0.05 m \times 0.05 m cells of the original data set had to be averaged within the corresponding bigger cells of the inversion results. In the histograms, values at 10^0 indicate a perfect prediction of K compared to the averaged value of the original data set. We also show the median value of the ratio (blue line) as well as how much of the prediction is within one order of magnitude (black lines and corresponding percentage) and within two orders of magnitude (red lines and corresponding percentage).

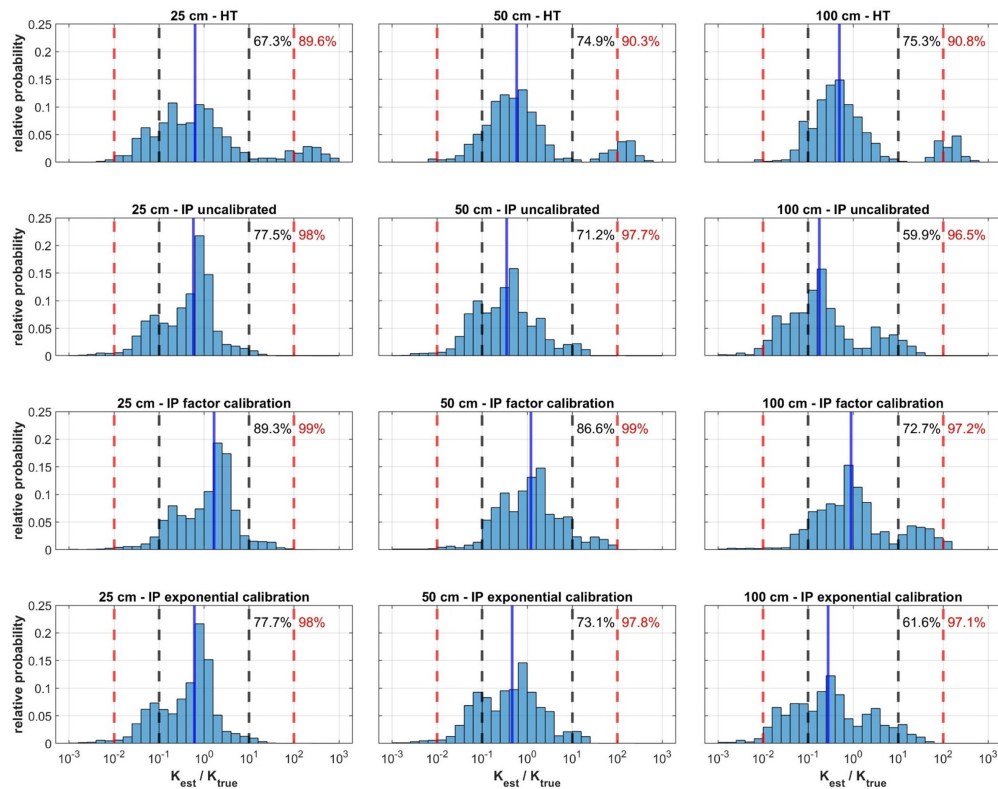


Figure 2.5: Histograms of $K_{\text{est}}/K_{\text{true}}$ (deviation of the inversion result from the true K -value for each cell) for the different methods, calibrations and spacings with the positions of the diagrams according to Figure 2.4. The blue vertical lines indicate the median value (ideally at $10^0 = \text{no deviation}$). The black (red) dashed lines show the one-(two-)order-of-magnitude-interval and the percentage indicates how many cells are within this range of deviation.

For the HT results a relatively broad distribution of prediction quality can be observed with approximately 90% of the values being within the 10^2 -interval and between 67% and 75% within the 10^1 -interval. A significant number of cells is strongly over-estimated, leading to a slightly bimodal distribution of the investigated ratio with a smaller second maximum around 10^2 . The median value is slightly smaller than 10^0 for all three spacings.

The uncalibrated IP results show a narrower distribution of prediction quality with 96.5% - 98% of the values within the 10^2 -interval. While the median value is close to 10^0 for the smallest electrode spacing, it is shifted to lower values with increasing spacing. At the same time, the percentage of values within the 10^1 -

interval decreases from 77.5% to 59.9%. Due to the low data density and strong regularization effects, a majority of the K -values gets significantly under-estimated with increasing spacing.

After performing the factor calibration this bias produced by the inversion is mostly corrected with all median values being very close to 10^0 and a much higher number of values can be found within the 10^1 -interval. However, the growing range of the distribution with increasing spacing cannot be removed by the calibration. The exponential calibration improves the prediction quality compared to the uncalibrated results, but is less successful than the factor calibration.

In the same way, a possible bias of the petrophysical laws underlying the inversion procedure might be corrected by the suggested calibration approaches. While the IP method is very well capable of retrieving the structural information correctly and giving a rough estimation of the expected trend in the K -values, the calibration using hydraulic information is being used for a more exact K -estimation. Still, it is important to note that the inherent scatter of the petrophysical laws cannot be removed and the achieved K -distribution remains an approximation of the reality within the limits of the accuracy of the petrophysical relations.

2.3.2 Transport Simulation

Snapshots of Tracer Plumes

Firstly, we evaluate the results of the transport modeling by imaging the tracer plumes that are simulated using the different inversion results as input data for the K -distribution. Fig. 2.6 shows an overview of snapshots taken at a simulation time of 50 days after starting the tracer injection for the different methods and calibrations as well as point spacings, arranged similarly to Fig. 2.4. The result for the original data set is given on the left side and we consider this to be the actual tracer concentration that would be observed in reality as a basis for comparison. The highly permeable zones (1) - (5) identified in Fig. 2.4 have produced fingering tracer plumes, that mostly extend as far as the center part of the domain ($x = 6 \dots 7$ m). Finger (2) inhibits some smaller variations due to the small-scale K -heterogeneities and finger (3) splits up into two thinner layers with high tracer concentration.

The HT results for 0.25 m and 0.5 m spacing correctly show all tracer fingers (1) - (5) with roughly the right extension and shape. Smaller features, as e.g., the variations in finger (2) or the splitting of finger (3), however, can hardly be made out. With 1 m spacing the two uppermost tracer fingers disappeared due to

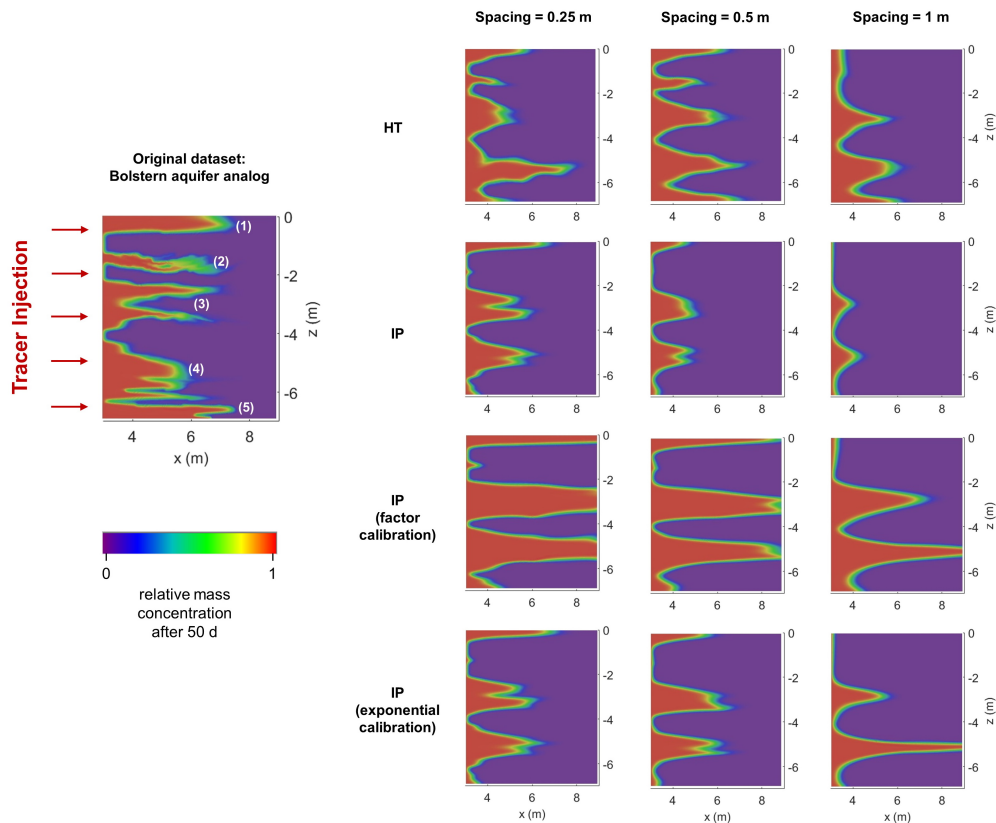


Figure 2.6: Transport modeling results for HT, IP and the two different IP calibrations for varying spacing of pumping locations / electrodes, given as images of relative mass concentration of the tracer injected in the left borehole. The result for the original data set of the Bolstern aquifer analog is given on the left for comparison. Here, the numbers (1) - (5) indicate the preferential flow paths identified in Fig. 2.4. All the plots show snapshots taken 50 days after starting the tracer injection. The same color bar applies to all images.

smoothing effects and the lack of pumping locations at the very top and only the fingers (3), (4) and (5) are modeled correctly.

Using the IP inversion results for the tracer prediction correctly reproduces the fingers (1), (3) and (4) with the right extension and shape. Some small-scale features, like the splitting of finger (3), are more realistic compared to HT. However, finger (2) gets strongly under-estimated due to smoothing effects, and layer (5) cannot be sensed due to the lack of quadrupoles in the lowest part of the domain. With larger spacing, the stronger influence of the smoothing effects becomes apparent.

The simulation with 1 m spacing can only reproduce the fingers (3) and (4), but they do not extend as far as they should. This indicates, that for cross-hole IP measurements a small enough electrode spacing is crucial to obtain reliable results.

The tracer prediction resulting from the factor calibration shows a clear over-estimation of K in the highly permeable layers with the fingers (1), (3) and (4) extending too far to the right. This effect is strongest for 0.25 m spacing, where the plume is already extending out of the domain at this time step. For the larger spacings, the images are at least closer to the reality than the uncalibrated results, although still somewhat over-corrected.

The best prediction of tracer plumes is achieved by the exponential calibration. For 0.25 m spacing the uncalibrated result has already been close to reality and it remains almost unchanged by the exponential calibration. A stronger effect of the calibration is visible for 0.5 m spacing, where the extension of the plumes is now predicted correctly. For 1 m spacing the result is still quite far from reality since the calibration cannot compensate for the lack in identified structures and the strong smoothing effects. Even so, there is a clear improvement compared to the uncalibrated result.

Tracer Breakthrough Curves

The depth-integrated relative tracer concentration over time at the central borehole ($x = 6$ m) is depicted in Fig. 2.7a-c. The concentrations were also recorded in the right borehole ($x = 9$ m), but all the main trends in the results are similar, so they are not further detailed here.

The breakthrough curve (BTC) for the original data set (red line) shows a relatively steep increase in tracer concentration within the first 150 days, which is stimulated by the highly permeable layers in the aquifer (layers (1) - (5) in Fig. 2.4 and 2.6). For later times, we observe a much slower increase in concentration as a result of the delayed propagation in the less permeable parts.

As a basis for comparison, we also show the BTC of a hypothetical homogeneous model with $K_{\text{eff}} = 7 \cdot 10^{-5} \text{ m s}^{-1}$ (red, dashed line). Here, we only observe a relatively quick incline of tracer concentration in the time span between 150 and 200 days. However, the true shape of the BTC cannot be reproduced, since no structural information on the sediments is processed. In contrast, all transport simulation results from HT and IP better approximate the true shape of the BTC. Apparently, the structural information gained from the two imaging techniques is valuable, even when just looking at depth-integrated BTCs. Especially the tracer

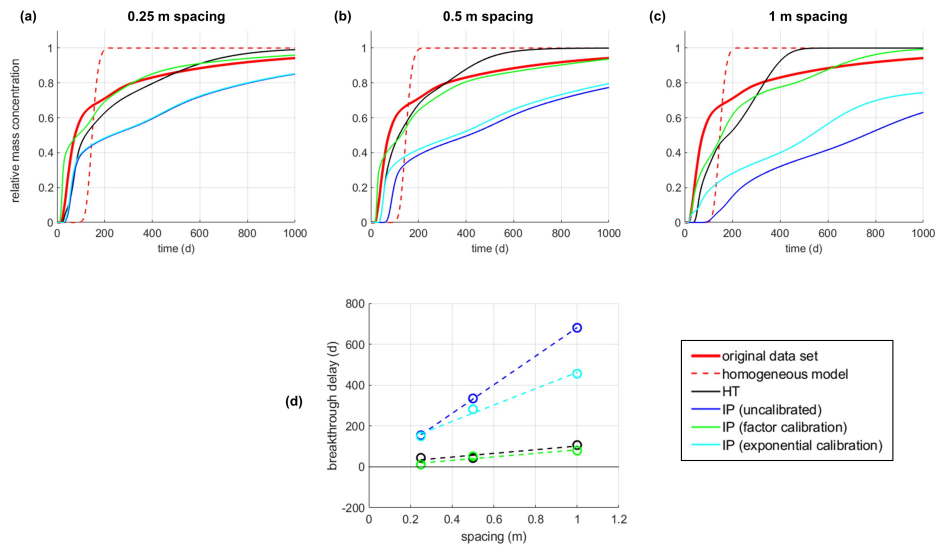


Figure 2.7: **(a) - (c)**: Depth-integrated tracer breakthrough curves at the center borehole ($x = 6$ m) resulting from different inversion results and calibrations compared to the original Bolstern data set (red solid line) and a hypothetical homogeneous model (red dashed line) for varying spacing of pumping locations / electrodes. **(d)** Breakthrough delay of the different methods and calibrations depending on the varying point spacing as a measure for the error of the transport simulations compared to the original data set. The dashed lines represent a linear regression between the data points for visual guidance only.

breakthrough at early times is strongly under-estimated by the homogeneous model.

The HT results (black lines) are successful in reproducing the whole BTC, although we observe a slight under-estimation of tracer breakthrough at early times and an over-estimation at late times. This can be interpreted as a result of smoothing effects, leading to a less pronounced distinction between areas with higher or lower K . It corresponds with the fact that this effect becomes stronger with increasing spacing, where smoothing effects have more impact.

Although the IP results (dark blue lines) correctly reproduce the general shape of the BTC (due to correctly retrieved structural information), they strongly underestimate the tracer breakthrough within the entire time span. Apparently, the tomograms are not accurate enough to be used for a transport simulation.

The exponential calibration (cyan lines) mainly corrects the early-time behavior of the BTC since only the highly permeable parts are changed by this calibration approach. Especially for the larger spacings (0.5 m and 1 m) this brings an advantage

compared to the uncalibrated result, whereas for the smallest spacing (0.25 m) almost no change can be observed. This is in agreement with the findings for the inversion results (Fig. 2.4) and the tracer plumes (Fig. 2.6). For the late times, the calibration does not compensate the under-estimation of tracer breakthrough. However, this is not caused by an under-estimation of K in the less permeable zones, since the slope of the BTC is correctly reproduced. Instead, the extension of high- K -zones is underestimated due to regularization (especially for large spacings) and therefore the early-time breakthrough reaches lower concentrations. This offset remains for the whole time span and leads to an overall under-prediction of tracer breakthrough.

The factor calibration (green lines) is more successful in correcting the IP results. Although the tracer concentration is over-estimated for early times, the long-term behavior is correctly predicted with a quality that is at least similar to the HT results. Applying the K_{eff} -value to the whole domain yields the best K -prediction in terms of average values and therefore the best reproduction of the complete BTC.

Finally, we assess the impact of the point spacing (electrodes or pumping locations) on the quality of the tracer breakthrough prediction. For this purpose, we pick a certain breakthrough time for all curves at the time where half of the relative concentration has been reached. We calculate the difference to the breakthrough time of the original data set and call this the breakthrough delay, considering it a rough measure for the error in the prediction of the BTC. The dependency of the delay on the spacing is shown in Fig. 2.7d. For all methods we observe an increase of the delay for increasing spacing due to a lower data density and stronger smoothing effects. This effect is only weakly pronounced for the HT results, indicating again that the point spacing is not as crucial and relatively good results can also be achieved with fewer pumping tests. On the other hand, the dependency on electrode spacing of the uncalibrated IP results is very pronounced, showing that a sufficiently small electrode spacing is particularly important to retrieve all the necessary structural information and gain good K -estimates. However, acquiring cross-borehole IP data with such small spacing in the field can be a very challenging task. Therefore, we consider the calibration with hydraulic data to be valuable especially when a larger spacing has to be used and therefore important structural information is not well resolved. While the exponential calibration can only slightly compensate for those problems, the factor calibration is very successful in reducing the breakthrough delay. Here, the results have a quality very similar to the HT data and the errors resulting from the large electrode spacing have been reduced significantly.

2.4 Conclusions

We have shown that both HT and IP are valuable tools for imaging K -heterogeneities in near-surface aquifers. The structural information of our test data set, the Bolstern aquifer analog, has been reconstructed by the inversion procedures to a high degree of resolution and quantitative accuracy. For the first time, the distribution of K could be computed directly from the IP data with our new IP- K inversion procedure and the general quality of the results is comparable to the HT travel time inversion. However, to achieve highly accurate K -estimates that allow using the results for groundwater modeling, we calibrate the results with hydraulic information. After the factor calibration, the depth-integrated tracer BTCs of the original data set could be reproduced. Imposing K_{eff} on the whole domain leads to a good prediction of the long-term behavior of tracer breakthrough. On the other hand, the exponential calibration is more suitable to correctly predict the tracer plumes at early times. Therefore, in practice it would be necessary to decide on one of the calibrations depending on how the data will be used later on. Both calibrations may not only correct regularization-induced errors in K -prediction, but also a possible bias of the petrophysical laws that link electrical and hydrological parameters. Although we cannot account for the inherent scatter of the petrophysical relations, we still consider those calibrations to be highly valuable tools within the processing of IP data. While the structural features of an aquifer can be accurately retrieved with IP, hydraulic information is essential for a reliable K -quantification.

Future research should focus on testing the suggested methodology within field experiments. The new IP- K inversion procedure for IP data has already been tested on borehole data (Fiandaca et al., 2021) and 2D surface profiles from five different European countries (Martin et al., 2021), giving K -values within one decade from slug tests / grain size analysis estimates. However, no benchmarking of the field K -estimates for flow and transport modeling or tracer experiments have been conducted yet.

Ideally, future field experiments should follow a similar concept as presented in this study (Fig. 2.1). Conducting both HT and IP experiments at the same site would allow a direct comparison of the performance of the methods in the field. Furthermore, the pumping tests carried out for the HT survey could provide the K_{eff} -value needed for the IP calibrations. Finally, the quality of the achieved K -images might also be tested by tracer experiments.

On the other hand, field campaigns with limited financial and time resources may

now also rely on IP measurements alone (together with one or just a few pumping tests for retrieving K_{eff}) following the suggested calibration methodology. While a full HT experiment is often very time-consuming and costly, IP measurements can mostly be conducted within a few hours (in a setting similar to the example shown in this work). Therefore, a detailed characterization of aquifer heterogeneities in the field might become more convenient by applying our IP- K inversion procedure and the results can be expected to have a similar quality compared to HT.

However, the two calibration approaches suggested in this work should only be regarded as a starting point. In a real field environment, further elaborated calibration methods might turn out to be more successful. Furthermore, stronger data integration approaches between hydraulic and geophysical methods are expected to yield even better results. While hydraulic methods are often most sensitive to preferential flow paths, IP generates the strongest polarization response in areas of low K . We therefore see a big potential in using the complementary sensitivities of the two methods by a stronger integration of the data. Ultimately, a fully-joint inversion of HT and IP data sets might open the door to an improved ability of imaging hydraulic conductivity in near-surface aquifers.

Research Data

The original Bolstern data set as well as all HT and IP inversion results are available through <https://doi.org/10.5281/zenodo.6361423>.

III.

Hybrid discrete fracture network inversion of hydraulic tomography data from a fractured-porous field site

Lukas Römhild¹,
Lisa Maria Ringel¹,
Quan Liu²,
Linwei Hu^{3,4},
Thomas Ptak²,
Peter Bayer¹

¹ Institute of Geosciences and Geography, Martin Luther University Halle-Wittenberg

² Faculty of Geosciences and Geography, University of Göttingen

³ Institute of Geosciences, Christian Albrechts University Kiel

⁴ GeoAnalysis-Engineering GmbH, Schauenburgerstraße 116, 24143, Kiel

Water Resources Research 60 (2024) e2023WR036035

<https://doi.org/10.1029/2023WR036035>

Abstract

The accurate characterization of hydraulic conductivity heterogeneities in an aquifer is crucial for predicting flow and transport processes correctly. Hydraulic tomography (HT) experiments are often used to infer the hydraulically relevant features, but the correct inversion of the data remains a challenging task. We implemented a discrete fracture network (DFN) inversion approach that is expanded by considering a nonzero matrix permeability. The hybrid model allows the accurate characterization of fractured-porous sites by taking into account both matrix and fracture flow. This novel inversion algorithm is successfully applied to HT data acquired at a field site in Goettingen (Germany), and the results are compared with those of a standard travel time inversion. Furthermore, we validate the inversion results by using them as the underlying material parameters for simulating heat tracer experiments and comparing the modeled temperature responses with those of heat tracer tests actually conducted at the site. It is shown that the DFN ensemble predicts the thermal response of the experiments correctly for the two major fractures in terms of location, amplitude, and time-dependent behavior of the temperature anomaly, as long as the stochastic nature of the results is taken into account. We conclude that considering both matrix and fracture flow in a hybrid DFN inversion approach can lead to significant improvements in flow and transport modeling at fractured-porous sites.

3.1 Introduction

The prediction of flow and transport behavior in aquifers is relevant for many applications in subsurface engineering and hydrogeology, such as geothermal energy, management of groundwater resources, and storage of hydrogen or methane (Attard et al., 2020; Gasanzade et al., 2021; Li et al., 2022a). However, the accuracy and reliability of the prediction depend on the characterization of the subsurface heterogeneity. Various tomographic methods have been established for imaging the distribution of hydraulic properties. Among these methods, hydraulic tomography (HT) is based on sequentially injecting (or extracting) water in one borehole interval and monitoring the transient pressure or hydraulic head response in other nearby intervals at different depths (Yeh & Liu, 2000). The tomographical configuration created by this setup is inspired by geophysical tomography methods such as crosswell seismic or electrical resistivity tomography (Bing & Greenhalgh, 2000; Binley & Slater, 2020; Bregman et al., 1989). However, in contrast to geophysical methods, HT provides a direct link between the measured signals and the hydraulic properties of the fracture network or the porous media (Day-Lewis et al., 2017). All pressure responses measured at the observation points can be used to invert the stratigraphic structures, i.e., the spatial distribution of hydraulic diffusivity, specific storage or hydraulic conductivity.

In general, two conceptual models are available for the inversion of the hydraulic head responses: the heterogeneous continuum model and the discrete fracture network (DFN) model. The application of a continuum model results in a spatial (element-wise) distribution of hydraulic parameters. It is assumed that the heterogeneities in hydraulic parameters are attributed exclusively to matrix flow, meaning that individual (discrete) fractures cannot be inferred. The continuum model is well established for the characterization of porous and fractured sites (e.g., Berg & Illman, 2011; Cardiff et al., 2013, 2020; Fischer et al., 2017; Illman et al., 2009; Liu et al., 2022; Luo et al., 2023; Ren et al., 2021; Somogyvari & Bayer, 2017; Tiedeman & Barrash, 2020; Zha et al., 2015; Zhao et al., 2019, 2023) and several inversion methods have been developed based on this concept. While geostatistical approaches can generate tomograms for both hydraulic conductivity (K) and specific storage (S_S) and often produce the best results for drawdown predictions, continuum-based travel time inversion only yields diffusivity (D) tomograms, but allows for the accurate characterization of high- D zones with less hydraulic data being required for the inversion (Qiu et al., 2023). In particular, travel time inversion

is considered a more efficient inversion approach in terms of computational costs and less reliance on a forward model for evaluating the error between simulated and measured data (Brauchler et al., 2003, 2013b; Hu et al., 2011; Liu et al., 2022; Yang et al., 2020). Thereby, potentially insufficient initial and boundary conditions can be avoided.

Further insights into the properties of fracture networks can be gained by implementing a DFN model for the inversion. The hydraulic properties of a predefined DFN structure (Klepikova et al., 2014, 2020), the structural properties (Somogyvári et al., 2019), or structural and hydraulic properties of DFNs (Fischer et al., 2020; Ringel et al., 2022) can be estimated. Typically, the contribution of the matrix to the flow is neglected in the DFN model, but the approach can infer individual (discrete) fractures based on the HT data.

In this study, we investigate the HT-based characterization of a fractured-porous field site. This category of aquifers can be of great relevance for geothermal applications (e.g., Bauer et al., 2017; Boersma et al., 2021; Huang et al., 2021; Kushnir et al., 2018). Reliable inversion results can help optimize the planning and operation of these sites. For that purpose, we develop a novel inversion strategy using a hybrid DFN model. It is based on a DFN inversion algorithm that has been applied for fractured crystalline rock masses assuming an impermeable rock matrix (Ringel et al., 2021, 2022; Somogyvári et al., 2017). However, at fractured-porous sites the characteristics of purely fractured rocks and a porous rock matrix with considerable permeability are combined and therefore it might not be sufficient to rely on either a continuum model or a DFN model alone. Instead, a combined (hybrid) approach considering flow in both discrete fractures and the porous matrix becomes necessary (Fischer et al., 2020). Therefore, the objective of this study is to expand the existing DFN inversion approach by the implementation of a hybrid model with a nonzero matrix permeability. We demonstrate this methodology for HT experiments conducted at the fractured rock experimental site located at the campus of the University of Göttingen, Germany, and compare the results with those obtained by using a continuum model alone.

This paper is structured as follows: subsequently, a description of the field site, the conducted HT experiments, and the fundamentals and implementations of both inversion algorithms are presented (Chapter 3.2). Afterwards, we evaluate the inversion results in Chapter 3.3 and validate the results by predicting and comparing the measured data of independently conducted heat tracer tests at the field site in Chapter 3.4. The results are discussed in Chapter 3.5, where we also present a com-

parison between the continuum model and the hybrid DFN approach. A conclusion of our findings is given in Chapter 3.6.

3.2 Methods

3.2.1 Site description and data acquisition

The experimental site is located at the north campus of the University of Göttingen, Germany (Fig. 3.1a), at the eastern shoulder of the Leinetalgraben, which is a distinctive zone of subsidence in the southern part of Lower Saxony, Germany. The geological structure is complex due to polyphase tectonic development under various tension forces. Lithologically, the area is located in the Lower and Middle Keuper, which mainly consists of clay sequences and silt-sandstone layers.

The lithological situation of the site has been described in Werner (2013) based on drill cores. The top 14 m are composed of quaternary limestones and claystones with mineralizations of quartz, feldspar, and calcite. Below this depth, different types of consolidated sediments of the Middle Keuper can be found, starting with red and grey siltstones as well as fine sandstones between 14 m and 24 m, with a high abundance of calcite mineralizations. Between 24 m and 42 m, grey claystones as well as siltstones are present, again with calcite mineralizations, but also iron oxide films and small amounts of mica. An alternation of different silt- and claystones continues until 64 m depth, where the Lower Keuper begins. For more details about the geological setting and the lithology we refer to Werner (2013).

Since 2013, five groundwater wells arranged in a cross shape have been installed at this site (Fig. 3.1b). Each well is 80 m deep and the horizontal distances from the middle well to other wells are between 1.9 m and 3 m. To hydraulically connect to the surrounding strata at different depths, each well was fitted with nine separate filter sections. Each filter screen is 5 m long and installed in alternation with a 3 m impermeable filter section backfilled with clay, except for the 8 m long casing at the top of the well (Fig. 3.1c). Therefore, tomographic pumping tests can be performed independently between different filter sections of the test and observation wells, which are hydraulically isolated by the double-packer system. Also, fiber-optic cables were pre-buried outside each wellbore in order to observe the temperature changes along the wells at high resolution during thermal tracer tests. Based on previous studies including geophysical borehole logging (Werner, 2013), flowmeter logging (Liu, 2022), long-term heat injection tests (Baetzel, 2017), and hydraulic tests (Qiu, 2020; Yang et al., 2020; Liu et al., 2023), the hydraulic connection

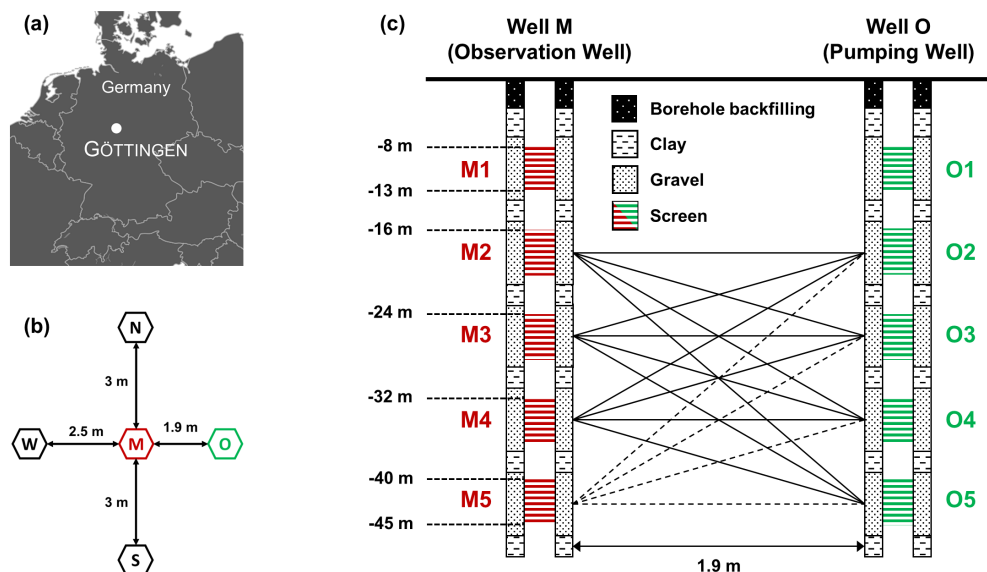


Figure 3.1: **(a)** Location of the field site in Göttingen within Central Europe. **(b)** Setup of the wells at the field site. **(c)** Tomographic configuration of the HT experiment with pumping screens in green and observation screens in red colors. The data recorded at M5 were not used due to high noise levels (dashed ray paths).

between wells M and O in the upper 45 meters seems most significant and several transmissive fractures can be inferred. Therefore, the cross-well area between wells M and O in the upper 45 meters will be the focus of this study (Fig. 3.1c).

The HT experiments were conducted in April 2018 as a series of cross-well multi-level pumping tests. A submersible pump (Grundfos MP1) was used to extract groundwater from isolated intervals in well O with a pumping rate of approximately 30 l min^{-1} (the exact rate for each test was recorded and could be used in the forward model of the hybrid DFN inversion). The resulting drawdown data were recorded by pressure transducers (“Druck” pressure sensors with an accuracy of $1 \text{ mmH}_2\text{O}$ and a temporal resolution of 20 ms) in both the pumping well O and the observation well M in the intervals separated by the double packer systems. The pumping tests were conducted in four different intervals (O2-O5), and for each test the resulting pressure response was recorded in the respective four intervals (M2-M5) in the opposite borehole, thereby creating a tomographic configuration. Drawdown data were also recorded in the pumping well O, but they are strongly affected by the three-dimensional diffusion of the pressure perturbation (radially,

assuming an isotropic medium), which is not included in the 2D forward model. Therefore, these data are not used within this work. Furthermore, the pressure signal at observation interval M5 is extremely noisy and was therefore excluded from the further processing and inversion (dashed lines in Fig. 3.1c). Therefore, the used data set consists of 12 different pressure response curves (red lines in Fig. 3.4). More information about the field experiments can be found in Yang et al. (2020).

3.2.2 Continuum-based travel time inversion

The hydraulic travel time of a pumping test can be defined as a line integral between a source point x_1 (where the pumping-induced pressure is generated) and a receiver point x_2 (at which the resulting pressure response curves are recorded). It is assumed that the signal travels along the path ε , which minimizes the travel time based on the given distribution of diffusivity D [$\text{m}^2 \text{s}^{-1}$] in the subsurface:

$$\sqrt{t_{\alpha,h}} = \frac{1}{\sqrt{6f_{\alpha,h}}} \int_{x_1}^{x_2} \frac{d\varepsilon}{\sqrt{D(\varepsilon)}}, \quad (3.1)$$

where $t_{\alpha,h}$ [s] is the hydraulic travel time and $f_{\alpha,h}$ is a conversion factor (Brauchler et al., 2003). The subscript h indicates the usage of a Heaviside source. The travel time of the signal is obtained by selecting the maximum of the absolute value of its first derivative (see Fig. 3.2a). In order to calculate this derivative, the raw data have to be denoised to create a smooth pressure response curve. For this purpose, we employed the wavelet method and polynomial regression as reported in Yang et al. (2020). Although the duration of the experiments is relatively long (between 300 s and 3000 s pumping duration), the travel time can typically be found within the first seconds of the signal (see Fig. 3.2b).

Similar to the seismic travel time inversion, Eq. 3.1 is resolved using ray tracing techniques, and the inverted slowness can be converted to the hydraulic diffusivity D . In this study, the open-source framework pyGIMLi is utilized to invert the hydraulic travel times, which is based on the generalized Gauss-Newton method (Günther et al., 2006; Rücker et al., 2017) and where the forward operator for calculating the travel times uses Dijkstra's algorithm (Dijkstra, 1959). As a final step, the diffusivity D might be converted to hydraulic conductivity K [m s^{-1}] by multiplying with specific storage S_s [m^{-1}]:

$$K = D \cdot S_s. \quad (3.2)$$

The spatial distribution of S_s can be inferred from hydraulic attenuation inversion (Brauchler et al., 2011; Song et al., 2023), but it is often assumed homogeneous by using literature values. Within this study, we use a constant specific storage of $S_s = 5 \cdot 10^{-5} \text{ m}^{-1}$ based on average values from Qiu (2020).

For performing the inversion, a uniform rectangular grid with a vertical resolution of 0.5 m and a horizontal resolution of 1 m is used. The relatively coarse resolution is chosen to account for the low data density produced by the limited number of source and receiver positions. The model space using this grid consists of 150 cell values, while the data space is made up by only 12 travel times. Therefore, an even finer resolution would pretend an accuracy of the result that is not actually supported by the data. Furthermore, the rectangular (non-square) cells are helpful to reproduce the horizontal layering typical for sedimentary environments, without the need to apply anisotropic constraints within the inversion. While the pumping and observation intervals have a relatively long vertical extension (red and green lines in Fig. 3.2c), the source and receiver positions are only modeled as points that are set at the top or bottom of the interval (black dots in Fig. 3.2c). Since the travel time inversion is generally most sensitive to the shortest path of the signal, the receiver points are placed at the position that minimizes the distance to the respective pumping location. Consequently, since results from a travel time inversion can only cover the domain between source and receiver points, no diffusivity information can be obtained for the area between the deepest intervals (-40 m to -45 m), as well as beyond the pumping and observation locations in horizontal direction.

3.2.3 Hybrid DFN inversion

Forward simulation and numerical model

Since the HT data were acquired at a fractured-porous field site, a hybrid DFN model, also called discrete fracture matrix (DFM) model, is applied for the simulation of the HT experiments (Berre et al., 2019). This conceptual model integrates larger and more permeable fractures directly while smaller and less conductive fractures are considered by the hydraulic conductivity and specific storage of the matrix elements. Flow in the fracture network and the porous media is governed by Darcy's law and the continuity equation. The porous medium is modeled as 2D continuum:

$$S_s \frac{\partial h}{\partial t} - \nabla \cdot (K \cdot \nabla h) = Q \quad (3.3)$$

with the following initial and boundary conditions:

$$h|_{t=0} = 0, \quad h|_{\Gamma_1} = 0, \quad (K \cdot \nabla h) \cdot \mathbf{n}|_{\Gamma_2} = 0. \quad (3.4)$$

Here, h [m] is the hydraulic head, Q [s^{-1}] is a source/sink term, Γ_1 comprises the left and right boundary of the domain, Γ_2 the top and bottom boundary, and \mathbf{n} is a normal vector on the respective boundary.

Fractures are reduced to 1D discrete lines assuming a constant hydraulic head normal to the fracture plane:

$$a_f S_{s,f} \frac{\partial h}{\partial t} - \nabla_T (a_f K_f \nabla_T h) = a_f Q, \quad (3.5)$$

where a_f [m] is the fracture aperture. The gradient ∇_T is evaluated in the fracture plane. The subscript f always refers to fracture parameters (in contrast to porous media parameters).

The finite element method (FEM) is applied for the numerical solution of Eq. 3.3, 3.4, and 3.5. Intersections between different fractures and between fracture and matrix are considered by a conforming mesh discretization which imposes continuity of the head and balance of the fluxes (Woodbury & Zhang, 2001). The mesh discretization for the computational domain including the boreholes and the fracture network is implemented utilizing the open source mesh generator *Gmsh* (Geuzaine & Remacle, 2009).

Solution of the inverse problem

The inversion of the HT data is based on a stochastic approach. Accordingly, the DFN parameters θ (a parameter set containing position, size, and hydraulic conductivity K of the fractures, see Table 1) are interpreted as random variables characterized by their posterior distribution $p(\theta|\mathbf{d})$. The Bayesian equation relates the posterior distribution, considering a set of measured HT data, to the likelihood of the modeled data for a given DFN realization and the prior information of the DFN parameters. The likelihood function L evaluates the error between the measured HT data \mathbf{d} and the HT signals $F(\theta)$ simulated by the forward model:

$$\log L(\mathbf{d}|\theta) \propto - \sum_{i=1}^N \frac{(d_i - F(\theta)_i)^2}{2\sigma_i^2}, \quad (3.6)$$

where σ is the data variance estimated by Gibbs sampling, as in previous works (Ringel et al., 2019, 2022). The posterior distribution of the DFN parameters is evaluated by generating samples from the distribution according to Markov chain Monte Carlo (MCMC) methods. This results in a set of DFN realizations that are equally likely by adjusting the structural and hydraulic properties of the DFN. Starting from an initial DFN realization, the DFN parameters are updated iteratively by proposing a new parameter set θ' with a proposal distribution q based on the current realization of the DFN. This parameter set is accepted or rejected according to the update probability:

$$\psi = \min \left(1, \frac{p(\theta'|\mathbf{d})}{p(\theta_{i-1}|\mathbf{d})} \frac{q(\theta_{i-1}|\theta')}{q(\theta'|\theta_{i-1})} \right). \quad (3.7)$$

Insertion or deletion of a fracture is a so-called transdimensional update following the reversible jump MCMC algorithm (Green, 1995). Additionally, parameter updates can be applied that adjust position, length, or hydraulic conductivity of the fractures. More information about this DFN inversion approach can be found in Ringel et al. (2022).

Implementation of the inversion

The computational domain comprises a rectangle covering the depth range between 0 m and -60 m in vertical (z-) direction and a horizontal (x-) extension between -10 m and 12 m. The two boreholes are located at $x = 0$ m and $x = 1.9$ m, so that the distance between both boreholes and the corresponding boundary of the domain is approximately 10 m. This distance ensures that boundary effects of the model directly affecting the relevant hydraulic signals are negligible, but long fractures are still able to connect the boundary conditions with the boreholes to simulate the interaction with the parts of the aquifer not included in the computational domain. As shown in Eq. 3.4, these boundary conditions on the left and right side of the domain were implemented as zero head boundaries due to the negligible natural flow conditions at the site. At the top and bottom of the domain, no-flow boundary conditions are employed. The initial hydraulic head is set to zero within the whole domain.

The pumping intervals are implemented as 1D line source elements using the exact vertical extension according to the field experiments (Figure 3.1c). The resulting pressure response curves are achieved by integrating over the volume of the borehole intervals (using the exact borehole radius and vertical extension), so that

the contributions of all fractures crossing the respecting intervals, as well as the matrix, are considered.

The pumping duration and extraction rates of the individual hydraulic tests are implemented according to the actual field experiment. However, only the first 100 s of the signals were evaluated within the inversion. This early time span is the most dynamic part of the response and contains almost all necessary information about the subsurface hydraulic parameters (e.g., Hou et al., 2023). Also, using the complete signal for the inversion procedure would significantly increase the computational cost.

For modeling flow in the porous medium, we assign a hydraulic conductivity of 10^{-6} m s^{-1} and a specific storage of $5 \cdot 10^{-5} \text{ m}^{-1}$ to the matrix. These values are based on earlier results of single-well multi-level pumping tests and corresponding type curve analysis, which give a range of possible values for both parameters (e.g., between $3.4 \cdot 10^{-7} \text{ m s}^{-1}$ and $1.3 \cdot 10^{-6} \text{ m s}^{-1}$ for K , based on Qiu (2020)). A more detailed discussion of the selected matrix parameters is contained in section 3.3.4.

The inversion algorithm works with a limited number of distinct fracture sets that are each characterized by a fixed fracture orientation angle. Based on data from an optic televiewer system, three major orientations of the fractures were identified by an earlier study (Werner, 2013) in terms of azimuth and dip angle: $351^\circ/6^\circ$, $221^\circ/37^\circ$, and $45^\circ/59^\circ$. By projecting these planes into our 2D domain, we obtain the following dip angles: -0.94° , -26.31° , and 49.64° .

At the beginning of the inversion process, an initial DFN has to be defined as the starting model. While some of the initial fractures are manually inserted to ensure connectivity to the boundary conditions, as well as between the pumping and observation intervals for the first iteration, a number of randomly generated fractures is also added. All of the initial fractures belong to one of the three fracture sets mentioned above, meaning that the orientation angles of the initial DFN are based on the three different angles from the televiewer data (Werner, 2013), and they remain fixed throughout the inversion process. Each orientation is chosen with a probability of $\frac{1}{3}$ when generating the initial DFN, and also when inserting a new fracture during the inversion process.

To evaluate the influence of the starting model, we performed several inversions with different initial DFNs in parallel. It could be observed that all inversions end up at similar posterior DFN ensembles despite large differences in the starting model. In all cases, none of the initial fractures remains untouched by the inversion. Instead, most of the direct interval connections are actually deleted and replaced by

parameter	minimum	maximum
x-position of the fractures mid-point	-8 m	10 m
z-position of the fractures mid-point	-46 m	-15 m
length of the fracture	0.5 m	10 m
hydraulic conductivity of the fracture	10^{-4} m s^{-1}	10^0 m s^{-1}

Table 1: Minimum and maximum values for the prior distribution of fracture parameters.

more indirect connections by a combination of several fractures. A lot of other initial fractures undergo significant changes in position and size during the inversion procedure.

All fractures in the model are assumed to be straight lines characterized by an aperture of 0.002 m (Liu et al., 2022) and a specific storage of 10^{-5} m^{-1} . While those two parameters remain fixed during the inversion, the hydraulic conductivity K as well as location and length of the fractures are regarded as inversion parameters. The minimum and maximum values used for the prior distribution of those parameters are summarized in Table 1.

Note that hydraulic conductivity is assumed to be constant within each individual fracture. The minimum and maximum number of fractures for a DFN are set to 20 and 200, respectively, while the latter has never been reached during the inversion process. The prior distributions also apply as proposal functions for the insertion of a fracture. For the deletion of a fracture, one fracture is randomly chosen from a uniform distribution over the number of fractures. In the case of a parameter update, the proposal distribution is a normal perturbation of the current value with a given standard deviation.

3.3 Inversion results

3.3.1 Travel time inversion result

The result from the continuum-based travel time inversion of the HT data is shown in Fig. 3.2c. The tomogram is evaluated in terms of diffusivity D , since this parameter is the direct result of the inversion and no conversion to hydraulic conductivity (Eq. 3.2) has been performed at this stage. In the result, most areas have diffusivity values between $0.1 \text{ m}^2 \text{ s}^{-1}$ and $10 \text{ m}^2 \text{ s}^{-1}$. However, there is one distinct high-

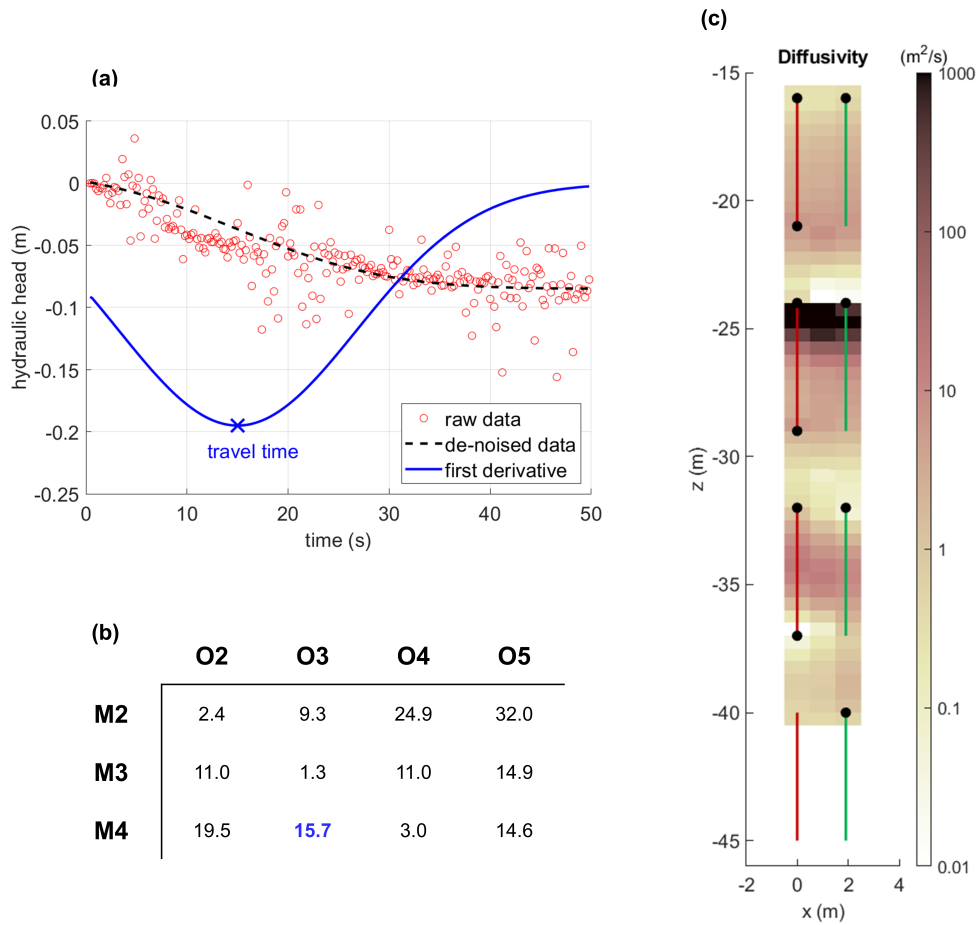


Figure 3.2: **(a)** Example for pressure response curves of the HT experiment and travel time processing. The raw data (red curve) are first denoised (black, dashed line), before the maximum of the first derivative (blue line) is picked as the travel time for the corresponding ray path. **(b)** Table with the derived travel times (in seconds) for all source-receiver combinations. The travel time from plot (a) is marked in blue. **(c)** Result of the travel time inversion in terms of diffusivity D . The green and red lines represent the pumping and observation intervals, respectively, whereas the black dots visualize the assumed source and receiver points for calculating the ray paths.

diffusivity zone at the depth of -25 m that connects the intervals M3 and O3. Clearly, a strong hydraulic connectivity was established between those intervals, but the exact depth of this connection remains unclear. The inversion algorithm places the high-diffusivity zone at the top of the interval, since the source and receiver

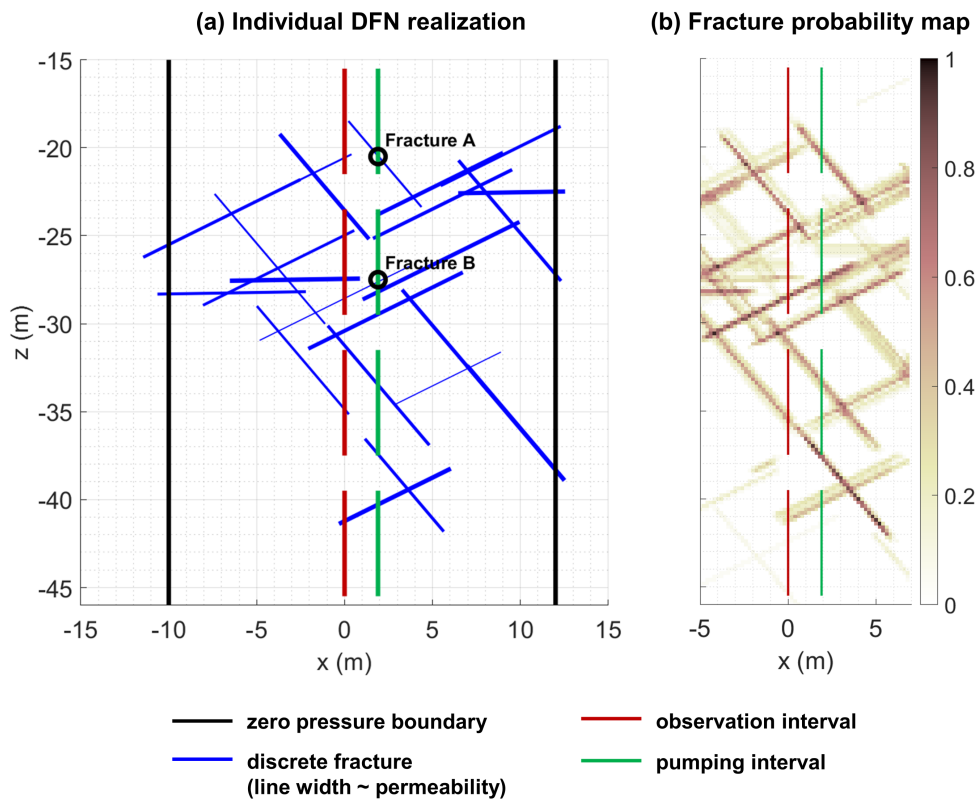


Figure 3.3: **(a)** Individual DFN realization from the last iteration of the inversion. The black lines represent the zero pressure boundary conditions (the no-flow boundaries at the top and bottom are not shown here), while green and red lines are pumping and observation intervals, respectively. The blue lines visualize the individual fractures of the DFN with the width of the line indicating the individual permeabilities. **(b)** Fracture probability map generated from the posterior ensemble of the hybrid DFN inversion.

points are positioned there in the forward model. In the field experiments, the complete intervals function as sources and receivers, so the connection could also be located at the bottom of these intervals (e.g., around -28 m). Therefore, it is not possible to derive the exact depth of the hydraulically relevant features using the continuum-based travel time inversion in combination with this specific field setup.

3.3.2 Hybrid DFN inversion results: individual realizations

Firstly, we show the DFN realization of the last iteration as one example of the posterior ensemble in Fig. 3.3a. This network consists of 23 individual fractures, with

three of them being part of the first fracture set (dip angle -0.94° , almost horizontal lines in the plot), eleven of the second fracture set (-26.31°) and nine of the third fracture set (49.64°). The hydraulic conductivity of the fractures is visualized by the width of the blue lines and ranges from 0.25 m s^{-1} to 0.99 m s^{-1} . All these values are close to the upper limit for K used within the inversion (1 m s^{-1}), so that even the relatively thin lines in the plot are fractures with a hydraulic conductivity significantly higher (around five orders of magnitude) than the matrix.

All fractures of this realization have a connection to the entirety of the network, either by other fractures or by the two boreholes. There are two fractures that connect the network to the left boundary and four fractures establish the connection to the right boundary (black lines). Only one direct connection between two opposite intervals can be found (marked as fracture B in Fig. 3.3a), which corresponds with the high-diffusivity zone identified in the travel time inversion result (Fig. 3.2c). However, many more connections between other intervals (also in vertical direction) are established in indirect ways by the interplay of several fractures. In some cases, fractures end very closely to one of the intervals, leaving a little gap, where the hydraulic connection is maintained by flow through the matrix (e.g., fracture A is very close to the pumping interval, but still leaves a small gap). In these cases, the combined fractured-porous approach is of great importance.

A comparison of the measured HT data with the modeled data based on the last DFN realization is shown in Fig. 3.4. Overall, a good data fit has been reached for the first 100 s of the signal. The hydraulic head towards steady-state conditions has mostly been simulated correctly with values between -0.1 m and -0.15 m . Only for combination O2-M4, the misfit between measured and simulated data at the last shown time step is significant. In other cases, the slope of the simulated curves is not entirely correct (e.g., combination O3-M3, where the drop in hydraulic head is actually much slower, but in the end, the same steady-state level is reached). This could be explained by an underestimation of the specific storage in either the matrix or the fracture network by the inversion but might also be a result of possible 3D effects in the experiment that are not accounted for in the 2D forward model. However, with respect to the high noise level of the measured data, the simulated pressure response curves can be regarded as satisfactory.

3.3.3 Hybrid DFN inversion results: fracture probability map

The high number of DFN realizations (samples from the posterior ensemble) requires the evaluation of the inversion result as a fracture probability map (FPM). Due

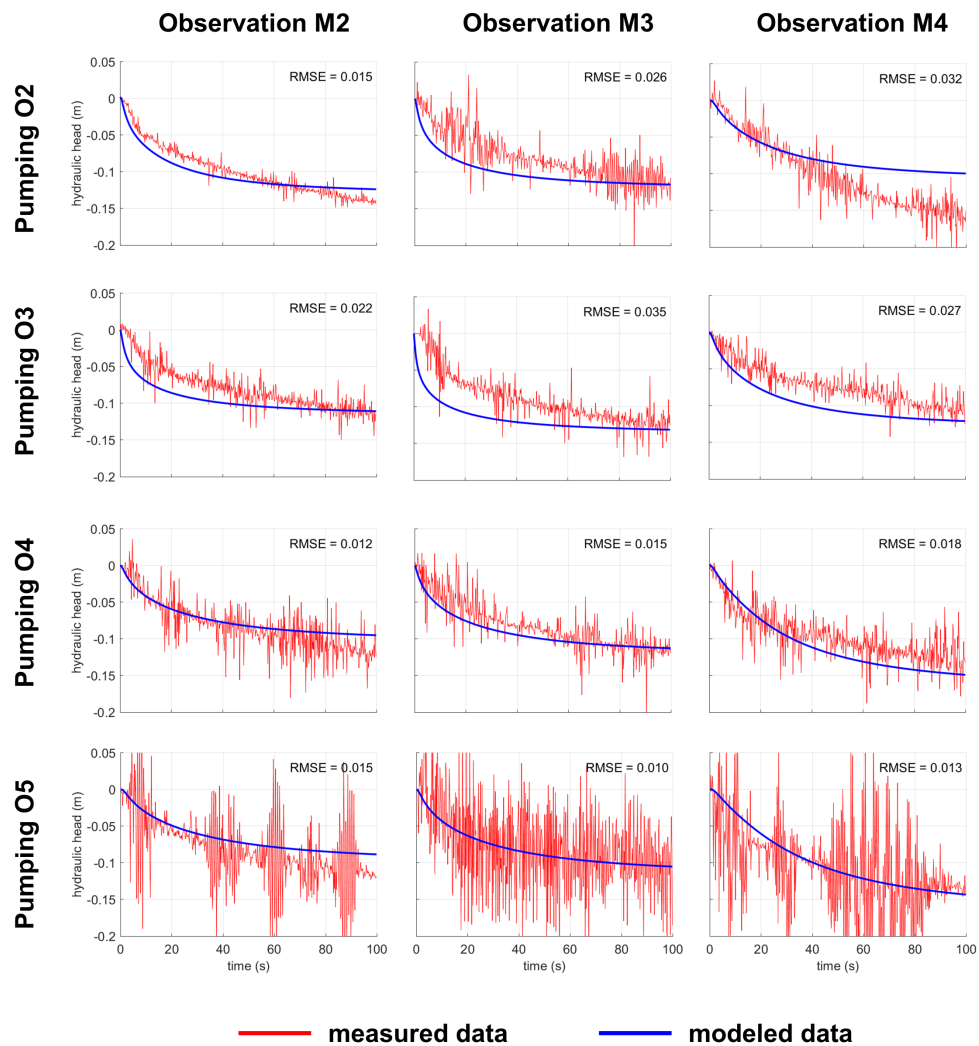


Figure 3.4: Measured (raw) data of the HT experiments (red lines) and modeled pressure response curves for the last iteration of the hybrid DFN inversion (blue lines). Only the first 100 s of the signal are used within the inversion procedure. The RMSE values (in m) shown in the plots are calculated using smoothed pressure response curves to eliminate the effect of noise on the RMSE. However, within the inversion procedure, the raw signal is used to include the uncertainty of the data.

to the large ensemble size and the strong similarity of consecutive realizations, the method of sequence thinning (Somogyvári et al., 2017) was used to select realizations that show significant differences. We use every 100th realization of the last 2500 iterations of the ensemble. A raster with 0.2 m resolution is generated for

each DFN realization and the values 1 and 0 are assigned to the individual raster elements, based on whether a fracture is present or not. By computing the mean of all rasters for the chosen DFNs, the FPM is created, showing the probability (between 0 and 1) for each raster element to be part of a fracture. The variations in hydraulic conductivity among the different fractures are not considered in the FPM.

Fig. 3.3b shows the resulting FPM. The individual realization from Fig. 3.3a can clearly be identified in the FPM as well, and deviations within the posterior ensemble are relatively minor. There is a limited number of fractures that only appear in some realizations (e.g., in the lower left corner). Instead, most of the fractures only undergo small positional changes (blurry areas in the FPM) or are almost not being shifted at all (dark lines in the FPM). All of those fractures are in some way connected to pumping/observation intervals or to the boundary, so that they are hydraulically relevant and therefore crucial to fit the data properly.

A zone with a particularly high fracture density can be identified around the second pair of intervals (between -22 m and -30 m, approximately). Here, the fracture network establishes a strong hydraulic connectivity between the opposite intervals and beyond (to the boundary). Again, fracture B appears as a very prominent feature that directly connects the intervals and is characterized by very high probabilities (dark colors) in the FPM. This zone of high fracture densities is in good agreement with the continuum-based inversion result (Fig. 3.2c) that indicates a high-diffusivity zone in a similar depth range. Above and below these depths, a lower fracture density can be observed, with only a few distinct fractures being hydraulically relevant. Outside the area covered by the intervals, no fractures are being inserted by the inversion algorithm due to the absence of hydraulic data.

3.3.4 Influence of matrix characteristics

Within the hybrid DFN inversion approach, selecting the correct hydraulic conductivity of the matrix plays a key role. As stated previously in section 3.2.3, we assign a hydraulic conductivity of 10^{-6} m s^{-1} to the matrix based on earlier findings of Qiu (2020). Generally, fitting some of the data by analytical solutions can help to find a good initial guess for the matrix parameters.

However, alternative matrix characteristics were also tested to evaluate their influence on the inversion results. If, on the one hand, the value for matrix- K is chosen too high, flow in the porous phase alone might explain the measured hydraulic data and therefore almost no fractures are inserted by the inversion algorithm. In this

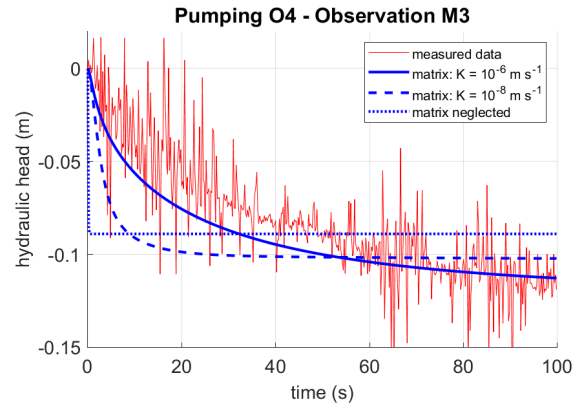


Figure 3.5: Influence of matrix parameters on the inversion results. Choosing a hydraulic conductivity of 10^{-6} m s^{-1} for the matrix results in the smallest misfit (solid, blue line), e.g., compared to a lower K -value of 10^{-8} m s^{-1} (dashed, blue line), and especially compared to a classical DFN inversion neglecting the matrix completely (dotted, blue line). For the complete results of all source receiver combinations, we refer to section A.3 (S1 and S2).

case, the matrix hydraulic conductivity is already an average value that contains both the porous and the fractured part. If, on the other hand, K of the matrix is chosen smaller, seemingly reasonable DFNs are generated by the inversion, but the experimental data cannot be fitted with the same accuracy. This trend is illustrated by Figure 3.5: When selecting a lower hydraulic conductivity of $K = 10^{-8} \text{ m s}^{-1}$ for the matrix, we observe a modeled pressure response that is too rapid for explaining the measured data (dashed, blue line in Figure 3.5). Overall, this DFN ensemble produced higher RMSE-values between measured and modeled data and is therefore characterized by a lower likelihood compared to the original matrix- K of 10^{-6} m s^{-1} . The complete inversion results for all source receiver combinations are shown in section A.3 (S1). It shall be noted that for both cases the misfit between measured and modeled data had remained almost constant for several thousands of iterations. It is thereby ensured that a stationary level had been reached and no better fit is possible, meaning that the shown DFN realization must be part of the posterior ensemble.

When neglecting the matrix completely (dotted, blue line in Figure 3.5), the modeled pressure response is even more rapid, and no satisfactory fit of the data can be achieved. The full result of this inversion case is shown in section A.3 (S2). As a consequence, a classical DFN inversion cannot be suitable for this data set. Instead,

the hybrid DFN inversion approach is necessary for processing the experimental data of this site, and probably also beneficial at other fractured-porous field sites.

3.4 Validation with thermal tracer test data

3.4.1 Field experiments

The thermal experiments used for the validation are conducted in opposite direction compared to the HT experiments (Fig. 3.1c) with heat injection in borehole M and observation of the resulting temperature response in borehole O. We evaluate the results for three different heat injections in the intervals M2, M3 and M4. The temperature of the injected water was approximately 20 °C, while the ambient temperature was around 9 °C during the experiments. The tests ran for 5 hours with an injection rate of 25 l min⁻¹. In the observation well, temperatures were recorded using a distributed temperature sensing (DTS) system with a vertical resolution of 0.5 m and an observation frequency of 1 min. During each thermal tracer test, double-packer systems were installed at different filter sections in the injection well attempting to reveal fractures at different filter sections. The results of these experiments have been published previously in Liu et al. (2022).

3.4.2 Simulation of the field experiments

The thermal tracer experiments were simulated in COMSOL 6.1 (Comsol, 1998) using the different inversion results obtained from the HT experiments as the underlying representation of the hydraulic properties. The computational domain is a 60 m × 60 m 2D rectangle with no-flow boundaries at the top and bottom and zero-pressure boundaries on the left and right, similar to the model used for the hybrid DFN inversion. We found that a larger horizontal distance between the boundary conditions and the boreholes (compared to the hybrid DFN inversion) is necessary due to the longer duration of the experiments.

The travel time inversion result was first converted from diffusivity D to permeability k (Eq. 3.2 and Eq. 3.8) by assuming a homogeneous specific storage of $5 \cdot 10^{-5} \text{ m}^{-1}$ (the same value was used for the matrix in the DFN inversion). The resulting k -distribution was imported as a pixel map, while the rest of the computational domain outside the inversion result was filled with a constant value of $k = 1.33 \cdot 10^{-13} \text{ m}^2$, which corresponds with the value of matrix permeability within

the hybrid DFN inversion ($K = 10^{-6} \text{ m s}^{-1}$) by using the conversion

$$k = \frac{\eta}{d \cdot g} \cdot K \approx 1.33 \cdot 10^{-7} \cdot K, \quad (3.8)$$

where η and d are dynamic viscosity and density of water, respectively, and g is the gravitational acceleration. To use the DFN result within the numerical model, several realizations of the posterior ensemble have to be implemented due to the stochastic nature of the inversion. Again, the sequence thinning method is employed to select every 100th realization of the last 900 iterations of the ensemble, meaning that the thermal tracer test simulations were conducted on 10 different DFN models. Each fracture was added manually to the numerical model as a line segment with the exact coordinates and permeability values from the inversion result. The permeability of the matrix was again assigned with $1.33 \cdot 10^{-13} \text{ m}^2$. Furthermore, porosity values of 0.3 for the matrix and 0.8 inside the fractures were assumed, as well as an average rock density of 2700 kg m^{-3} (Schön, 2015). The thermal conductivity ($0.58 \text{ W m}^{-1} \text{ K}^{-1}$ for the fluid and $3.0 \text{ W m}^{-1} \text{ K}^{-1}$ for the matrix), as well as the specific heat capacity ($4200 \text{ J kg}^{-1} \text{ K}^{-1}$ for the fluid and $1000 \text{ J kg}^{-1} \text{ K}^{-1}$ for the matrix) are based on literature values for sandstone (Schön, 2015).

Similar to the hydraulic forward models used within the inversion procedures, a 2D model is also employed for the thermal simulations. This approximation is typically reasonable in local zones with clearly defined principal stress directions (Lang et al., 2018), which is fulfilled in this specific field case due to the small distance between the boreholes (1.9 m) and the given orientation angles of the fractures.

For all the simulations, a homogeneous temperature field of $10 \text{ }^\circ\text{C}$ was used as initial condition and the temperature at the boundaries is kept at this value, accounting for the temperature of water inflow from the sides. In the injection interval, a mass flux of 25 l min^{-1} with a temperature of $20 \text{ }^\circ\text{C}$ was employed, in accordance with the actual field survey. The complete time span of the experiment (5 hours) was simulated. Fig. 3.6 illustrates the thermal tracer test simulation for one DFN realization for the injection interval M3 at three different time steps.

3.4.3 Comparison between measured and predicted thermal response

Fig. 3.7 compares the measured thermal response (left column of plots) produced by the three different injections in the intervals M2, M3, and M4 with the modeled thermal response using the continuum-based inversion result (middle column) and the hybrid DFN inversion result (right column). The results were evaluated in terms

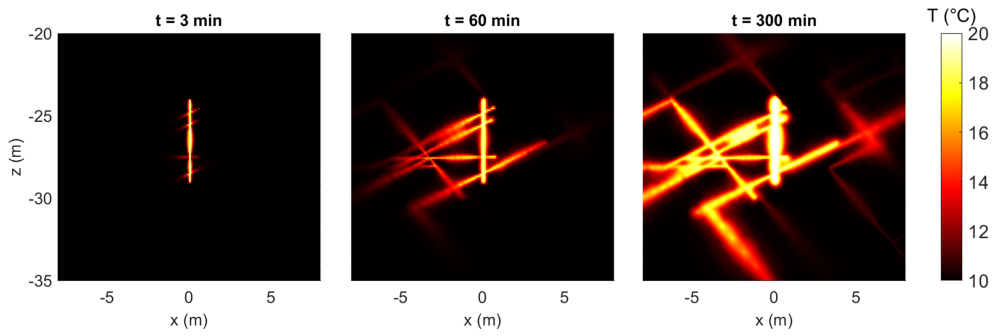


Figure 3.6: Snapshots of the thermal tracer test simulations performed in COMSOL for injection interval M3 at the first time step (left), after one hour (center) and at the last time step (right).

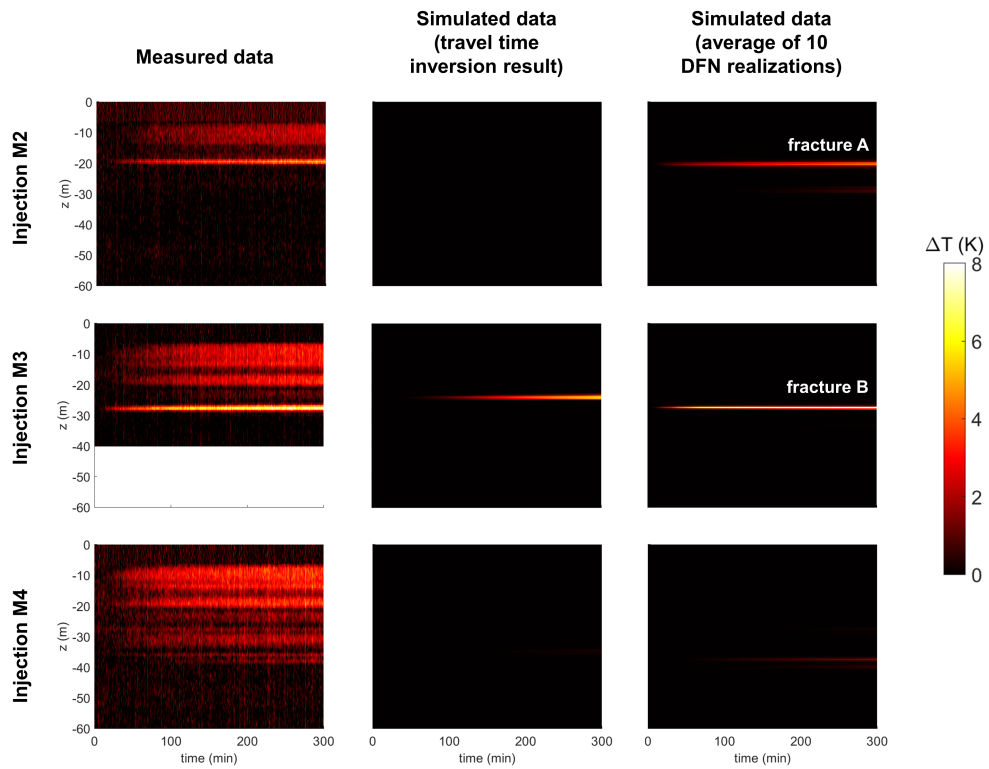


Figure 3.7: Comparison of measured data from the thermal tracer test (left column) and the simulated data using the travel time inversion result (center column) and the hybrid DFN inversion result (right column). Fracture A and fracture B are also shown in Fig. 3.3a.

of temperature deviation ΔT from the respective minimum values since the actual temperature of the aquifer was often slightly smaller (1-2 K) than the 10 °C assumed in the numerical model.

The measured data reveal two significant temperature anomalies: one for the first injection in interval M2 at a depth of -20 m with a temperature amplitude of up to 5 K, and another one for the second injection in interval M3 at a depth of -28 m with a temperature amplitude of up to 8 K. We interpret these major pathways for heat transport as the two prominent fractures A and B, which can also be identified in the hybrid DFN inversion result (Fig. 3.3a). The time-dependent behavior of the temperature breakthrough in those two fractures is also shown in Fig. 3.8 by the red lines. In these plots, the depth with the highest temperature amplitude was used for the evaluation, as this was assumed to be the crossing point of the fracture with the observation borehole.

The other temperature anomalies with much smaller amplitude, but wider vertical extensions (red areas in the plot) are most likely a result of vertical heat transport inside the observation borehole and/or remaining heat from the respective earlier injections (the experiments were conducted from top to bottom). Both of these effects are not accounted for in the numerical model, so that the anomalies cannot be observed in the simulated data.

The simulated temperature data using the continuum-based inversion result (middle column in Fig. 3.7) only reveal one significant temperature anomaly for injection M3 at a depth of -24 m. This corresponds with the high-diffusivity zone observed in the travel time inversion result shown in Fig. 3.2c. As described earlier, the exact depth of this zone cannot be expected to be reproduced by the travel time inversion. Therefore, this high-diffusivity zone can be assumed to resemble fracture B and so we show both thermal responses together in Fig. 3.8b. Compared to the measured data, the response from the travel time inversion result (orange line) is delayed and has a significantly smaller amplitude. We therefore conclude that, although the continuum-based approach actually reproduces this fracture, the estimation of its depth and permeability is not very accurate. At the approximate position of fracture A (Fig. 3.8a), only a very small temperature anomaly is simulated assuming a continuum (which would probably be below the noise level in a field experiment). In this case, the continuum model is not able to correctly predict the heat transport by this fracture.

The simulated temperature data using the hybrid DFN inversion result (right column in Fig. 3.7) is able to reproduce both fractures A and B. The calculated depths

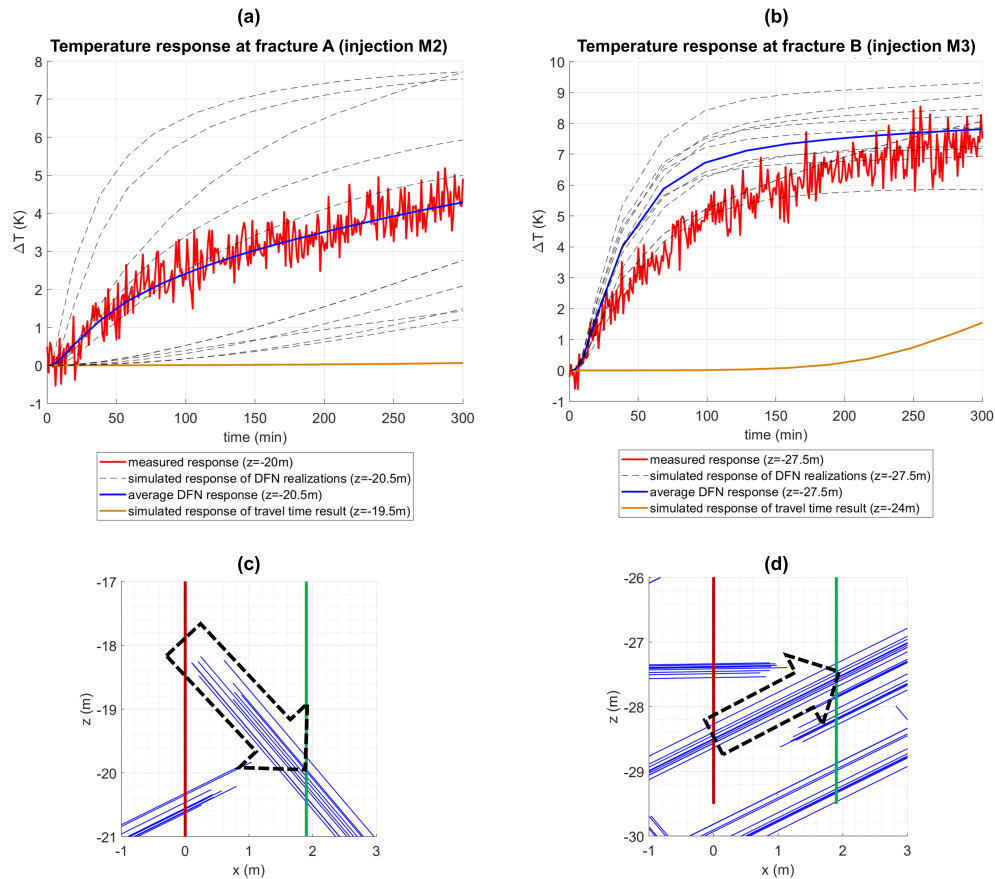


Figure 3.8: **(a)** Measured and **(b)** simulated temperature response curves for fractures A and B. The curves are always generated for the depth showing the greatest temperature amplitude, so that smaller inaccuracies regarding the location of the fractures in the inversion result are not considered in these plots. The plots **(c-d)** show the ten individual realizations of the posterior ensemble used for the numerical simulations (blue lines). Here, the black arrows indicate the general direction of heat transport from the injection to the observation borehole.

of the temperature anomalies are very accurate in comparison with the measured data. There is actually another weak anomaly caused by a fracture in the hybrid DFN result for injection interval M4 at a depth of -37 m. A similar anomaly is also visible in the measured data, but the signal is superimposed by noise and the borehole effects, which hampers reliable interpretation.

When looking at the time dependency as well as the amplitude of the temperature response (Fig. 3.8), it is crucial to distinguish between the individual realizations

(shown as black, dashed lines) and the average of those 10 realizations (blue, solid line). For fracture A, a strong variability among the individual realizations can be observed, with maximum temperature deviations ranging from 1 K to almost 8 K at the last time step. The reason is illustrated in Fig. 3.8c, where all ten DFN realizations are shown as blue lines. The major pathway of heat transport (black arrow) is maintained by a fracture that, although crossing the observation borehole (green line) directly, has no immediate contact to the injection borehole (red line). In the remaining gap, heat is only transported through the rock matrix, which is much slower compared to the heat transport in the fractures. Therefore, besides the exact parameter values assigned to the matrix in the model, the size of the remaining gap (=the distance of the heat transport through the matrix) has a huge impact on the temperature response observed in the other borehole. Since the position of this fracture is adapted and changes during the inversion process, the individual realizations produce strongly differing temperature responses. However, when computing the average of these realizations, the measured data can be predicted almost perfectly. This again highlights the importance of considering the stochastic nature of the hybrid DFN inversion results, as well as the need to model the flow in both discrete fractures and porous matrix within the hybrid DFN approach.

For fracture B, the individual realizations produce more similar temperature responses compared to fracture A, with maximum temperature deviations between 6 K and 9 K (Fig. 3.8b). In this case, the fracture directly connects the injection interval with the observation borehole (Fig. 3.8d), so that small variations in the position do not have a strong impact on the heat transport. However, changes in the permeability of the fracture may still affect the results. Again, the prediction of the measured data using the average of ten DFN realizations is fairly good, even if the rise in temperature is too rapid at early times. For both fractures, the prediction quality using the hybrid DFN inversion result is significantly better than using the continuum model.

3.5 Discussion

While the main focus of this study is the application of the novel hybrid DFN inversion approach to HT field data, we also want to give a detailed comparison with the continuum-based travel time inversion as well as provide guidance for future applications about how to select the more suitable inversion method under certain

conditions.

The main advantage of a continuum-based travel time inversion is the computational efficiency, with a total run time of 15-20 s on a standard laptop for the inversion performed on the HT data set of this study. It also requires less assumptions (and therefore minor a priori knowledge) about certain site conditions, since no boundary conditions have to be defined in the forward model and a lot of details about the experiment (pumping rate, pumping duration, borehole effects) are irrelevant. Despite all those simplifications, the inversion can yield good results for porous media with mostly continuous heterogeneities and allows to identify the major highly transmissive zones within the aquifer. Since the result of the inversion is deterministic, the interpretation of the tomogram is straightforward and does not require any stochastic evaluation.

However, only the diffusivity distribution can be retrieved by the travel time inversion. The conversion to hydraulic conductivity (or permeability) requires information about the specific storage, which can be approximated by a constant value derived from hydraulic attenuation inversion or by further post-processing (Hu et al., 2011; Jimenez et al., 2013). It is also important to note that regularization parameters (e.g., smoothness constraints) may strongly affect the results, and a trial-and-error strategy is often required to find reasonable values for those parameters. Furthermore, although the inversion itself is rather quick, the denoising procedures and picking of the exact travel time can be challenging and time-demanding. The strong simplifications made within the forward model also do not allow an evaluation of the uncertainties of the result.

For the data set of this study, only one out of two high-diffusivity zones (that were clearly visible in the thermal tracer test data) could be identified by the travel time inversion, and inaccuracies were observed in the predicted temperatures as well as in the location of the thermal breakthrough. It is an inherent limitation of the travel time inversion approach in combination with this specific field setup that the exact depth of these highly permeable zones cannot be inferred. Generally, the setup of this hydraulic tomography experiment with a small distance between the two boreholes (1.9 m), but a large vertical extension of the intervals (6 m) is not particularly favorable for performing a travel time inversion. Furthermore, the results indicate that flow between the boreholes is mainly established by narrow zones of high permeability, which might be regarded as fractures. Therefore, a continuum-based inversion approach is probably not suitable to accurately infer the hydraulic properties at this site.

Furthermore, a classical DFN inversion only considering individual fractures, but neglecting the influence of the matrix completely, could not fit the measured data with reasonable quality. Instead, the hybrid DFN inversion produced the best results by accounting for flow in both the matrix and the fractures. We could show that both of the highly transmissive zones could be identified by the hybrid DFN inversion, so that the thermal tracer test data were reproduced very accurately in terms of both location and amplitude of the temperature breakthrough. We therefore conclude that the hybrid DFN results are indeed suitable to be used for flow and transport modeling. Another advantage of the approach is that no preprocessing of the HT data is necessary. Noisy data can be used directly, and the underlying uncertainties are considered in the Bayesian inversion framework. The stochastic nature of the approach allows for the evaluation its uncertainties, e.g., in terms of a fracture probability map.

However, a DFN inversion is computationally expensive and may require a high-performance workstation. For the inversion performed for this study, we used a standard desktop PC with an 8-core i7-9700K 3.6 GHz processor and 32 GB RAM. With this setup, a total run time of 4-5 days was required to compute a probabilistic inversion result with a sufficiently large posterior ensemble. The forward model also requires the implementation of appropriate boundary conditions and some assumptions for fractures (e.g., orientation angles of fracture sets, as well as constant aperture and permeability for an individual fracture) are necessary. Therefore, a relatively large amount of a priori knowledge about certain site conditions is crucial to obtain accurate inversion results. It shall also be noted that, although matrix flow is contained in the hybrid DFN model, the matrix parameters are so far assumed constant and need to be predefined, and selecting reasonable values can be a crucial but challenging task. 3D and borehole effects are also neglected (or contained in matrix values) in the current study but could be included for other sites if necessary. Furthermore, due to the stochastic nature of the inversion, the results cannot be interpreted or used for flow and transport modeling directly, but require special post-processing.

We therefore suggest that the decision for one of the inversion approaches should be based on the actual site conditions as well as the expectations about the result. If the data were acquired in a fractured-porous environment with a big contrast in permeability between the rock matrix and individual fractures, the hybrid DFN approach is highly suggested. This was also shown by Fischer et al. (2020) for a karstic and fractured aquifer, where the inferred transmissivities of fracture and ma-

trix differ by several orders of magnitude. However, for an almost impermeable rock matrix (e.g., in most crystalline rocks), where hydraulic connections are exclusively maintained by the fractures, the classical DFN inversion (without matrix flow) can be sufficient (Ringel et al., 2021, 2022). If, on the other hand, the permeability contrast between matrix and fractures is very small, e.g., due to only partially open fractures or high fracture surface roughness, the heterogeneities can be assumed continuous, so that the travel time inversion is advantageous due to its simplicity and computational efficiency.

3.6 Conclusions and Outlook

We have shown that a hybrid DFN inversion approach, considering flow in both discrete fractures and a permeable matrix, is valuable for the hydraulic characterization of fractured-porous sites. The method was successfully applied to HT data acquired at a field site in Göttingen (Germany). For this specific field case, a good fitting of the experimental data could not be achieved by implementing a DFN inversion alone, but only by including a non-zero matrix permeability in the forward model. The results are in general agreement with a standard continuum-based travel time inversion, but the hybrid DFN approach can reveal some hydraulic connectivities in the aquifer with more detail and accuracy. This is also supported by independent validation data, i.e., a thermal tracer test conducted at the same site. Here, the inferred DFN ensemble is able to predict the thermal responses with high accuracy regarding the depth, the amplitude, and the time-dependent behavior of the temperature anomalies. However, it is crucial to take the stochastic nature of the approach into account to achieve good results.

The inversion approach might be used for a variety of applications, including the characterization of geothermal sites. For instance, according to a sensitivity study by Heldt et al. (2023), the thermal performance of a high-temperature aquifer thermal energy storage (HT-ATES) system is most sensitive to hydraulic conductivity and its vertical-to-horizontal anisotropy ratio. A preliminary characterization of the aquifer heterogeneity is thus necessary for a better system design and for improving the heat recovery during the operation phase. This characterization should include an accurate representation of both the fracture network and the porous rock matrix (Fischer et al., 2020).

However, this study should only be regarded as a first attempt for including matrix flow within a DFN inversion approach. For future applications of the hybrid

DFN inversion, a more generalized procedure can be desirable that has the ability to treat the matrix characteristics (K and S_s) as inversion parameters, and not pre-define them manually. Improvements could also be achieved by implementing spatially variable matrix parameters as well as including borehole effects directly in the forward model. An improved proposal distribution could be generated by considering complementary data (e.g., from geophysical methods) for the generation of DFNs. Furthermore, a proposal distribution could be implemented that considers the correlation between certain parameters, so that more proposed DFNs are likely to be accepted. This would ultimately result in higher computational efficiency. Further research topics include the application of the inversion approach in 3D, as well as the investigation of the resolution and reliability of the hybrid DFN inversion results for cases where only one borehole is available (geothermal applications). For this purpose, preliminary synthetic studies should be conducted to test and improve the methodology, but ultimately more field examples are needed to prove the robustness of the inversion approach.

Research Data

The experimental data used in this study (hydraulic tomography and thermal tracer test) can be found under the following link: <https://doi.org/10.5281/zenodo.10213883>

IV.

Joint inversion of induced polarization and hydraulic tomography data for hydraulic conductivity imaging

Lukas Römhild¹,
Gianluca Fiandaca²,
Peter Bayer¹

¹ Institute of Geosciences and Geography, Martin Luther University Halle-Wittenberg

² Department of Earth Sciences “Ardito Desio”, Università degli Studi di Milano

Geophysical Journal International 238(2) (2024) 960–973

<https://doi.org/10.1093/gji/ggae197>

Abstract

For accurate modelling of groundwater flow and transport processes within an aquifer, precise knowledge about hydraulic conductivity K and its small-scale heterogeneities is fundamental. Methods based on pumping tests, such as hydraulic tomography (HT), allow for retrieving reliable K -estimates, but are limited in their ability to image structural features with high resolution, since the data from time-consuming hydraulic tests are commonly sparse. In contrast, geophysical methods like induced polarization (IP) can potentially yield structural images of much higher resolution, but depend on empirical petrophysical laws that may introduce significant uncertainties to the K -estimation. Therefore, this paper presents a joint inversion procedure for both HT and IP data, which allows for combining the complementary abilities of both methods. Within this approach, a travel time inversion is applied to the HT data, while the IP inversion is based on a full-decay time-domain forward response, as well as a re-parametrization of the Cole-Cole model to invert for K directly. The joint inversion is tested on a synthetic model mimicking horizontally layered sediments, and the results are compared with the individual HT and IP inversions. It is shown that jointly inverting both data sets consistently improves the results by combining the complementary sensitivities of the two methods, and that the inversion is more robust against changes in the experimental setups. Furthermore, we illustrate how a joint inversion approach can correct biases within the petrophysical laws by including reliable K -information from hydraulic tests and still preserving the high-resolution structural information from IP. The different inversion results are compared based on the structural similarity index (SSIM), which underlines the robustness of the joint inversion compared to using the data individually. Hence, the combined application of HT and IP within field surveys and a subsequent joint inversion of both data sets may improve our understanding of hydraulically relevant subsurface structures, and thus the reliability of groundwater modelling results.

4.1 Introduction

The hydraulic properties of the near-surface Earth have long been a target of geophysical research (e.g., Binley et al., 2015). In particular, precise knowledge about the spatial distribution of the hydraulic conductivity K in shallow aquifers is crucial for predicting flow and transport processes correctly (e.g., Comunian et al., 2011; Refsgaard et al., 2012; You et al., 2020). Classically, in the hydrogeological community, this information is inferred from different types of hydraulic tests. Among them, hydraulic tomography (HT) has been established as a method that is able to image the spatial distribution of K between two or more boreholes using a tomographic configuration (Yeh & Liu, 2000). The method is based on sequential pumping experiments in several depth intervals within one borehole, while the transient pressure or hydraulic head response is recorded in other nearby intervals at different depths. A broad range of inversion approaches is available to infer the hydraulic parameters from the HT data, which are based either on discrete fracture network models (e.g., Klepikova et al., 2014, 2020; Somogyvári et al., 2019; Fischer et al., 2020; Ringel et al., 2022; Römhild et al., 2024a), or on heterogeneous continuum models (e.g., Illman et al., 2009; Berg & Illman, 2011; Cardiff et al., 2013, 2020; Fischer et al., 2017; Luo et al., 2023; Ren et al., 2021; Somogyvári & Bayer, 2017; Zha et al., 2015; Zhao et al., 2019, 2023), while the latter is most suitable for porous media. In particular, continuum-based travel time inversion (Brauchler et al., 2003, 2013b; Hu et al., 2011; Liu et al., 2022; Yang et al., 2020) is considered appealing due to its computational efficiency.

The main advantage of these methods is the direct link between the measured hydraulic data and the desired hydraulic parameters, which does not require using petrophysical approximations. Therefore, the overall quantification of K is highly reliable, reflecting the true hydraulic characteristics of the aquifer (e.g., Zhao et al., 2015). However, conducting these pumping tests in the field can be time-consuming and expensive, with a single test typically taking several hours (e.g., Berg & Illman, 2013), so that only a small number of them is practically feasible. Therefore, the ability to image the hydraulic parameters with high resolution is mostly limited due to a low data density and thus a high degree of non-uniqueness of the inverse problem (Bohling & Butler Jr., 2010). Furthermore, HT experiments are most sensitive to high- K zones as the major flow paths within the aquifer, but low- K heterogeneities are more difficult to image.

In contrast, hydrogeophysical measurements can often be conducted more time-

and cost-efficiently, making it more feasible to image subsurface heterogeneities with higher resolution. Particularly, induced polarization (IP) has the potential to reliably map the distribution of K in near-surface aquifers (Slater, 2007; Binley & Slater, 2020). Based on the conceptual similarities between groundwater flow and electrical conduction in porous media, petrophysical relations linking hydraulic and electrical parameters have been derived from laboratory experiments (e.g., Börner et al., 1996; Slater & Lesmes, 2002; Binley et al., 2005; Revil & Florsch, 2010; Titov et al., 2010; Revil et al., 2012b; Attwa & Günther, 2013; Weller et al., 2015; Robinson et al., 2018). The resulting equations can either be applied to the electrical parameters retrieved from the IP inversion in a separate step (Hördt et al., 2009; Attwa & Günther, 2013; Maurya et al., 2018a), or directly be incorporated into the inversion procedure (Fiandaca et al., 2018b; Römhild et al., 2022a). For the latter, a re-parametrization of the Cole-Cole model (Cole & Cole, 1941; Pelton et al., 1978; Tarasov & Titov, 2013) can be used as the model space (Fiandaca et al., 2018a). The main advantage of this approach is that K is an actual inversion parameter, and therefore the results can be interpreted in terms of hydraulic properties directly. Furthermore, regularization parameters can be defined with respect to K , and sensitivity calculations may be performed for this parameter. In addition, prior information given in terms of K can be used to inform the inversion directly (e.g., in the form of a starting model). It was also shown that the new model parameters are actually less correlated with each other than the classical Cole-Cole parameters (Fiandaca et al., 2021). The inversion approach has been tested by a synthetic study on a realistic aquifer analogue data set and compared with HT inversion results by Römhild et al. (2022a). Furthermore, the procedure has also been applied to field data, and the IP inversion results were in good agreement with K -estimates derived from borehole data, slug tests, and grain size analysis (Martin et al., 2021; Thalund-Hansen et al., 2023), thereby demonstrating that the IP- K inversion approach indeed has the potential to map spatial heterogeneities of the hydraulic properties.

However, the petrophysical relations used within this inversion (Weller et al., 2015; Revil et al., 2012b) are derived from laboratory experiments performed on a small set of samples, which is often not representative for the actual field case. Therefore, the accuracy of the K -estimates may be limited due to the inherent uncertainty of the petrophysical approximations. Furthermore, the accuracy of the K -quantification might be affected by the regularization parameters of the inversion. These limitations motivate the idea of incorporating reliable hydraulic data into the

IP inversion.

Based on the complementary abilities of HT and IP regarding sensitivity, spatial resolution, and reliability of the K -estimates, the aim of this work is to combine the IP- K inversion approach with a HT travel time inversion in order to image the distribution of K with high accuracy. In an earlier attempt, the IP results have been calibrated by using hydraulic data providing reliable estimates for an effective hydraulic conductivity K_{eff} (Römhild et al., 2022a). However, these calibration techniques are often not straightforward and require a certain amount of manual fitting. Therefore, the objective of this paper is to introduce a joint inversion procedure, in which HT and IP data can be inverted simultaneously for a distribution of K that minimizes both data misfits. Generally, petrophysical joint inversion approaches have already been used in other contexts, such as permafrost sites (Mollaret et al., 2020), gas hydrate systems (Turco et al., 2021) or reservoir characterization (Gao et al., 2012). The inversion strategy presented in this paper aims to combine the high-resolution structural information from IP with the robust K -estimates derived from HT, as well as the complementary sensitivities of both methods to areas of enhanced or reduced K . We implement the joint inversion procedure for a simple synthetic test case to show the main benefits as well as the limitations of the method. In particular, biased petrophysical relations are introduced to assess the robustness of the joint inversion against these uncertainties, compared to individual inversion. The quality of the inversion results is evaluated by using the structural similarity index (SSIM).

The paper is structured as follows. We introduce the two individual inversion strategies for IP and HT as well as the joint inversion approach in section 4.2. Subsequently, the individual and joint inversion results based on a synthetic model are presented in section 4.3, with special emphasis on the ability of the joint inversion to correct a petrophysical bias within the IP-based K -estimates. We discuss our findings in section 4.4, thereby focusing on the applicability to actual field cases. Some concluding remarks as well as an outlook to further research questions are given in the last section.

4.2 Methods

4.2.1 Induced polarization

Petrophysical foundation

The concept of inverting IP data for hydraulic conductivity K is based on the fact that electrical and hydraulic rock parameters are typically governed by the same pore space properties (Slater, 2007). In general, the electrical conductivity σ^* of a porous medium can be considered as a frequency-dependent and complex-valued quantity (Vinegar & Waxman, 1984):

$$\sigma^*(\omega) = \sigma_{\text{el}} + \sigma_{\text{int}}^*(\omega), \quad (4.1)$$

which is a superposition of electrolytic conductivity σ_{el} and interface conductivity σ_{int}^* , with $\omega = 2\pi f$ being the angular frequency, and the * denoting complex quantities. It may either be given in terms of real and imaginary part (σ' and σ'' , respectively) or as magnitude $|\sigma^*|$ and phase angle ϕ :

$$\sigma^*(\omega) = \sigma'(\omega) + i\sigma''(\omega) = |\sigma^*| \cdot e^{i\phi}, \quad (4.2)$$

with i denoting the imaginary unit. The electrolytic part describes the DC conduction through a rock's pore space, and therefore depends on pore volume properties as described by Archie's law (Archie, 1942) assuming fully saturated conditions:

$$\sigma_{\text{el}} = \frac{\sigma_w}{F} = \Phi^m \cdot \sigma_w, \quad (4.3)$$

where σ_w is the pore water conductivity, $F = \Phi^{-m}$ is the formation factor, Φ is porosity, and m is the empirical cementation exponent.

In contrast, the interface conductivity σ_{int}^* can be governed by a variety of different electrical polarization phenomena mainly attributed to the interface between pore space and rock matrix. In the absence of electronically conductive minerals, such as graphite or pyrite, diffusion-related polarization connected to the electrical double layer (EDL) at the pore-matrix-interface is dominant (Marshall & Madden, 1959; Schwarz, 1962; Olhoeft, 1985; Bückner & Hördt, 2013). Since these polarization effects strongly depend on the frequency of the applied current, the spectral behavior of σ^* must be taken into account, which is commonly described by the Cole-Cole

model (Cole & Cole, 1941; Pelton et al., 1978; Tarasov & Titov, 2013):

$$\sigma^*(\omega) = \sigma_0 \left[1 + \frac{m_0}{1 - m_0} \left(1 - \frac{1}{1 + (i\omega\tau_\sigma)^c} \right) \right]. \quad (4.4)$$

Here, σ_0 is the DC conductivity, m_0 the intrinsic chargeability as defined by Seigel (1959), τ_σ the relaxation time, and c the frequency exponent.

In order to achieve the re-parametrization of the Cole-Cole model in terms of hydraulic properties, two different petrophysical approaches are applied within this work. First, Weller et al. (2015) found a relation to estimate the permeability k that is based on the formation factor F as a measure for the volumetric properties of the pore space, and the imaginary part of the electrical conductivity σ'' evaluated at 1 Hz accounting for the polarization strength:

$$k = \frac{1.08 \cdot 10^{-13}}{F^{1.12} (\sigma''(1 \text{ Hz}))^{2.27}} \quad (4.5)$$

for unconsolidated and fully saturated sediments. Within this approach, the relationship

$$\sigma''(1 \text{ Hz}) = 0.042 \cdot \sigma'_{\text{int}}(1 \text{ Hz}) \quad (4.6)$$

between imaginary and real part of surface conductivity found by Weller et al. (2013) is also used. However, in this work, the relation is imposed at the frequency $f = (2\pi\tau_\sigma)^{-1}$ according to Fiandaca et al. (2018b).

As a second approach, we use an equation suggested by Revil et al. (2012b) using the formation factor F , the diffusion coefficient of the Stern layer D_+ , and the relaxation time τ_σ :

$$k = \frac{\tau_\sigma D_+}{4F}. \quad (4.7)$$

The relation is based on the concept of τ_σ being a measure for typical scale lengths in the rock's pore space, which in return govern hydraulic conductivity. We use the two distinct D_+ -values for sand and clay:

$$\begin{aligned} D_{+, \text{sand}} &= 1.3 \cdot 10^{-9} \cdot \text{m}^2 \text{s}^{-1}, \\ D_{+, \text{clay}} &= 3.8 \cdot 10^{-12} \cdot \text{m}^2 \text{s}^{-1}, \end{aligned} \quad (4.8)$$

given by Revil et al. (2015), in order to simulate realistic τ_σ -values within the forward modelling. However, the physical significance of D_+ remains ambiguous (Weller et al., 2016), and therefore this parameter might introduce a high degree of

uncertainty to this relation (Eq. 4.7). For a more detailed discussion on the inherent limitations of the petrophysical relations, we also refer to Fiandaca et al. (2018b) and Römhild et al. (2022a).

In order to include different petrophysical approaches within our inversion procedure, both Equations (4.5) and (4.7) are used simultaneously, forcing the inversion to produce K -values that fulfil the two relations equally well. This is based on the hypothesis that a combined approach has the potential to make the K -estimation more robust against varying field conditions that may differ from the underlying assumptions of the individual petrophysical relations.

Finally, the conversion from permeability k to hydraulic conductivity K is performed using the relation

$$K = \frac{d \cdot g}{\eta} \cdot k \approx 7.5 \cdot 10^6 \cdot k, \quad (4.9)$$

where d is the density of the pore fluid, g the gravitational acceleration, and η the dynamic viscosity of the pore fluid. The approximation is achieved by assuming a groundwater temperature of 10 °C.

IP forward modelling

Generally, IP experiments can be conducted either in the frequency domain (spectral induced polarization, SIP) or in the time domain (TDIP). Both approaches can potentially produce consistent results of similar quality (Martin et al., 2020). In this work, we focus on TDIP, since it is more widely used within field applications due to a typically smaller acquisition time (Maurya et al., 2018b). By performing full-decay spectral inversion (Fiandaca et al., 2012, 2013; Madsen et al., 2020), an accurate retrieval of spectral properties can be achieved, given that a wide time range is used during data acquisition (Madsen et al., 2017), for instance through the analysis of full-waveform recordings (Olsson et al., 2016). The general concept of time-domain IP experiments is illustrated in Figure 4.1. For more details about the method we refer to Binley & Slater (2020).

The forward response is computed using the WhyCDF model space, similar to Römhild et al. (2022a). We assume a constant water conductivity of $\sigma_w = 50 \text{ mS m}^{-1}$ as well as a homogeneous formation factor of $F = 5$ as realistic values for unconsolidated sediments (Schön, 2015). The K -distribution is set up according to the synthetic test case given in subsequent section 4.2.4, and the diffusion coefficient D_+ is derived from K by interpolation in log-space from the sand-clay values sug-

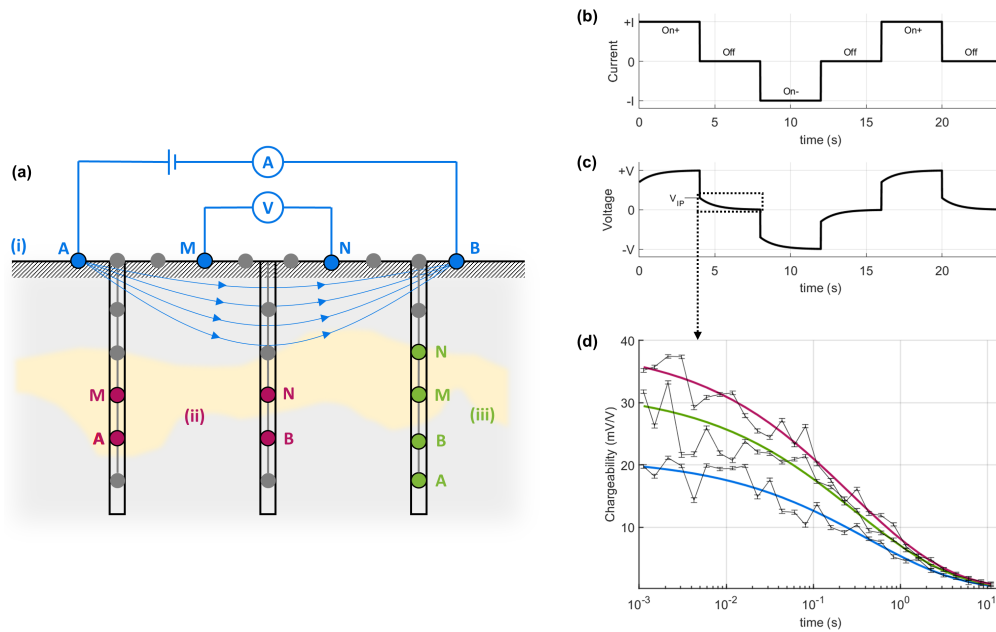


Figure 4.1: **(a)** Generalized setup of (i) surface (blue), (ii) cross-borehole (red), and (iii) single-borehole (green) IP experiments with current electrodes A and B, and voltage electrodes M and N. **(b)** Current signal with alternating on-times and off-times, and **(c)** observed voltage including charging curves and decay curves caused by the polarization effects. **(d)** Exemplary voltage decay curves with added Gaussian noise (black lines with error bars), and the respective curves fitted by the inversion (coloured lines).

gested by Revil et al. (2015) (Eq. 4.8). Although a continuous relationship between K and D_+ has not yet been proven by other studies, we consider it a reasonable approximation for imposing realistic τ_σ -values on the data. The frequency exponent $c = 0.5$ is assumed homogeneous. Clearly, these can be strong assumptions, especially regarding a constant formation factor. However, it was shown in previous works that an accurate K -distribution is also achieved when including spatial variability in F (Römhild et al., 2022a). Nevertheless, the synthetic experiments can only be regarded as best-case scenarios that illustrate the general potential of the method.

The specific setup of the IP experiments is given in section 4.2.4. The forward simulation is executed using EEMverter, an inversion tool for electric and electromagnetic data (Fiandaca et al., 2023). The 2D solution of the forward problem is computed in the frequency domain, and then transformed to the time domain

through a Hankel transform taking into account both the current waveform and the receiver transfer function, following Fiandaca et al. (2013).

Finally, Gaussian noise of 2 and 10 per cent magnitude is added to resistivity and IP data, respectively. As illustrated in Figure 4.1d, this can be regarded as a relatively high noise level, which accounts for the difficulty to acquire high-quality IP data under certain field conditions. However, we find that decay curves with such noise content can still be fitted by the inversion, so that the approach can be expected to be applicable to field data.

4.2.2 Hydraulic tomography

Full modelling

The HT experiments are simulated by using the finite element solver of pyGIMLi, a Python-based open-source library for multimethod modelling and inversion in geophysics (Rücker et al., 2017). The geometries of the test cases and the corresponding mesh are generated by the sub-module “meshtools”, and the K -information of the synthetic model (see section 4.2.4) is assigned to the different layers.

Flow in the porous medium, modelled as a continuum, is governed by Darcy’s law and the continuity equation. Therefore, the governing equation of the simulation is the following partial differential equation (PDE):

$$S_s \frac{\partial h}{\partial t} - \nabla \cdot (K \nabla h) = 0, \quad (4.10)$$

which can also be written as

$$S_s \frac{\partial h}{\partial t} - \nabla K \cdot \nabla h - K \nabla^2 h = 0. \quad (4.11)$$

In both formulations, S_s is the specific storage, K is the hydraulic conductivity, and h is the hydraulic head. Equation 4.10 can be implemented using the function “solveFiniteElements” of pyGIMLi, which solves PDEs matching the form

$$c \frac{\partial u}{\partial t} = \nabla \cdot (a \nabla u) + bu + f(\mathbf{r}, t), \quad (4.12)$$

by setting $u = h$, $a = K$, $b = 0$, $c = S_s$, and $f = 0$. The hydraulic head on the sides of the domain is kept at zero by applying a Dirichlet boundary condition. The injection is implemented as a Neumann boundary condition applied to the respective injection intervals. Examples of the full solution of the PDE (Eq. 4.10) are shown

in Figure 4.2b, where the pressure response curves (hydraulic head over time, in response to a Heaviside pumping signal) are plotted for different combinations of source receiver pairs. This full modelling approach is applied for computing the synthetic HT data used in this work. However, only the peak times of the head responses (the times at which the first derivatives of the pressure signals reach their maximum) are used as data in the inversion process, as explained in the subsequent section. The specific setup for the experiments shown in this work is given in section 4.2.4.

Travel time approximation

For computing the forward response within the inversion of HT data, we use the travel time approximation of Eq. 4.11, which neglects the $(\nabla K \cdot \nabla h)$ term in comparison to $S_s \frac{\partial h}{\partial t}$, such that the peak time (or the time for reaching a fraction α of the peak) can be computed as the line integral between the source point S_i (where the pumping-induced pressure is generated) and the receiver point R_i (where the resulting hydraulic head is observed), following the ray path ε :

$$\sqrt{t_{\alpha,h}} = \frac{1}{\sqrt{6f_{\alpha,h}}} \int_{S_i}^{R_i} \frac{d\varepsilon}{\sqrt{\frac{S_s(\varepsilon)}{K(\varepsilon)}}}, \quad (4.13)$$

where $t_{\alpha,h}$ is the time for reaching the fraction α of the peak, and $f_{\alpha,h}$ is a scaling factor that is computed numerically from the diffusion equation of homogeneous media (Brauchler et al., 2003). The subscript h indicates that a Heaviside signal was used for the pumping tests. In this work, we apply a 25 per cent early time diagnostics approach (i.e., $\alpha = 0.25$) according to Brauchler et al. (2003). By using earlier travel times, the sensitivity of the inversion to preferential flow paths can be enhanced (Hu, 2011). Similar to seismic travel time inversion (Zelt & Smith, 1992), Eq. 4.13 can be solved by using ray tracing techniques. For this purpose, the “travelttime” submodule of pyGIMLi is utilized for computing the forward response based on Dijkstra’s algorithm (Dijkstra, 1959). A noise level of 3 per cent was added to the travel time data, based on Doetsch et al. (2010) and Hu et al. (2017).

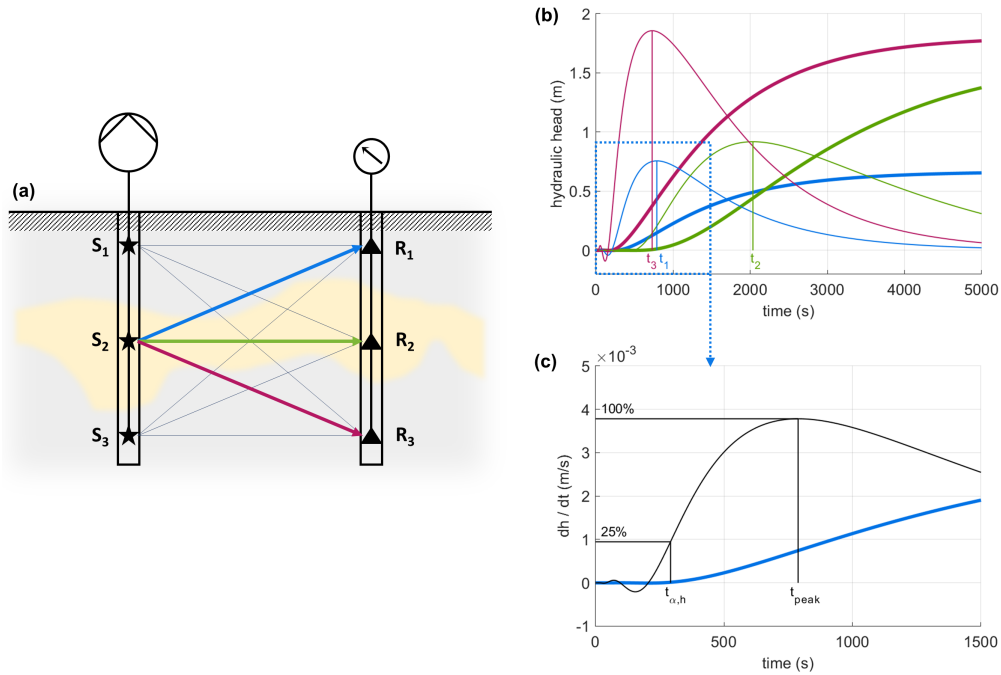


Figure 4.2: **(a)** Generalized setup of a HT experiment with simplified ray paths between source points S_i and receiver points R_i . **(b)** Travel time processing of HT data. The bold lines represent the hydraulic head response at the receiver points initiated by a Heaviside signal at the pumping locations. The thin lines are the respective first derivatives, and the peak times t_i are picked at the maximum of these curves. The color-coding refers to the ray paths in (a). **(c)** Early-time diagnostics for travel time processing. The bold, blue line is the hydraulic head response of the first ray path, while the thin, black line shows its first derivative. The early time $t_{\alpha,h}$ is picked where the derivative reaches 25% of its maximum value. Note that numerical instabilities commonly occur in the early phase of the pumping experiment simulation.

4.2.3 Inversion

IP-K inversion

The data space of the IP inversion comprises both the DC data and the complete IP decays for the respective quadrupole sequence. The inversion of these data is performed in the ThyCD model space similar to Römhild et al. (2022a). Consequently, the inversion parameters comprise the total (DC) conductivity σ_0 , the hydraulic conductivity K , the diffusion coefficient D_+ , and the frequency exponent c . When evaluating the inversion results, D_+ might also be interpreted in

terms of an apparent diffusion coefficient D_a as described by Weller et al. (2016). The inverse problem is solved within the EEMverter framework through an iterative Gauss-Newton scheme based on Fiandaca et al. (2013, 2023), where the objective function contains the squared data misfit and smoothness regularization terms for vertical and horizontal constraints. The constraints allow for adjusting the spatial variability of each model parameter in horizontal and vertical direction. However, all four model parameters remain uncoupled and space-dependent within the inversion.

HT inversion

The data space of the HT inversion comprises the early times $t_{\alpha,h}$ of the source receiver pairs of the simulated sequence (described in section 4.2.4), while the model space is defined by the 2D distribution of K (assuming homogeneous S_s). Although the inversion could be fully performed in the pyGIMLi environment together with the forward computations, EEMverter is used in this study for carrying out the HT inversions (as well as the joint inversions), thanks to the feature of EEMverter of accepting external forward and jacobian computations. Additional codes for establishing the interface between EEMverter and pyGIMLi are implemented in MATLAB, and the transfer of the data is handled by text-based files. In particular, the model of the current iteration (i.e., the K -distribution) is exported by EEMverter and then used by pyGIMLi for the forward calculation. The resulting HT data (i.e., the travel times) as well as the Jacobian matrix for this model are subsequently transferred back to EEMverter, which handles the actual inversion procedure.

Joint inversion

The joint inversion of both data types is also implemented using the EEMverter framework, with internal computation of DC and IP data and external forward calculation of the HT response using pyGIMLi. Generally, the results can be achieved by either a classical, fully-joint inversion (minimizing both data misfits simultaneously), or by working with different inversion cycles. In the latter case, the inversion might be performed for one data type only in a first cycle, and the joint inversion of both data sets is executed in a second cycle using the result of the first cycle as a starting model. In this paper, only results from the fully-joint, single-cycle inversion are shown to ensure comparability. The use of the same inversion algorithm for all the inversion types in this study (IP- K inversion, HT traveltime inversion, and joint inversion) allows for a fair and easy comparison of inversion results, because regu-

larization, damping, data weighting, and stopping criteria are treated in the same way for all data types.

Since the number of IP data points is typically larger than the available HT data points, considerations about the correct weighting of the different methods within the joint inversion are necessary. In the current form of the algorithm, data are weighted according to their given standard deviation. For the synthetic data used in this work, we have carefully chosen reasonable standard deviation models that ensure a well-balanced influence of the two methods within the joint inversion. However, for the inversion of field data, where the standard deviation is an inherent part of the data that cannot be modified, the implementation of an explicit weighting factor might become necessary.

4.2.4 Synthetic model

To illustrate the advantages as well as the limitations of the joint inversion approach, a simple synthetic model mimicking horizontally layered sediments with alternating hydraulic conductivity is constructed (Figure 4.3a). The model domain has a horizontal extension of 12 m and extends down to 8 m depth. It primarily consists of material with an intermediate hydraulic conductivity of $K = 10^{-6} \text{ m s}^{-1}$, intermitted by a layer of 1 m thickness with high hydraulic conductivity ($K = 10^{-4} \text{ m s}^{-1}$) at 2 m depth, another layer of the same thickness with low hydraulic conductivity ($K = 10^{-8} \text{ m s}^{-1}$) at 4 m depth, and a thinner layer (0.5 m) of high hydraulic conductivity ($K = 10^{-4} \text{ m s}^{-1}$) at 6 m depth. In this way, the different sensitivities of the two methods for areas of enhanced K (HT) or reduced K (IP) shall be illustrated. In addition, the ability of the different experimental setups to resolve small-scale structural features, such as thin horizontal layers, shall be assessed.

While the hydraulic conductivity is the shared parameter used within the synthetic experiments of both HT and IP, the model also comprises additional parameters that are individually required for one of the methods. The underlying assumptions for those parameters are described in the respective sections about the synthetic experiments (sections 4.2.2 and 4.2.1), while the values used in the simulations are shown in Figure 4.3, including the diffusion coefficient D_+ (Figure 4.3b). To illustrate the effect of the heterogeneity in K and D_+ on the IP response, additional electrical parameters are shown in Figure 4.3c–f. Note that those are not defined as model parameters but can be derived from the other parameters by using the petrophysical conversions given in section 4.2.1. Consequently, smaller values for K lead to a stronger polarization (manifested as higher phase peak ϕ_{\max} and higher

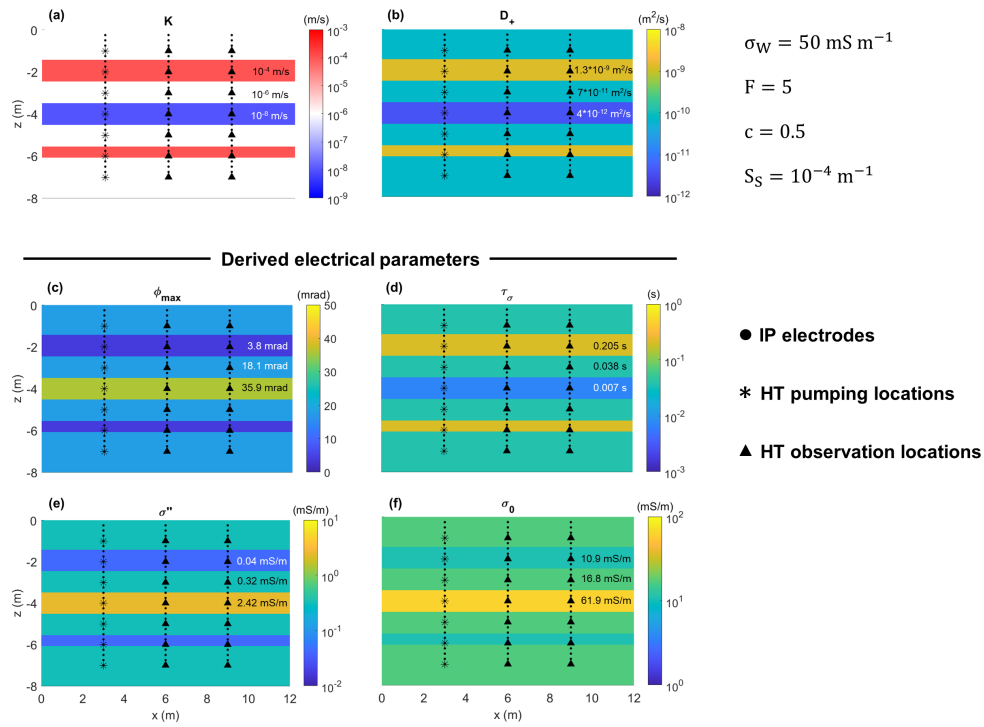


Figure 4.3: Distribution of hydraulic conductivity K (a) and diffusion coefficient D_+ (b) in the synthetic model. The parameters given on the right are assumed constant for the synthetic experiments. The given parameter set can be used to compute other electrical parameters by the conversions given in section 4.2.1. Here, we show the maximum phase angle ϕ_{\max} (c), the Cole-Cole relaxation time τ_σ (d), the imaginary part of electrical conductivity σ'' evaluated at $f = (2\pi\tau_\sigma)^{-1}$ (e), and the DC conductivity σ_0 (f). Three boreholes are placed at $x = 3 \text{ m}$, 6 m , and 9 m , with IP electrodes (black dots) distributed with 25 cm spacing, and HT source points (asterisks) and receiver points (triangles) with at least 1 m spacing.

σ''), shorter relaxation times τ_σ , and a higher DC conductivity σ_0 .

In all cases, it is assumed that three boreholes are located in the model domain with a horizontal distance of 3 m and a vertical extension down to 7 m depth. The electrodes for the IP experiments as well as pumping and observation locations of the HT setup are placed in those boreholes.

For the HT experiments, the injection intervals are located in the left borehole at $x = 3 \text{ m}$. We use an interval length of 0.1 m and an injection rate of 0.5 m s^{-1} to simulate pumping tests, which are conducted sequentially from top to bottom. The

observation points are located in two other boreholes at $x = 6$ m and $x = 9$ m at the same depths as the injection intervals, and the hydraulic head is recorded over time at the nearest node of the mesh.

The setup of the IP data acquisition is based on a common cross-borehole scheme with electrodes being distributed with 25 cm spacing in the three hypothetical boreholes at $x = 3$ m, 6 m, and 9 m. Note that for this study no surface electrodes are used to allow a fair comparison with the HT experiments. The sequence is built using a combination of cross-borehole and single-borehole quadrupoles (cases (ii) and (iii) in Figure 4.1a, similar to Römhild et al. (2022a)), consisting of 1860 quadrupoles in total. Each decay curve is defined by 41 IP time gates ranging from 0.003 s to 12 s (Figure 4.1c).

4.3 Inversion results

4.3.1 Individual HT and IP inversion results

The K -images resulting from the different test cases are shown in Figure 4.4 in comparison with the synthetic model (a). In the IP result (Figure 4.4b), the different layers of the model are reproduced by the inversion and the overall K -quantification is accurate. A high spatial resolution can be achieved due to the small electrode spacing of 25 cm. However, regularization-induced smoothing effects lead to a tendency of underestimating K in the high-permeability zones and overestimating K in the less permeable areas. The limited ability to correctly reproduce sharp boundaries and strong parameter contrasts is a common characteristic of inversion procedures using smoothness constraints (Loke et al., 2003). In particular, the thin layer of high K at 6 m depth is strongly underestimated, which is also a result of the reduced sensitivity of IP to high- K zones due to the weakness of the polarization effects. However, such thin layers of enhanced K often serve as major flow paths within an aquifer and are therefore important to capture.

For the HT inversion, we show three different inversion results for different experimental setups: (i) with 1 m spacing between the pumping locations as well as between the receiver points (Figure 4.4c, data set with 98 travel times), (ii) with 2 m spacing, and points being placed inside the layers (Figure 4.4d, data set with 18 travel times), and (iii) with 2 m spacing, and points being placed outside the layers (all points in areas of $K = 10^{-6} \text{ m s}^{-1}$, Figure 4.4e, data set with 32 travel times). In the first case, the two layers of high K are clearly visible in the results, since they serve as preferential flow paths during the HT experiments. The low- K

layer has also been reproduced by the inversion due to acting as a hydraulic barrier between some of the source receiver pairs. Generally, although the K -quantification in terms of average values is accurate, the spatial resolution of the result is much lower compared to IP due to the larger spacing between the source and receiver locations. For the hydraulic experiments, a spacing smaller than 1 m is hardly feasible in practice. Instead, even this setup can be very time-consuming and expensive, and an experiment with even less source and receiver points might be favourable. In this case, when increasing the spacing to 2 m, the individual layer boundaries are not well-resolved, and the K -information from the zones of high sensitivity (i.e., the ray paths, which are predominantly inside the layers) migrates to the areas of low sensitivity due to the smoothness constraints. Therefore, large areas of high K and low K are visible in the inversion result, instead of the thin layers from the input model. In the third case (Figure 4.4e), where the source and receiver points are placed outside the layers, the inversion result is more dominated by the intermediate K -estimates, and the contrast in K is less pronounced. Furthermore, layer boundaries in the inversion result are shifted towards the modified source and receiver locations, which highlights the strong influence of the sensitivity distribution of the individual experimental setup on the inversion results. Generally, an HT setup with 2 m spacing is not sufficient to resolve the small-scale structural elements of the synthetic model.

4.3.2 Joint inversion results

The results of the joint inversion are shown in the right section of Figure 4.4 (f–h). Clearly, the complementary sensitivities of both methods are combined, so that both high- K and low- K layers can be identified in the results, and their delineation with respect to the areas with intermediate K is more accurate. Furthermore, the high spatial resolution of IP that allows resolving thin layers of contrasting K is complemented by the strong sensitivity of HT to the preferential flow paths, so that the thin layer of high K at -6 m depth is more pronounced than in the individual IP results. Generally, the quantitative estimates of K are very accurate (with stronger contrasts compared to the individual IP inversion) and the joint inversion is more successful in attributing the K -information to the correct location due to being less constraint- and more data-driven. Note that in this case the same smoothness constraints are applied for all inversions to ensure comparability, although it can be beneficial to use different constraints depending on the different methods and setups. In addition, the joint inversion results for the different HT setups are actually

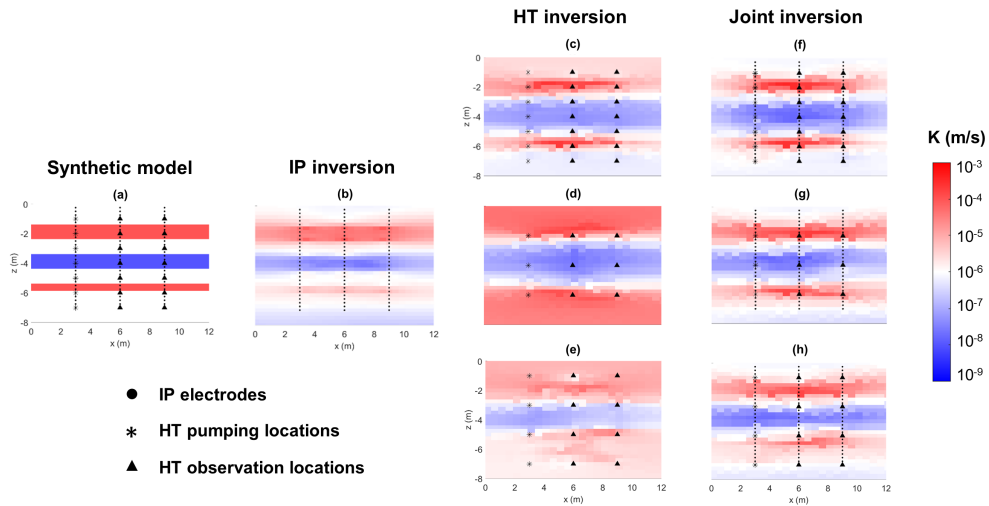


Figure 4.4: Individual inversion results for IP (b) and HT (c–e), as well as joint inversion results (f–h) in comparison with the original synthetic model (a). In the result plots, only the electrodes / source and receiver points that are contained in the respective data set used for the inversion are shown. The color bar for K applies to all plots.

very similar, indicating that the joint inversion is more robust against changes in the experimental setup. Even a small amount of pumping tests can be sufficient to extract the relevant information that improve the reproduction of the K -distribution.

4.3.3 Influence of petrophysical bias

To assess the potential of the joint inversion to correct a bias in the petrophysical relations used within the IP inversion, we now include such bias directly in the forward modelling of the IP data. This is achieved by multiplying the K -values of the synthetic model with a constant factor (10^{-2} , 10^{-1} , 10^1 , or 10^2). Therefore, we can only account for a constant shift within the petrophysical relations, but not for inherent scatter. All other direct input parameters (including D_+) remain untouched within this modified example. However, note that the electrical properties do change as a result of this modification, similar to the illustrations in Figure 4.3c–f.

The resulting K -images of the IP inversion are shown in Figure 4.5 in the uppermost row of plots. Here, the centre plot depicts the unbiased results as shown in Figure 4.4b, the left plots include a negative bias, and the right plots a positive bias of one or two orders of magnitude. As expected, the changes are clearly reflected in the individual IP inversion results, with K being underestimated for the

negative bias, and overestimated for the positive bias. In addition, the reproduction of structural features is generally less successful for a stronger petrophysical bias.

Subsequently, the joint inversion is performed for all possible combinations of IP bias and HT setup. The individual HT results are shown again in the left-hand column of Figure 4.5 – these plots, as well as the joint inversion results without petrophysical bias, are the same as in Figure 4.4 (c–e and f–h, respectively). For the first two HT setups (1 m, and 2 m inside), the joint inversion is able to reproduce all layers of the synthetic model, with fairly good K -estimates and strong contrasts between the different structural elements. These structures have not been captured by neither the HT inversion nor the biased IP inversion in such detail, but by combining the sensitivities of both methods, a large improvement in the quality of the inversion results is achieved. While HT has the ability to capture the major flow paths (red layers in the plot) and ensures the reliability of the K -quantification, the IP data still contain valuable information about small-scale structural features, even if they are not visible in the individual IP results when assuming a petrophysical bias. For these two cases, the joint inversion results are also robust against changes in the setup of the HT experiments, indicating that reducing the amount of pumping tests is not necessarily problematic. However, when shifting the HT source and receiver location to areas between the layers (last row of plots), the joint inversion results are significantly less accurate. Here, the hydraulic information provided by the HT experiments is not sufficient to correct the petrophysical bias with the same reliability compared to the first two setups. This indicates that not only the spacing between HT source and receiver points, but also their exact location with respect to the relevant structural features is crucial for achieving good joint inversion results. Although the second HT setup contains only three pumping tests, the results are significantly better than the third HT setup with four pumping tests. However, compared to the individual IP and HT results, all joint inversion bring improvement to the reproduction of the structural features.

4.3.4 Comparison of structural similarity

To allow for a more quantitative comparison of the methods, the structural similarity index (SSIM) of the inversion results compared to the synthetic model is calculated. Being rooted in image processing, the SSIM measures the similarity between two images by considering luminance, contrast, and structural information (Wang et al., 2004), and is bounded from 0 to 1, while the latter value indicates perfect similarity between two images. The index has already been used as a tool for assessing the

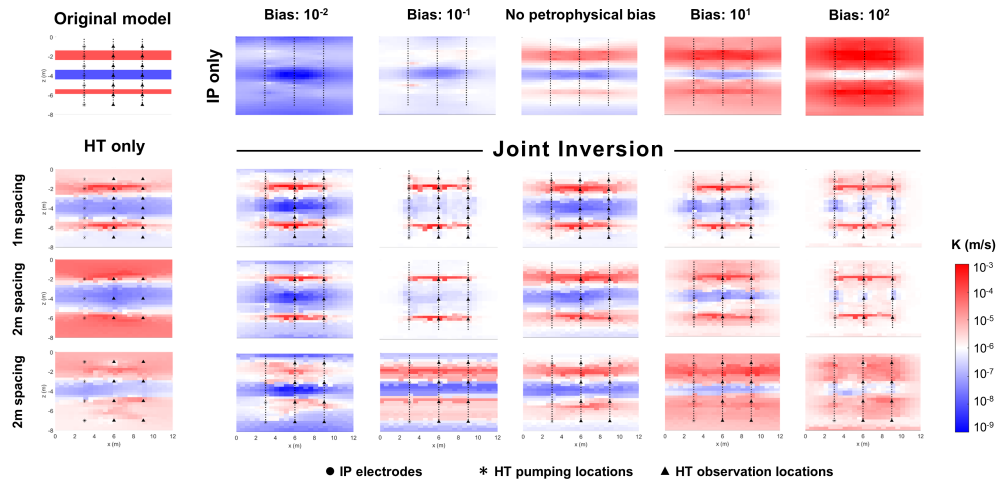


Figure 4.5: Inversion results for the individual HT inversion (left column), the individual IP inversion including petrophysical bias factors (uppermost row), and joint inversion results for all possible combinations. The colour bar for K applies to all plots.

quality of geophysical inversion results (e.g., Giraud et al., 2018; Almadani et al., 2021; Römhild et al., 2022a), or for quantifying the prediction quality of machine learning approaches (Thibaut et al., 2021). In our work, the Python package “scikit-image” (van der Walt et al., 2014) is utilized for calculating the SSIM, and only the part of the domain between the boreholes is used for the computation, since the sensitivity of HT is restricted to this area.

The results are shown in Figure 4.6 with respect to the petrophysical bias applied to the IP data. For the individual IP inversion (black curve with triangular markers), the SSIM is approximately 0.46 for the unbiased case, and decreases significantly for the negative bias of one order of magnitude (0.14), and two orders of magnitude (0.01). As shown above, the structural features of the model can hardly be reproduced when assuming a negative petrophysical bias (Figure 4.5). In contrast, a positive bias of one order of magnitude actually produces the highest SSIM (0.58). Apparently, due to the limited sensitivity of IP to high- K areas, the inversion result is improved when the K -prediction is shifted by a certain factor. As shown in Figure 4.5, the contrast between the different layers is more pronounced for the 10^1 -bias compared to the unbiased result, and the K -prediction in the highly permeable layers is more accurate. This is also in accordance with some findings by Römhild et al. (2022a), where calibrating the IP results with a constant K_{eff} derived

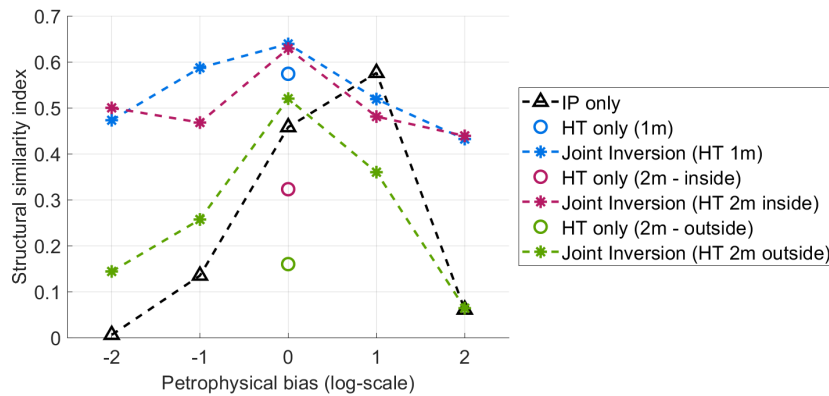


Figure 4.6: Structural similarity index (SSIM) of the inversion results, compared to the original synthetic model, for the different inversion methods, and with varying petrophysical bias. The dashed lines are for visual guidance only.

from hydraulic tests (“factor calibration”) was found to be a helpful approach for improving the results of transport simulations. However, when increasing the bias even further to two orders of magnitude, the quality of the results is significantly reduced, characterized by an SSIM of 0.06. Generally, the individual IP results show a strong dependency on a potential bias of the petrophysical relations, which is not only influenced by the amplitude, but also the direction of the bias.

The SSIM of the individual HT results is visualized by circle markers, with the colours indicating the different setups. While the setup with 1 m spacing (blue) produces an SSIM of 0.57, which is slightly higher than the individual IP inversion, a setup with larger spacing (2 m) results in a poorer reproduction of the structural features and K -estimates, with an SSIM of 0.32 for source and receiver points inside the layers (red), and an SSIM of 0.16 for points outside the layers (green). This is in accordance with the visual inspection of Figures 4.4 and 4.5. The quality of the individual HT inversion results strongly depends on the specific setup of the hydraulic experiments, and a sufficiently small spacing of source and receiver points (i.e., a large number of time-consuming pumping tests) has to be used to achieve results that have a similar quality compared to IP.

The SSIM of the joint inversion results is shown by asterisk markers, and the colours indicate the setup of the used HT data. When using the unbiased IP data within the joint inversion, significantly higher SSIM values can be achieved compared to the individual HT inversion, for all three HT setups (compare pairs of circle and

asterisk markers of the same colours in the plot). Compared to the unbiased IP result, the SSIM values of the joint inversion are also slightly higher for all three HT setups, indicating an improved inversion result even when only sparse hydraulic data are used to complement the IP data.

When including the biased IP data in the joint inversion, most of the resulting SSIM values are still higher than the respective individual HT values (or at least in a similar range). It shows that complementing hydraulic tests by IP experiments can even be beneficial when the underlying petrophysical assumptions are not entirely fulfilled at the specific field site. In any case, the high-resolution structural information from the IP data is valuable, and it is worth including them in the joint inversion procedure, even if the exact quantification of K by the IP experiments is not correct.

When comparing the joint inversion results with the individual IP results, significantly higher SSIM values can be observed in nearly all cases. The only exception for this specific model is the 10^1 -bias, where the individual IP inversion had produced an exceptionally high SSIM value, as explained above. Here, the SSIM values of the joint inversion are slightly smaller, but still indicate a high quality of the inversion results.

The joint inversion results using the first two HT setups (blue and red markers in Figure 4.6) are particularly robust against the petrophysical bias of the IP data. Here, the SSIM values of the biased joint inversion results are almost as high as for the unbiased joint inversion result (roughly between 0.4 and 0.6). This indicates that by using the reliable K -estimates from the hydraulic tests, the bias of IP resulting from the uncertainty of the petrophysical relations can indeed be corrected. However, a suitable HT setup is crucial for achieving such significant improvements. When using the last HT setup (2 m spacing, points outside the layers) for the joint inversion (green markers in Figure 4.6), the improvement compared to the individual inversion results is rather modest. If the HT source and receiver positions are placed outside the relevant structural features, the hydraulic information is less valuable for the joint inversion procedure. Therefore, the exact location of the source and receiver points can in some cases be more important than simply the amount of pumping tests.

4.4 Discussion

The main objective of the presented methodology is the correction of potential petrophysical uncertainties within the IP- K inversion, as presented in the previous section. Those uncertainties may arise, for instance, from the empirical parameters in the approach of Weller et al. (2015), or from the limited applicability of the diffusion coefficient D_+ in the relation of Revil et al. (2012b). The latter may also be interpreted as an apparent diffusion coefficient D_a in the inversion results (Weller et al., 2016), but its physical significance in the context of IP inversion remains ambiguous. In addition, petrophysical relations are also resolution-dependent, and may not hold on different scales (Hermans & Irving, 2017; Singha et al., 2015). They are mostly derived from a relatively small set of samples in the laboratory, which is often not representative for the actual field conditions (e.g., Benoit et al., 2019).

To overcome these problems, the idea of jointly evaluating electrical and hydraulic data has already been proposed by Slater (2007). We have now shown that a joint inversion of HT and IP data is a promising approach for implementing this concept. Including the reliable K -estimates from the hydraulic data can potentially correct a petrophysical bias within the IP inversion, thereby overcoming some of the aforementioned uncertainties.

The presented inversion approach relies on a single-component Cole-Cole model, which can be seen both as an oversimplification or as an unnecessary complexity, depending on the point of view. The rationale of this choice is that a frequency-dependent model is necessary for taking into account Eq. 4.7 in the K -estimation, and that the Cole-Cole model is widely used for fitting IP spectra of data acquired in the field and consequently for parametrizing the model space of IP inversions. However, some sediments may not show a single-component polarization peak, but are instead characterized by several polarization components at different frequencies (Weigand & Kemna, 2016; Römhild et al., 2022b): in these cases, a more complex description of the electrical properties and of the link between electrical and hydraulic properties might be used, for instance in terms of Debye decomposition (Nordsiek & Weller, 2008; Zisser et al., 2010; Hase et al., 2022). On the contrary, when a constant-phase behaviour (Börner et al., 1996; Weller et al., 1996; Lajaunie et al., 2016) is sufficient for describing the electrical properties of the sediments, the proposed approach should still work, since the Cole-Cole model for very small values of the frequency exponent c becomes a constant phase angle model.

For the latter case, a much simpler method of inferring K from IP data has been proposed by Flores Orozco et al. (2022). It is based on computing σ'' from the integral chargeability, and then relying on the petrophysical relations of Weller et al. (2015) for computing K . However, this approach does not consider the actual spectral characteristics of the data, and variations in spectral content as well as non-standard decay types (e.g., heterodox transients as described by Fiandaca et al. (2022)) might lead to bias in the inversions. Instead, a full decay inversion can potentially cover these transient types, and is therefore favourable for inverting cross-borehole IP data.

Another critical point for every geophysical joint inversion is the dimensionality of the problem depending on the acquisition schemes of the different methods (JafarGandomi & Binley, 2013; Ghalenoei et al., 2022). For a successful joint inversion of all data types, consistent acquisition geometries are crucial. In our test case, the data acquisition points of both HT and IP are placed in the same boreholes, so that the two data sets cover the same 2D cross-section. Such setups should also be most feasible within field applications. However, the experiments cannot be carried out simultaneously, so it needs to be ensured that temporal changes in the subsurface between the measurements, for instance due to seasonal variations, are negligible.

Furthermore, field measurements could also contain IP data collected on a surface profile. If such profile covers the same cross-section as the boreholes, so that the overall inversion problem is restricted to a 2D section, the current version of the presented algorithm is still applicable. Although surface IP experiments have a limited ability of resolving small-scale structures in greater depths, the HT data might still cover this depth range, and a joint inversion of both data types would benefit from the complementary sensitivities. If no borehole electrodes are installed, simultaneously carrying out both experiments might be practically possible, but the hydraulic stimulation during the HT experiments could strongly affect the resulting IP signal (e.g., due to streaming-induced self-potential). Therefore, a sequential measuring procedure is still advisable.

Challenges for the joint inversion of HT and IP data might arise from strongly differing geometries, especially if the combined data set is not restricted to a 2D cross section but covers a 3D domain. Currently, the inversion algorithm presented here is not available for 3D applications, but it will be extended in the future (similar to Madsen et al. (2020)). However, sufficient overlap in the sensitivity coverage would be crucial to ensure that the hydraulic data can potentially correct biased IP-based K -estimates within the joint inversion. For this purpose, pre-experimental synthetic

studies investigating the exact sensitivity distributions would be indispensable to optimize the acquisition geometry. Additionally, the computational cost to invert for a 3D distribution of the model parameters increases drastically, so that high-performance workstations are required. Similar issues would arise from including anisotropy in the model, which is necessary in some geological settings.

4.5 Conclusions

In a new attempt of combining geophysical and hydrological approaches for imaging hydraulic conductivity K , IP and HT data were processed together within a fully-joint inversion. Thereby, the complementary abilities of both methods regarding sensitivity, spatial resolution and reliability of the K -estimates were combined. We tested the new joint inversion strategy on a simple synthetic test case to illustrate the benefits and limitations of the method. It could be shown that the joint inversion brought significant improvements when comparing the results to the individual IP and HT inversion, especially when hydraulic information is sparse. In addition, the robustness against uncertainties in the petrophysical relations underlying the IP inversion was significantly increased when using the joint inversion approach. By including the HT data, a possible petrophysical bias was successfully corrected by the reliable K -estimates from the hydraulic tests, while the high-resolution structural information from IP is also preserved. Compared to the calibration approaches proposed by Römhild et al. (2022a), the joint inversion has the ability of handling the complementary information from the two data sets automatically, is therefore more elegant, and does not require any manual tuning.

However, the present study shall only be regarded as a starting point showing the general potential of the joint inversion approach. In future works, the methodology can be tested on more complex synthetic models, like aquifer analogue data sets similar to Heinz et al. (2003) or Bayer et al. (2015), also assessing the influence of other experimental setups, as well as, potentially, more complex bias in the petrophysical relations of IP. Furthermore, expanding the approach to data sets with different dimensions might be an important step towards fully capturing the hydraulically relevant structures in the subsurface.

Clearly, the application of the joint inversion approach to field data will be crucial to test the actual applicability of the method in practice. For that purpose, a well-known field site should be chosen to enable the comparison with already available stratigraphical and hydraulic information, and ideally with other geophysical data.

The applicability of the petrophysical relations needs to be ensured by choosing a site with unconsolidated, fully saturated sediments characterized by significant heterogeneities in the hydraulic parameters. Pre-experimental synthetic studies might be conducted to determine the most suitable setup for imaging the relevant structures. Ultimately, the inversion results could be validated by performing tracer experiments as proposed by Römhild et al. (2022a).

Generally, we would like to encourage the combined application of geophysical and hydrological methods in the context of imaging the hydraulic parameters of the near-surface Earth. By applying a joint inversion procedure as proposed in this work, the benefits of two complementary methods can be combined, thereby yielding results with much higher resolution and accuracy. In particular, an improved understanding of the small-scale subsurface heterogeneities in the hydraulic parameters can be essential to achieve more reliable predictions from flow and transport models, which strongly depend on the underlying K -information. Therefore, a joint inversion of IP and HT data can be an important contribution towards the goal of understanding and modelling flow and transport processes in aquifers more correctly.

Research Data

The synthetic model and data, as well as all inversion results shown in this work are available through: Römhild, L., Fiandaca, G., & Bayer, P. (2024). Induced polarization and hydraulic tomography joint inversion results on a synthetic model [Data set]. Zenodo. <https://doi.org/10.5281/zenodo.10208903>.

V.

Synopsis

5.1 Summary and conclusions

Three different hypotheses were formulated as the main objectives of this thesis in Chapter 1. In the following, it will be evaluated whether their verification has been successful, and which conclusions can be drawn from the results.

Hypothesis 1:

Time-domain induced polarization data can be inverted directly for a hydraulic conductivity subsurface model.

A novel inversion procedure for TDIP data has been developed in Chapter 2 (Römhild et al., 2022a). Within this approach, petrophysical relations between hydraulic and IP parameters are incorporated into the inversion, allowing for direct computation of the spatial distribution of K . The method was successfully tested on the Bolstern aquifer analog data set by performing synthetic IP experiments using a combined cross-borehole and surface electrode acquisition geometry. By inverting those data, the structural features of the aquifer were successfully reconstructed with high resolution and accuracy. Therefore, it could be shown that TDIP data can be used to infer the spatial distribution of K within an aquifer without applying any additional processing.

However, the reliability of such IP-derived K -estimates strongly depends on the accuracy and applicability of the petrophysical relations within the geological setting present at the field site. This issue was tackled by introducing two different calibration strategies that use hydraulic information from sparse pumping tests, and can therefore improve the quantitative estimates of K . The quality of all results was assessed by performing synthetic tracer experiments, which underlined the importance of such calibration techniques. Although the proposed methodology yielded accurate results for this test case, it still requires some manual fitting procedures for making the K -estimation reliable. Hence, there was still a demand for a more straightforward procedure of combining hydraulic and geophysical data. This demand was eventually fulfilled by the joint inversion introduced in Chapter 4 (see Hypothesis 3).

Hypothesis 2:

A combination of continuum- and fracture-based modeling approaches yields more accurate and reliable inversion results using hydraulic tomography data.

A new hybrid DFN inversion procedure for HT data has been developed in Chapter 3 (Römhild et al., 2024a). It is based on a classical DFN inversion that allows resolving individual fractures but is extended by considering a nonzero matrix permeability. This approach was applied to an HT data set acquired at a fractured-porous field site in Göttingen (Germany). Results proved that by also considering flow through a porous matrix, a better data fit can be achieved compared to a classical DFN approach. For validation, the subsurface models were used to predict heat tracer tests, which had also been conducted at the site. The modeled temperature response based on the hybrid DFN result compared well with experimental data in terms of amplitude, location, and time-dependent behavior of the temperature anomaly. In particular, the results are superior to a purely continuum-based approach that does not allow for resolving individual fractures.

Hence, it was shown that combining continuum- and fracture-based modeling techniques is important for achieving more accurate subsurface representations based on HT data. Especially at fractured-porous sites, considering groundwater flow through both the matrix and individual fractures in the forward model of the inversion is crucial. Neglecting one of the components can lead to misinterpretation of the data. For the hybrid DFN approach implemented within this thesis, the stochastic nature of the results has to be considered, e.g., by evaluating several realizations of the DFN ensemble in a statistical manner. Stochastic inversion approaches are generally computationally expensive and require more complicated processing procedures. However, it was revealed that such tools with a high degree of sophistication are often required to achieve an accurate and reliable characterization of aquifer heterogeneities.

Hypothesis 3:

A joint inversion of induced polarization and hydraulic tomography data improves the spatial resolution, accuracy, and reliability of the hydraulic conductivity estimation by combining the complementary abilities of both methods.

A new joint inversion procedure for IP and HT data has been developed in Chapter 4 (Römhild et al., 2024b). It is based on the IP- K inversion introduced in Chapter 2, as well as a travel time inversion for the HT data. Therefore, both individual inversion techniques are continuum-based and deterministic, which allows using the same inversion framework, in this case EEMverter. The approach was successfully tested on a synthetic model inspired by horizontally layered sediments of contrasting hydraulic (and hence electrical) parameters. The joint inversion allows to increase the spatial resolution, accuracy, and reliability of the K -estimates compared to individual IP or HT inversion. In particular, it was shown how potential bias in the petrophysical relations within the IP inversion is corrected automatically when including the reliable hydraulic information from HT. Vice versa, the IP data can provide the required structural information with high resolution, which cannot be achieved by sparse HT data sets alone. This illustrates how the complementary abilities of both methods are combined by the joint inversion.

Although a joint application of geophysical and hydraulic methods for aquifer characterization tasks has been promoted frequently in the last decades, the actual implementation of simultaneous data processing approaches has remained a challenging task. The joint inversion procedure proposed in this work can be a helpful tool for handling such different data types in a straightforward manner. However, an application to different types of field cases will surely be crucial to evaluate the performance in practice and additional challenges must be expected when dealing with actual field data (see section 5.2). Different geological environments and acquisition parameters may require modifications within the data processing and inversion methodology. Ultimately, the joint inversion approach, when used correctly within the restriction given by its underlying assumptions, may be an important step towards a more accurate characterization of aquifer heterogeneities, thus building the foundation for an increased reliability of groundwater modeling results.

5.2 Outlook

With the inversion procedures introduced in this work, several new components are added to the toolbox of hydrogeophysical data processing and inversion techniques, allowing for a more accurate characterization of aquifer heterogeneities. This includes approaches for both fractured and porous rocks, as well as for both hydraulic and geophysical data. The combined application of these two types of methods is promoted throughout this thesis, ultimately resulting in the joint inversion procedure for HT and IP data, which was introduced in Chapter 4.

While the hybrid DNF inversion (Chapter 3) was applied to field data, the other inversion techniques were only tested on synthetic examples in this work. Consequently, the next step must be the application of these approaches within field studies. The IP- K inversion introduced in Chapter 2 was used to estimate hydraulic parameters at a waste site for assessing contaminant mass discharge, and the results from IP compared well with data from slug tests and grain size analysis (Thalund-Hansen et al., 2023). The accurate prediction of contaminant transport at a specific site will probably be an important field of application for the proposed methods in the future, because detailed information about K -heterogeneities in a relatively small domain is crucial for such tasks. More field investigations making use of the IP- K inversion method in similar contexts are currently under way.

For testing the joint inversion of HT and IP data in practice for the first time, specific and controlled field settings are required to allow for a validation of the inversion results. To ensure the applicability of the petrophysical relations within the IP inversion, a site with unconsolidated sediments and a shallow groundwater table (fully saturated conditions) is recommended. Ideally, such a site would have already been investigated extensively. Stratigraphical information, as well as other geophysical and hydraulic data from previous experiments, could then be used in the planning phase, and subsequently for a comparison of the results. Furthermore, a sufficient contrast in K -heterogeneities should be present at the site. For instance, an alternation of sand and clay would allow for assessing the ability of the methods to image small-scale structures within the aquifer. Concerning the experimental setup, at least two boreholes will be required with a suitable distance, ideally between two and five meters, and a well diameter that can handle both HT and IP equipment. This setup might be extended by IP surface profiles, and by more boreholes in the same 2D cross-section similar to the synthetic example in Chapter 4. For a validation of the inversion results, tracer tests could be conducted similar to the suggestions

given in section 2.3.2.

In parallel to planning and conducting such field experiments, more methodological developments can be considered in the future. Within the IP inversion, a parameterization of the model space in terms of a Debye decomposition may be beneficial compared to the Cole-Cole based approach, as recently proposed by Günther & Martin (2024). This approach would still allow for handling time-domain full-waveform IP data but not rely on the assumption of a purely Cole-Cole-like behavior of the conductivity spectra. Instead, the Debye parameterization is often regarded as the most generalized and natural model space for IP data, allowing for a superposition of several Debye relaxations with different time constants τ_n and chargeabilities m_n (Nordsiek & Weller, 2008). The petrophysical IP- K relations may then be used by deriving a total chargeability and a log-mean relaxation time from the Debye spectra (Martin et al., 2024). Using such parameterization may widen the range of geological settings, in which the inversion strategy could potentially be used. However, a careful comparison of the two inversion strategies on synthetic as well as field data has to be a target of future research.

For the HT inversion, the travel time approach is based on the assumption of a homogeneous specific storage S_s . To include a spatial variability of this parameter, hydraulic attenuation inversion could be incorporated into the framework (Brauchler et al., 2011). Furthermore, the HT forward response may also be based on a full groundwater model within the joint inversion scheme, instead of using the travel time approximation. This forward problem can also be solved using pyGIMLi, as it was implemented for the full modeling of HT data (section 4.2.2). However, this would result in more degrees of freedom and therefore potentially increased non-uniqueness of the solution, as well as higher computational effort.

Similar issues might arise when modifying the hybrid DFN inversion procedure by including spatially variable matrix characteristics for K and S_s as part of the model space. However, the need for pre-defining of these parameters before the inversion would be eliminated, making the method more widely applicable at fracture-porous sites. Using a DFN-based approach for the HT data within the joint inversion is not considered meaningful since the petrophysical IP- K relations are only valid in unconsolidated sediments, and not in fractured rock. Therefore, both HT and IP inversion approaches have to be based on continuum models in such a joint inversion framework.

Furthermore, including even more methods in the inversion scheme may help to increase the sensitivity in other areas within the domain of interest, resolve more

structural features, and potentially enhance the reliability of the K -estimates. In particular, including electromagnetic (EM) methods seems very promising since they are often able to reach deeper regions of the aquifer. Also, they allow for airborne surveys and can therefore cover large areas faster. Including EM data within a joint inversion scheme could be implemented using the newest developments of EEMverter (Fiandaca et al., 2024) and EEMstudio (Sullivan et al., 2024), which will also have the capability of performing 3D inversions. An auspicious example is the joint inversion of transient EM and IP data recently presented by Signora et al. (2024), which yielded significant improvements in uncovering subsurface heterogeneities in electrical conductivity compared to individual inversions. However, using the IP effect contained in EM data to invert for hydraulic parameters will remain a great challenge (Marchant. et al., 2014; Sharifi et al., 2024).

In contrast to a deterministic approach, the joint inversion could also be performed within a Bayesian framework, similar to the DFN inversion of Chapter 3. This would allow for better uncertainty estimation and a more detailed analysis of the individual roles of the methods for the K -quantification, as shown, e.g., by Blatter et al. (2019). Ultimately, the rapid development of artificial intelligence tools will also help with the processing and inversion of the data and potentially give new opportunities for retrieving the required hydraulic information from different types of field experiments (Yu & Ma, 2021; Sun et al., 2022).

In the long run, these improvements in data processing and inversion techniques providing highly informative subsurface representations can be the foundation for more accurate groundwater modeling results, and will therefore contribute to enhanced reliability in the monitoring and managing of aquifers as an important precondition for widely available groundwater resources.

Bibliography

- Adler, P. M. & Thovert, J.-F., 1999. *Fractures and Fracture Networks*, Kluwer Academic Publishers.
- Adler, P. M., Thovert, J.-F., & Mourzenko, V. V., 2013. *Fractured Porous Media*, Oxford University Press.
- Ahmed, A. S., Jardani, A., Revil, A., & Dupont, J. P., 2016. Specific storage and hydraulic conductivity tomography through the joint inversion of hydraulic heads and self-potential data, *Advances in Water Resources*, 89, 80–90.
- Almadani, M., Waheed, U. b., Masood, M., & Chen, Y., 2021. Dictionary learning with convolutional structure for seismic data denoising and interpolation, *Geophysics*, 86(5), 1S0–Z1.
- Amanambu, A. C., Obarein, O. A., Mossa, J., Li, L., Ayeni, S. S., Balogun, O., Oyebamiji, A., & Ochege, F. U., 2020. Groundwater system and climate change: Present status and future considerations, *Journal of Hydrology*, 589, 125163.
- Archie, G. E., 1942. The electrical resistivity log as an aid in determining some reservoir characteristics, *Transactions of the American Institute of Mining, Metallurgical and Petroleum Engineers*, 146, 54–62.
- Atekwana, E. A. & Slater, L. D., 2009. Biogeophysics: A new frontier in earth science research, *Reviews of Geophysics*, 47, RG4004.
- Attard, G., Bayer, P., Rossier, Y., Blum, P., & Eisenlohr, L., 2020. A novel concept for managing thermal interference between geothermal systems in cities, *Renewable Energy*, 145, 914–924.
- Attwa, M. & Günther, T., 2013. Spectral induced polarization measurements for predicting the hydraulic conductivity in sandy aquifers, *Hydrology and Earth System Science*, 17, 4079–4094.

- Baetzel, K., 2017. *Hydrogeological Characterization of a Fractured Aquifer based on Modelling and Heat Tracer Experiments*, Master's thesis, University of Göttingen.
- Bagnardi, M. & Hooper, A., 2018. Inversion of surface deformation data for rapid estimates of source parameters and uncertainties: A bayesian approach, *Geochemistry, Geophysics, Geosystems*, 19(7), 2194–2211.
- Barbieri, M., Barberio, M. D., Banzato, F., Billi, A., Boschetti, T., Franchini, S., Gori, F., & Petitta, M., 2023. Climate change and its effect on groundwater quality, *Environmental Geochemistry and Health*, 45, 1133–1144.
- Bauer, J. F., Krumbholz, M., Meier, S., & Tanner, D. C., 2017. Predictability of properties of a fractured geothermal reservoir: the opportunities and limitations of an outcrop analogue study, *Geothermal Energy*, 5(1), 24.
- Bayer, P., Comunian, A., Höyng, D., & Mariethoz, G., 2015. High resolution multi-facies realizations of sedimentary reservoir and aquifer analogs, *Scientific Data*, 2, 150033.
- Bayes, T., 1763. An essay towards solving a problem in the doctrine of chances, *Philosophical Transactions of the Royal Society of London*, 53, 370–418.
- Benning, M. & Burger, M., 2018. Modern regularization methods for inverse problems, *Acta Numerica*, 27, 1–111.
- Benoit, S., Ghysels, G., Gommers, K., Hermans, T., Nguyen, F., & Huysmans, M., 2019. Characterization of spatially variable riverbed hydraulic conductivity using electrical resistivity tomography and induced polarization, *Hydrogeology Journal*, 27, 396–407.
- Berg, S. J. & Illman, W. A., 2011. Three-dimensional transient hydraulic tomography in a highly heterogeneous glaciofluvial aquifer-aquitard system, *Water Resources Research*, 47(10), W10507.
- Berg, S. J. & Illman, W. A., 2013. Field study of subsurface heterogeneity with steady-state hydraulic tomography, *Groundwater*, 51(1), 29–40.
- Berkowitz, B., 2002. Characterizing flow and transport in fractured geological media: A review, *Advances in Water Resources*, 25, 861–884.

- Berre, I., Doster, F., & Keilegavlen, E., 2019. Flow in fractured porous media: A review of conceptual models and discretization approaches, *Transport in Porous Media*, 130, 215–236.
- Bing, Z. & Greenhalgh, S. A., 2000. Cross-hole resistivity tomography using different electrode configurations, *Geophysical Prospecting*, 48, 887–912.
- Binley, A. & Slater, L. D., 2020. *Resistivity and Induced Polarization - Theory and Applications to the Near-Surface Earth*, Cambridge University Press.
- Binley, A., Slater, L. D., Fukes, M., & Cassiani, G., 2005. Relationship between spectral induced polarization and hydraulic properties of saturated and unsaturated sandstone, *Water Resources Research*, 41, W12417.
- Binley, A., Hubbard, S. S., Huisman, J. A., Revil, A., Robinson, D. A., Singha, K., & Slater, L., 2015. The emergence of hydrogeophysics for improved understanding of subsurface processes over multiple scales, *Water Resources Research*, 51, 3837–3866.
- Binley, A., Keery, J., Slater, L., Barrash, W., & Cardiff, M., 2016. The hydrogeological information in cross-borehole complex conductivity data from an unconsolidated conglomeratic sedimentary aquifer, *Geophysics*, 91, E409–E421.
- Blatter, D., Key, K., Ray, A., Gustafson, C., & Evans, R., 2019. Bayesian joint inversion of controlled source electromagnetic and magnetotelluric data to image freshwater aquifer offshore new jersey, *Geophysical Journal International*, 218(3), 1822–1837.
- Boersma, Q. D., Bruna, P. O., de Hoop, S., Vinci, F., Moradi Tehrani, A., & Bertotti, G., 2021. The impact of natural fractures on heat extraction from tight triassic sandstones in the west netherlands basin: a case study combining well, seismic and numerical data, *Netherlands Journal of Geosciences*, 100, E6.
- Bohling, G. C. & Butler Jr., J. J., 2010. Inherent limitations of hydraulic tomography, *groundwater*, 48(6), 809–824.
- Bohling, G. C., Butler Jr., J. J., Zhan, X., & Knoll, M. D., 2007. A field assessment of the value of steady shape hydraulic tomography for characterization of aquifer heterogeneities, *Water Resources Research*, 43, W05430.

- Bording, T. S., Fiandaca, G., Maurya, P. K., Auken, E., Christiansen, A. V., Tuxen, N., Klint, K. E. S., & Larsen, T. H., 2019. Cross-borehole tomography with full-decay spectral time-domain induced polarization for mapping of potential contaminant flow-paths, *Journal of Contaminant Hydrology*, 226, 103523.
- Brauchler, R., Liedl, R., & Dietrich, P., 2003. A travel time based hydraulic tomographic approach, *Water Resources Research*, 39(12), 1370.
- Brauchler, R., Cheng, J. T., Dietrich, P., Everett, M., Johnson, B., Liedl, R., & Sauter, M., 2007. An inversion strategy for hydraulic tomography: Coupling travel time and amplitude inversion, *Journal of Hydrology*, 345, 184–198.
- Brauchler, R., Hu, R., Dietrich, P., & Sauter, M., 2011. A field assessment of high-resolution aquifer characterization based on hydraulic travel time and hydraulic attenuation tomography, *Water Resources Research*, 47, W03503.
- Brauchler, R., Böhm, G., Leven, C., Dietrich, P., & Sauter, M., 2013a. A laboratory study for tracer tomography, *Hydrogeology Journal*, 21, 1265–1274.
- Brauchler, R., Hu, R., Hu, L., Jiménez, S., Bayer, P., Dietrich, P., & Ptak, T., 2013b. Rapid field application of hydraulic tomography for resolving aquifer heterogeneity in unconsolidated sediments, *Water Resources Research*, 49(4), 2013–2024.
- Bregman, N. D., Bailey, R. C., & Chapman, C. H., 1989. Crosshole seismic tomography, *Geophysics*, 54, 200–215.
- Brunner, P., Therrien, R., Renard, P., Simmons, C. T., & Hendricks Franssen, H.-J., 2017. Advances in understanding river-groundwater interactions, *Reviews of Geophysics*, 55, 818–854.
- Butler Jr., J. J., 2019. *The Design, Performance, and Analysis of Slug Tests (2nd Edition)*, CRC Press.
- Börner, F. D., Schopper, J. R., & Weller, A., 1996. Evaluation of transport and storage properties in the soil and groundwater zone from induced polarization measurements, *Geophysical Prospecting*, 44, 583–601.
- Börner, J. H., Herdegen, V., Repke, J. U., & Spitzer, K., 2017. Spectral induced polarization of the three-phase system CO₂ – brine – sand under reservoir conditions, *Geophysical Journal International*, 208, 289–305.

- Bücker, M. & Hördt, A., 2013. Analytical modelling of membrane polarization with explicit parametrization of pore radii and the electrical double layer, *Geophysical Journal International*, 194(2), 804–813.
- Bücker, M., Flores Orozco, A., Undorf, S., & Kemna, A., 2019. On the role of stern- and diffuse-layer polarization mechanisms in porous media, *Journal of Geophysical Research: Solid Earth*, 124, 5656–5677.
- Cardiff, M., Barrash, W., & Kitanidis, P. K., 2013. Hydraulic conductivity imaging from 3-d transient hydraulic tomography at several pumping/observation densities, *Water Resources Research*, 49(11), 7311–7326.
- Cardiff, M., Zhou, Y., Barrash, W., & Kitanidis, P. K., 2020. Aquifer imaging with oscillatory hydraulic tomography: Application at the field scale, *Groundwater*, 58(5), 710–722.
- Carrera, J., Hidalgo, J. J., & Slooten, L. J., 2010. Computational and conceptual issues in the calibration of seawater intrusion models, *Hydrogeology Journal*, 18, 131–145.
- Chib, S., 2001. Markov chain monte carlo methods: Computation and inference, *Handbook of Econometrics*, 5, 3569–3649.
- Cirpka, O. A., Leven, C., Bastian, P., Ippisch, O., Patzelt, A., Meyer, A., & Klein, O., 2011. Tomographic methods in hydrogeology, *Geotechnologien Science Report*, 18, 35–45.
- Cole, K. S. & Cole, R. H., 1941. Dispersion and absorption in dielectrics - i. alternating current characteristics, *The Journal of Chemical Physics*, 9, 341–351.
- Comsol, 1998. Introduction to comsol multiphysics ®.
- Comunian, A., Renard, P., Straubhaar, J., & Bayer, P., 2011. Three-dimensional high resolution fluvio-glacial aquifer analog - part 2: Geostatistical modeling, *Journal of Hydrology*, 405, 10–23.
- Condon, L. E., Kollet, S., Bierkens, M. F. P., Fogg, G. E., Maxwell, R. M., Hill, M. C., Fransen, H.-J. H., Verhoef, A., Van Loon, A. F., Sulis, M., & Abesser, C., 2021. Global groundwater modeling and monitoring: Opportunities and challenges, *Water Resources Research*, 57, e2020WR029500.

- Costall, A. R., Harris, B. D., B., T., Wagner, F. M., & Pigois, J. P., 2020. Groundwater throughflow and seawater intrusion in high quality coastal aquifers, *Scientific Reports*, 10, 9866.
- Day-Lewis, F. D. & Bathija, A. P., 2022. Introduction to this special section: Hydrogeophysics, *The Leading Edge*, 41(8), 518–518.
- Day-Lewis, F. D., Slater, L. D., Robinson, J., Johnson, C. D., Terry, N., & Werkema, D., 2017. An overview of geophysical technologies appropriate for characterization and monitoring at fractured-rock sites, *Journal of Environmental Management*, 204, 709–720.
- De La Vaissiere, R., Morel, J., Noiret, A., Cote, P., Helmlinger, B., Sohrabi, R., Lavanchy, J.-M., Leveau, F., Nussbaum, C., & Morel, J., 2014. Excavation-induced fractures network surrounding tunnel: properties and evolution under loading, *Geological Society, London, Special Publications*, 400(1), 279–291.
- De Marsily, G., Delay, F., Goncalves, J., Renard, P., Teles, V., & Violette, S., 2005. Dealing with spatial heterogeneity, *Hydrogeology Journal*, 13, 161–183.
- Diersch, H. J. G., 2014. *FEFLOW - Finite Element Modeling of Flow, Mass and Heat Transport in Porous and Fractured Media*, Springer-Verlag Berlin Heidelberg.
- Dijkstra, E. W., 1959. A note on two problems in connexion with graphs, *Numerische Mathematik*, 1(1), 269–271.
- Dillon, P., Stuyfzand, P., Grischek, T., Lloria, M., Pyne, R. D. G., Jain, R. C., Bear, J., Schwarz, J., Wang, W., Fernandez, E., Stefan, C., Pettenati, M., van der Gun, J., Sprenger, C., Massmann, G., Scanlon, B. R., Xanke, J., Jokela, P., Zheng, Y., Rossetto, R., Shamrukh, M., Pavelic, P., Murray, E., Ross, A., Bonilla Valverde, J. P., Palma Nava, A., Ansems, N., Posavec, K., Ha, K., Martin, R., & Sapiano, M., 2019. Sixty years of global progress in managed aquifer recharge, *Hydrogeology Journal*, 27, 1–30.
- Divahar, J., Roberts, A. J., Mattner, T. W., Bunder, J. E., & Kevrekidis, I. G., 2024. Staggered grids for multidimensional multiscale modelling, *Computers & Fluids*, 271, 106167.
- Doetsch, J., Linde, N., & Binley, A., 2010. Structural joint inversion of time-lapse crosshole ert and gpr traveltime data, *Geophysical Research Letters*, 37(24), L24404.

- Doetsch, J., Fiandaca, G., Auken, E., Christiansen, A. V., Cahill, A. G., & Jakobsen, R., 2015. Field-scale time-domain spectral induced polarization monitoring of geochemical changes induced by injected CO₂ in a shallow aquifer, *Geophysics*, 80(2), 113–126.
- Dukhin, S. S., Shilov, V. N., & Bikerman, J. J., 1974. Dielectric phenomena and the double layer in disperse systems and polyelectrolytes, *Journal of the Electrochemical Society*, 121(4), 154C.
- Döll, P. & Fiedler, P., 2008. Global-scale modeling of groundwater recharge, *Hydrology and Earth System Sciences*, 12, 863–885.
- Earman, S. & Dettinger, M., 2011. Potential impacts of climate change on groundwater resources – a global review, *Journal of Water and Climate Change*, 2(4), 213–229.
- Epting, J., Huggenberger, P., Radny, D., Hammes, F., Hollender, J., Page, R. M., Weber, S., Bänninger, D., & Auckenthaler, A., 2018. Spatiotemporal scales of river-groundwater interaction – the role of local interaction processes and regional groundwater regimes, *Science of the Total Environment*, 618, 1224–1243.
- Fiandaca, G., Auken, E., Christiansen, A. V., & Gazoty, A., 2012. Time-domain-induced polarization: Full-decay forward modeling and 1d lateral constrained inversion of cole-cole parameters, *Geophysics*, 77(3), 213–225.
- Fiandaca, G., Ramm, J., Binley, A., Gazoty, A., Christiansen, A. V., & Auken, E., 2013. Resolving spectral information from time domain induced polarization data through 2-d inversion, *Geophysical Journal International*, 192, 631–646.
- Fiandaca, G., Madsen, L. M., & Maurya, P. K., 2018a. Re-parameterisations of the cole-cole model for improved spectral inversion of induced polarization data, *Near Surface Geophysics*, 16, 385–399.
- Fiandaca, G., Maurya, P. K., Balbarini, N., Hördt, A., Christiansen, A. V., Foged, N., Bjerg, P. L., & Auken, E., 2018b. Permeability estimation directly from logging-while-drilling induced polarization data, *Water Resources Research*, 54(4), 2851–2870.
- Fiandaca, G., Madsen, L. M., Olmo, M., Römhild, L., & Maurya, P., 2021. Inversion of hydraulic conductivity from induced polarisation, part a: Methodology and verification, *NSG2021 1st Conference on Hydrogeophysics*.

- Fiandaca, G., Olsson, P.-I., Maurya, P. K., Kühl, A., Bording, T., Dahlin, T., & Auken, E., 2022. Heterodox transients in time-domain-induced polarization, *Geophysics*, 87(1), E35–E47.
- Fiandaca, G., Zhang, B., Chen, J., Signora, A., Dauti, F., Galli, S., Sullivan, N. A. L., Bollino, A., & Viezzoli, A., 2023. Closing the gap between galvanic and inductive methods: Eemverter, a new 1d/2d/3d inversion tool for electric and electromagnetic data with focus on induced polarisation, *AEM 2023: Short abstracts*, pp. 52–66.
- Fiandaca, G., Zhang, B., Chen, J., Signora, A., Dauti, F., Galli, S., Sullivan, N. A. L., Bollino, A., & Viezzoli, A., 2024. Closing the gap between galvanic and inductive induced polarization: Eemverter, a new modelling tool for electric and electromagnetic data, *7th International IP Workshop, Lund (Sweden)*.
- Fischer, P., Jardani, A., Wang, X., Jourde, H., & Lecoq, N., 2017. Identifying flow networks in a karstified aquifer by application of the cellular automata-based deterministic inversion method (lez aquifer, france), *Water Resources Research*, 53(12), 10508–10522.
- Fischer, P., Jardani, A., & Jourde, H., 2020. Hydraulic tomography in coupled discrete-continuum concept to image hydraulic properties of a fractured and karstified aquifer (lez aquifer, france), *Advances in Water Resources*, 137, 103523.
- Flores Orozco, A., Steiner, M., Katona, T., Roser, N., Moser, C., Stumvoll, M. J., & Glade, T., 2022. Application of induced polarization imaging across different scales to understand surface and groundwater flow at the hofermuehle landslide, *CATENA*, 219, 106612.
- Gallistl, J., Weigand, M., Stumvoll, M., Ottowitz, D., Glade, T., & Orozco, A. F., 2018. Delineation of subsurface variability in clay-rich landslides through spectral induced polarization imaging and electromagnetic methods, *Engineering Geology*, 245, 292–308.
- Gan, Q. & Elswort, D., 2016. Production optimization in fractured geothermal reservoirs by coupled discrete fracture network modeling, *Geothermics*, 62, 131–142.
- Gao, G., Abubaker, A., & Habashy, T., 2012. Joint petrophysical inversion of electromagnetic and full-waveform seismic data, *Geophysics*, 77(3), WA3–WA18.

- Gasanzade, F., Pfeiffer, W. T., Witte, F., Tuschy, I., & Bauer, S., 2021. Subsurface renewable energy storage capacity for hydrogen, methane and compressed air – a performance assessment study from the north german basin, *Renewable and Sustainable Energy Reviews*, 149, 111422.
- Gazoty, A., Fiandaca, G., Pedersen, J., Auken, E., Christiansen, A. V., & Pedersen, J. K., 2012. Application of time domain induced polarization to the mapping of lithotypes in a landfill site, *Hydrology and Earth System Sciences*, 16, 1793–1804.
- Geuzaine, C. & Remacle, J.-F., 2009. Gmsh: A 3-D finite element mesh generator with built-in pre- and post-processing facilities, *International Journal for Numerical Methods in Engineering*, 79(11), 1309–1331.
- Ghalenoei, E., Dettmer, J., Ali, M. Y., & Kim, J. W., 2022. Trans-dimensional gravity and magnetic joint inversion for 3-d earth models, *Geophysical Journal International*, 230, 363–376.
- Giraud, J., Lindsay, M., Pakyuz-Charrier, E., Martin, R., Ogarko, V., & Jessell, M., 2018. Impact of uncertain geology in constrained geophysical inversion, *ASEG Extended Abstracts*, 1, 1–6.
- Gorelick, S. M. & Zheng, C., 2015. Global change and the groundwater management challenge, *Water Resources Research*, 51, 3031–3051.
- Gottlieb, J. & Dietrich, P., 1995. Identification of the permeability distribution in soil by hydraulic tomography, *Inverse Problems*, 11.2, 353.
- Green, P. J., 1995. Reversible jump Markov chain Monte Carlo computation and Bayesian model determination, *Biometrika*, 82(4), 711–732.
- Green, T. R., Taniguchi, M., Kooi, H., Gurdak, J. J., Allen, D. M., Hiscock, K. M., Treidel, H., & Aureli, A., 2011. Beneath the surface of global change: Impacts of climate change on groundwater on groundwater, *Journal of Hydrology*, 405, 532–560.
- Griebler, C., Briemann, H., Haberer, C. M., Kaschuba, S., Kellermann, C., Stumpp, C., Hegler, F., Kuntz, D., Walker-Hertkorn, S., & Lueders, T., 2016. Potential impacts of geothermal energy use and storage of heat on groundwater quality, biodiversity, and ecosystem processes, *Environmental Earth Sciences*, 75, 1–18.

- Guo, T., Zhang, Y., Zhang, W., Niu, B., He, J., Chen, M., Yu, Y., Xiao, B., & Xu, R., 2022. Numerical simulation of geothermal energy productivity considering the evolution of permeability in various fractures, *Applied Thermal Engineering*, 201, 117756.
- Guo, Z., E., F. G., Brusseau, M. L., LaBolle, E. M., & Lopez, J., 2019. Modeling groundwater contaminant transport in the presence of large heterogeneity: a case study comparing mt3d and rwhet, *Hydrogeology Journal*, 27, 1363–1371.
- Günther, T. & Martin, T., 2024. Inverting time-domain induced polarization field data using debye discretization, *7th International IP Workshop, Lund (Sweden)*.
- Günther, T., Rücker, C., & Spitzer, K., 2006. Three-dimensional modelling and inversion of dc resistivity data incorporating topography - ii. inversion, *Geophysical Journal International*, 166(2), 506–517.
- Hadgu, T., Karra, S., Kalinina, E., Makedonska, N., Hyman, J. D., Klise, K., Viswanathan, H. S., & Wang, Y., 2017. A comparative study of discrete fracture network and equivalent continuum models for simulating flow and transport in the far field of a hypothetical nuclear waste repository in crystalline host rock, *Journal of Hydrology*, 553, 59–70.
- Hao, Y., Yeh, T.-C. J., Xiang, J., Illman, W. A., Ando, K., Hsu, K.-C., & Lee, C.-H., 2008. Hydraulic tomography for detecting fracture zone connectivity, *Groundwater*, 46(2), 183–192.
- Hase, J., Gurin, G., Titov, K., & Kemna, A., 2022. Conversion of induced polarization data and their uncertainty from time domain to frequency domain using debye decomposition, *minerals*, 13(7), 955.
- Heinz, J., Kleineidam, S., Teutsch, G., & Aigner, T., 2003. Heterogeneity patterns of quaternary glaciofluvial gravel bodies (sw-germany): application to hydrogeology, *Sedimentary Geology*, 158, 1–23.
- Heldt, S., Wang, B., & Bauer, S., 2023. Parameter identification and range restriction through sensitivity analysis for a high-temperature heat injection test, *Geothermal Energy*, 11, 12.
- Helmholtz, H., 1879. Studien über electrische grenzsichten, *Annalen der Physik*, 243, 337–382.

- Hermans, T. & Irving, J., 2017. Facies discrimination with electrical resistivity tomography using a probabilistic methodology: effect of sensitivity and regularisation, *Near Surface Geophysics*, 15, 13–25.
- Hou, X., Hu, R., Yeh, T.-C. J., Li, Y., Qi, J., Song, Y., & Qiu, H., 2023. A short-term pumping strategy for hydraulic tomography based on the successive linear estimator, *Water Resources Research*, 59, e2022WR033831.
- Hu, L., Bayer, P., Alt-Epping, P., Tatomir, A., Sauter, M., & Brauchler, R., 2015. Time-lapse pressure tomography for characterizing co₂ plume evolution in a deep saline aquifer, *International Journal of Greenhouse Gas Control*, 39, 91–106.
- Hu, L., Doetsch, J., Brauchler, R., & Bayer, P., 2017. Characterizing co₂ plumes in deep saline formations; comparison and joint evaluation of time-lapse pressure and seismic tomography, *Geophysics*, 82(4), 1–18.
- Hu, R., 2011. *Hydraulic Tomography: A New Approach Coupling Hydraulic Travel Time, Attenuation and Steady Shape Inversions for High-Spatial Resolution Aquifer Characterization*, Thesis, Georg-August-Universität Göttingen.
- Hu, R., Brauchler, R., Herold, M., & Bayer, P., 2011. Hydraulic tomography analog outcrop study: Combining travel time and steady shape inversion, *Journal of Hydrology*, 409, 350–362.
- Huang, Y., Pang, Z., Kong, Y., & Watanabe, N., 2021. Assessment of the high-temperature aquifer thermal energy storage (ht-ates) potential in naturally fractured geothermal reservoirs with a stochastic discrete fracture network model, *Journal of Hydrology*, 603, 127188.
- Huysmans, M., Peeters, L., Moermans, G., & Dassargues, A., 2008. Relating small-scale sedimentary structures and permeability in a cross-bedded aquifer, *Journal of Hydrology*, 361, 41–51.
- Hönig, M. & Tezkan, B., 2007. 1d and 2d cole-cole-inversion of time-domain induced-polarization data, *Geophysical Prospecting*, 55, 117–133.
- Hördt, A., Druiventak, A., Blaschek, R., Binot, F., Kemna, A., Kreye, P., & Zisser, N., 2009. Case histories of hydraulic conductivity estimation with induced polarization at the field scale, *Near Surface Geophysics*, 7, 529–545.

- Höyng, D., Prommer, H., Blum, P., Grathwohl, P., & D’Affonseca, F. M., 2015. Evolution of carbon isotope signatures during reactive transport of hydrocarbons in heterogeneous aquifers, *Journal of Contaminant Hydrology*, 174, 10–27.
- Illman, W. A., 2014. Hydraulic tomography offers improved imaging of heterogeneity in fractured rocks, *Groundwater*, 52(5), 659–684.
- Illman, W. A., Liu, X., Takeuchi, S., Jim Yeh, T.-C., Ando, K., & Saegusa, H., 2009. Hydraulic tomography in fractured granite: Mizunami underground research site, Japan, *Water Resources Research*, 45(1), W01406.
- IPCC, 2023. Climate change 2023: Synthesis report. contribution of working groups i, ii and iii to the sixth assessment report of the intergovernmental panel on climate change [core writing team, h. lee and j. romero (eds.)], *IPCC, Geneva, Switzerland*, pp. 35–115.
- Irving, J. & Singha, K., 2010. Stochastic inversion of tracer test and electrical geophysical data to estimate hydraulic conductivities, *Water Resources Research*, 46(11), W11514.
- Jackson, D. D. & Matsuura, M., 1985. A bayesian approach to nonlinear inversion, *Journal of Geophysical Research: Solid Earth*, 90(B1), 581–591.
- JafarGandomi, A. & Binley, A., 2013. A bayesian trans-dimensional approach for the fusion of multiple geophysical datasets, *Journal of Applied Geophysics*, 96, 38–54.
- Jimenez, S., Brauchler, R., & Bayer, P., 2013. A new sequential procedure for hydraulic tomographic inversion, *Advances in Water Resources*, 62, 59–70.
- Karatzas, G. P., 2017. Developments on modeling of groundwater flow and contaminant transport, *Water Resources Management*, 31, 3235–3244.
- Kemna, A., Binley, A., & Slater, L., 2004. Crosshole ip imaging for engineering and environmental applications, *Geophysics*, 69(1), 97–107.
- Kemna, A., Binley, A., Cassiani, G., Niederleithinger, E., Revil, A., Slater, L., Williams, K. H., Orozco, A. F., Haegel, F. H., Hördt, A., Kruschwitz, S., Leroux, V., Titov, K., & Zimmermann, E., 2012. An overview of the spectral induced polarization method for near-surface applications, *Near Surface Geophysics*, 10, 453–468.

- Kessouri, P., Furman, A., Huisman, J. A., Martin, T., Mellage, A., Ntarlagiannis, D., Bücken, M., Ehosioko, S., Fernandez, P., Flores-Orozco, A., Kemna, A., Nguyen, F., Pilawski, T., Saneiyan, S., Schmutz, M., Schwartz, N., Weigand, M., Wu, Y., Zhang, C., & Placencia-Gomez, E., 2019. Induced polarization applied to biogeophysics: recent advances and future prospects, *Near Surface Geophysics*, 17, 595–621.
- Kitanidis, P., 1995. Quasi-linear geostatistical theory for inversing, *Water Resources Research*, 31(10), 2411–2419.
- Klepikova, M., Le Borgne, T., Bour, O., Gallagher, K., Hochreutener, R., & Lavenant, N., 2014. Passive temperature tomography experiments to characterize transmissivity and connectivity of preferential flow paths in fractured media, *Journal of Hydrology*, 512, 549–562.
- Klepikova, M., Brixel, B., & Jalali, M., 2020. Transient hydraulic tomography approach to characterize main flowpaths and their connectivity in fractured media, *Advances in Water Resources*, 136, 103500.
- Kong, X. Z., Deuber, C. A., Kittilä, A., Somogyvari, M., Mikutis, G., Bayer, P., Stark, W. J., & Saar, M. O., 2018. Tomographic reservoir imaging with dna-labeled silica nanotracers: The first field validation, *Environmental Science & Technology*, 52(23), 13681–13689.
- Kuang, X., Jiao, J. J., Zheng, C., Cherry, J. A., & Li, H., 2020. A review of specific storage in aquifers, *Journal of Hydrology*, 581, 124282.
- Kushnir, A. R. L., Heap, M. J., & Baud, P., 2018. Assessing the role of fractures on the permeability of the permo-triassic sandstones at the soultz-sous-forêts (france) geothermal site, *Geothermics*, 74, 181–189.
- Lajaunie, M., Maurya, P. K., & Fiandaca, G., 2016. Comparison of cole-cole and constant phase angle modeling in time-domain induced polarization, *4th International Workshop on Induced Polarization*.
- Lang, P. S., Paluszny, A., Nejati, M., & Zimmerman, R. W., 2018. Relationship between the orientation of maximum permeability and intermediate principal stress in fractured rocks, *Water Resources Research*, 54(11), 8734–8755.

- Lei, Q., Latham, J.-P., & Tsang, C.-F., 2017a. The use of discrete fracture networks for modelling coupled geomechanical and hydrological behaviour of fractured rocks, *Computers and Geotechnics*, 85, 151–176.
- Lei, Q., Latham, J.-P., Xiang, J., & Tsang, C.-F., 2017b. Role of natural fractures in damage evolution around tunnel excavation in fractured rocks, *Engineering Geology*, 231, 100–113.
- Lelièvre, P. G. & Farquharson, C. G., 2013. Gradient and smoothness regularization operators for geophysical inversion on unstructured meshes, *Geophysical Journal International*, 195(1), 330–341.
- Leroy, P. & Revil, A., 2009. A mechanistic model for the spectral induced polarization of clay materials, *Journal of Geophysical Research*, 114, B10202.
- Lesmes, D. P. & Morgan, F. D., 2001. Dielectric spectroscopy of sedimentary rocks, *Journal of Geophysical Research: Solid Earth*, 106(B7), 13329–13346.
- Li, H., Lu, C., Werner, A. D., Irvine, D. J., & Luo, J., 2022a. Impacts of heterogeneity on aquifer storage and recovery in saline aquifers, *Water Resources Research*, 58, e2021WR031306.
- Li, L., Zhang, Q., Zhou, Z., Cui, Y., Shao, J., & Zhao, Y., 2022b. Groundwater circulation patterns in bedrock aquifers from a pre-selected area of high-level radioactive waste repository based on two-dimensional numerical simulation, *Journal of Hydrology*, 610, 127849.
- Li, X., Li, D., Xu, Y., & Feng, X., 2020. A dfn based 3d numerical approach for modeling coupled groundwater flow and solute transport in fractured rock mass, *International Journal of Heat and Mass Transfer*, 149, 119179.
- Linde, N. & Doetsch, J., 2016. *Joint Inversion in hydrogeophysics and near-surface geophysics*, chap. 7, pp. 119–135, John Wiley & Sons, New Jersey.
- Linde, N., Finsterle, S., & Hubbard, S., 2006. Inversion of tracer test data using tomographic constraints, *Water Resources Research*, 42(4), W04410.
- Linde, N., Renard, P., Mukerji, T., & Caers, J., 2015. Geological realism in hydrogeological and geophysical inverse modeling: A review, *Advances in Water Resources*, 86, 86–101.

- Liu, G., Zhou, C., Rao, Z., & Liao, S., 2021. Impacts of fracture network geometries on numerical simulation and performance prediction of enhanced geothermal systems, *Renewable Energy*, 171, 492–504.
- Liu, Q., 2022. *Characterization of Hydraulic Properties in Fractured Aquifers Using Slug Test-based Hydraulic Tomography and Thermal Tracer Tomography*, Ph.D. thesis, Georg-August-Universität Göttingen.
- Liu, Q., Hu, R., Hu, L., Xing, Y., Qiu, P., Yang, H., Fischer, S., & Ptak, T., 2022. Investigation of hydraulic properties in fractured aquifers using cross-well travel-time based thermal tracer tomography: Numerical and field experiments, *Journal of Hydrology*, 609, 127751.
- Liu, Q., Hu, L., Hu, R., Brauchler, R., Xing, Y., Qi, J., & Ptak, T., 2023. Characterization of aquifer heterogeneity by tomographic slug test responses considering wellbore effects, *Journal of Hydrology*, 627(B), 130472.
- Liu, W. & Manga, M., 2009. Changes in permeability caused by dynamic stresses in fractured sandstone, *Geophysical Research Letters*, 36(20), L20307.
- Loke, M. H. & Dahlin, T., 2002. A comparison of the gauss–newton and quasi-newton methods in resistivity imaging inversion, *Journal of Applied Geophysics*, 49(3), 149–162.
- Loke, M. H., Acworth, I., & Dahlin, T., 2003. A comparison of smooth and blocky inversion methods in 2d electrical imaging surveys, *Exploration Geophysics*, 34, 182–187.
- Luo, N., Zhao, Z., Illman, W. A., Zha, Y., Mok, C. M. W., & Yeh, T.-C. J., 2023. Three-dimensional steady-state hydraulic tomography analysis with integration of cross-hole flowmeter data at a highly heterogeneous site, *Water Resources Research*, 59(6), e2022WR034034.
- Madsen, L. M., Fiandaca, G., Auken, E., & Christiansen, A. V., 2017. Time-domain induced polarization – an analysis of cole–cole parameter resolution and correlation using markov chain monte carlo inversion, *Geophysical Journal International*, 211, 1341–1353.
- Madsen, L. M., Fiandaca, G., & Auken, E., 2020. 3-d time-domain spectral inversion of resistivity and full-decay induced polarization data - full solution of

- poisson's equation and modelling of the current waveform, *Geophysical Journal International*, 223, 2101–2116.
- Makedonska, N., Jafarov, E., Doe, T., Schwering, P., Neupane, G., & EGS Col-lab Team, 2020. Simulation of injected flow pathways in geothermal fractured reservoir using discrete fracture network model, *45th Workshop on Geothermal Reservoir Engineering, Stanford University, February 10-12, 2020*.
- Mao, D., Liu, Z., Wang, W., Li, S., Gao, Y., Xu, Z., & Zhang, C., 2018. An application of hydraulic tomography to a deep coal mine: Combining traditional pumping tests with water inrush incidents, *Journal of Hydrology*, 567, 1–11.
- Marchant., D., Haber, E., & Oldenburg, D. W., 2014. Three-dimensional modeling of ip effects in time-domain electromagnetic data, *Geophysics*, 79(6), 1ND–Z201.
- Marshall, D. J. & Madden, T. R., 1959. Induced polarization, a study of its causes, *Geophysics*, 4, 790–816.
- Martin, T., Günther, T., Orozco, A. F., & Dahlin, T., 2020. Evaluation of spectral induced polarization field measurements in time and frequency domain, *Journal of Applied Geophysics*, 180, 104141.
- Martin, T., Pauw, P. S., Karoulis, M., Mendoza, A., Günther, T., Madsen, L. M., Maurya, P. K., Doetsch, J., Rejkjaer, S., Dahlin, T., & Fiandaca, G., 2021. Inversion of hydraulic conductivity from induced polarisation, part b: Field examples from five countries, *NSG2021 1st Conference on Hydrogeophysics*.
- Martin, T., Günther, T., Weller, A., Kass, A., Grombacher, D., Butron, C., Men-doza, A., & Dahlin, T., 2024. Estimating hydraulic properties from ip and nmr measurements at field and laboratory scale, *7th International IP Workshop, Lund (Sweden)*.
- Maurya, P. K., Balbarini, N., Moller, I., Ronde, V., Christiansen, A. V., Bjerg, P. L., Auken, E., & Fiandaca, G., 2018a. Subsurface imaging of water electrical conductivity, hydraulic permeability and lithology at contaminated sites by induced polarization, *Geophysical Journal International*, 213, 770–785.
- Maurya, P. K., Fiandaca, G., Christiansen, A. V., & Auken, E., 2018b. Field-scale comparison of frequency- and time-domain spectral induced polarization, *Geophysical Journal International*, 214, 1441–1466.

- Maxwell, J. C., 1873. *A Treatise on Electricity and Magnetism*, Oxford, Clarendon Press.
- McLachlan, P., Blanchy, G., Chambers, J., Sorensen, J., Uhlemann, S., Wilkinson, P., & Binley, A., 2021. The application of electromagnetic induction methods to reveal the hydrogeological structure of a riparian wetland, *Water Resources Research*, 57(6), e2020WR029221.
- Mehl, S., Hill, M. C., & Leake, S. A., 2006. Comparison of local grid refinement methods for modflow, *Groundwater*, 44(6), 792–796.
- Mogaji, K. A., Lim, H. S., & Abdullah, K., 2015. Modeling of groundwater recharge using a multiple linear regression (mlr) recharge model developed from geophysical parameters: a case of groundwater resources management, *Environmental Earth Sciences*, 73, 1217–1230.
- Mojabi, P. & LoVetri, J., 2009. Overview and classification of some regularization techniques for the gauss-newton inversion method applied to inverse scattering problems, *IEEE Transactions on Antennas and Propagation*, 57(9), 2658–2665.
- Mollaret, C., Wagner, F., Hilbich, C., Scapozza, C., & Hauck, C., 2020. Petrophysical joint inversion applied to alpine permafrost field sites to image subsurface ice, water, air, and rock contents, *Frontiers in Earth Science*, 8, 85.
- Neumann, S. P., 2005. Trends, prospects and challenges in quantifying flow and transport through fractured rocks, *Hydrogeology Journal*, 13, 124–147.
- Nordsiek, S. & Weller, A., 2008. A new approach to fitting induced-polarization spectra, *Geophysics*, 73(6), 235–245.
- Oldenburg, D. W. & Li, Y., 1994. Inversion of induced polarization data, *Geophysics*, 59(9), 1327–1341.
- Olhoeft, G. R., 1985. Low-frequency electrical properties, *Geophysics*, 50(12), 2492–2503.
- Olsson, P. I., Fiandaca, G., Larsen, J. J., Dahlin, T., & Auken, E., 2016. Doubling the spectrum of time-domain induced polarization by harmonic de-noising, drift correction, spike removal, tapered gating and data uncertainty estimation, *Geophysical Journal International*, 207, 774–784.

- Orozco, A. F., Kemna, A., Oberdörster, C., Zschornak, L., Leven, C., Dietrich, P., & Weiss, H., 2012. Delineation of subsurface hydrocarbon contamination at a former hydrogenation plant using spectral induced polarization imaging, *Journal of Contaminant Hydrology*, 136–137, 131–144.
- Parker, B. L., Cherry, J. A., & Chapman, S. W., 2012. Discrete fracture network approach for studying contamination in fractured rock, *Aqua mundi*, Am06052, 101–116.
- Pelton, W., Ward, S., Hallof, P., Sill, W., & Nelson, P., 1978. Mineral discrimination and removal of inductive coupling with multifrequency ip, *Geophysics*, 43, 588–609.
- Pirot, G., Linde, N., Mariethoz, G., & Bradford, J., 2017. Probabilistic inversion with graph cuts: Application to the boise hydrogeophysical research site, *Water Resources Research*, 53(2), 1231–1250.
- Poduri, S. & Kambhammettu, B. V. N. P., 2021. On the performance of pilot-point based hydraulic tomography with a geophysical a priori model, *Groundwater*, 59(2), 214–225.
- Pouladi, B., Linde, N., Longuevergne, L., & Bour, O., 2021. Individual and joint inversion of head and flux data by geostatistical hydraulic tomography, *Advances in Water Resources*, 154, 103960.
- Qiu, H., Hu, R., Luo, N., Illman, W. A., & Hou, X., 2023. Comparison of travel-time and geostatistical inversion approaches for hydraulic tomography: Synthetic modeling study on data density and well configuration issues, *Journal of Hydrology*, 618, 129247.
- Qiu, J., Wang, W., Ma, L., Dang, B., & Sun, X., 2024. Identification of preferential flow paths by hydraulic tomography compared with tracer test and the groundwater contour map in coal mine water hazard area, *Journal of Hydrology*, 631, 130816.
- Qiu, P., 2020. *Automated data processing and numerical methods for travel-time based hydraulic tomography*, Ph.D. thesis, Georg-August-Universität Göttingen.
- Ramirez, A. L., Nitao, J. J., Hanley, W. G., Aines, R., Glaser, R. E., Sengupta, S. K., Dyer, K. M., Hickling, T. L., & Daily, W. D., 2005. Stochastic inversion of

- electrical resistivity changes using a markov chain monte carlo approach, *Journal of Geophysical Research: Solid Earth*, 110(B2), B02101.
- Rau, G. C., Cuthbert, M. O., Post, V. E. A., Schweizer, D., Acworth, R. I., Andersen, M. S., Blum, P., Carrara, E., Rasmussen, T. C., & Ge, S., 2020. Future-proofing hydrogeology by revising groundwater monitoring practice, *Hydrogeology Journal*, 28, 2963–2969.
- Refsgaard, J. C., Christensen, S., Sonnenborg, T. O., Seifert, D., Hojberg, A. L., & Troldborg, L., 2012. Review of strategies for handling geological uncertainty in groundwater flow and transport modeling, *Advances in Water Resources*, 36, 36–50.
- Ren, S., Zhang, Y., Jim Yeh, T.-C., Wang, Y., & Carr, B. J., 2021. Multiscale hydraulic conductivity characterization in a fractured granitic aquifer: The evaluation of scale effect, *Water Resources Research*, 57(9), e2020WR028482.
- Revil, A., 2012. Spectral induced polarization of shaly sands: Influence of the electrical double layer, *Water Resources Research*, 48, W02517.
- Revil, A. & Florsch, N., 2010. Determination of permeability from spectral induced polarization in granular media, *Geophysical Journal International*, 181, 1480–1498.
- Revil, A. & Glover, P. W. J., 1997. Theory of ionic-surface electrical conduction in porous media, *Physical Review B*, 55(3), 1757–1773.
- Revil, A., Karaoulis, M., Johnson, T., & Kemna, A., 2012a. Review: Some low-frequency electrical methods for subsurface characterization and monitoring in hydrogeology, *Hydrogeology Journal*, 20, 617–658.
- Revil, A., Koch, K., & Holliger, K., 2012b. Is it the grain size or the characteristic pore size that controls the induced polarization relaxation time of clean sands and sandstones?, *Water Resources Research*, 48, W05602.
- Revil, A., Florsch, N., & Camerlynck, C., 2014. Spectral induced polarization porosimetry, *Geophysical Journal International*, 198, 1016–1033.
- Revil, A., Binley, A., Mejus, L., & Kessouri, P., 2015. Predicting permeability from the characteristic relaxation time and intrinsic formation factor of complex conductivity spectra, *Water Resources Research*, 51, 6672–6700.

- Ringel, L. M., Somogyvari, M., Jalali, M., & Bayer, P., 2019. Comparison of hydraulic and tracer tomography for discrete fracture network inversion, *geosciences*, 9(6), 274.
- Ringel, L. M., Jalali, M., & Bayer, P., 2021. Stochastic inversion of three-dimensional discrete fracture network structure with hydraulic tomography, *Water Resources Research*, 57(12), e2021WR030401.
- Ringel, L. M., Jalali, M., & Bayer, P., 2022. Characterization of the highly fractured zone at the grimsel test site based on hydraulic tomography, *Hydrology and Earth System Sciences*, 26, 6443–6455.
- Ringel, L. M., Illman, W. A., & Bayer, P., 2024. Recent developments, challenges, and future research directions of tomographic characterization of fractured aquifers, *Journal of Hydrology*, 631, 130709.
- Robinson, J., Slater, L., Weller, A., Keating, K., Robinson, T., Rose, C., & Parker, B., 2018. On permeability prediction from complex conductivity measurements using polarization magnitude and relaxation time, *Water Resources Research*, 54, 3436–3452.
- Römhild, L., Sonntag, M., Kiyani, D., Rogers, R., Rath, V., & Börner, J. H., 2019. Anisotropic complex electrical conductivity of black shale and mudstone from the moffat shale group (ireland), *Near Surface Geophysics*, 17, 675–690.
- Römhild, L., Fiandaca, G., Hu, L., Meyer, L., & Bayer, P., 2022a. Imaging hydraulic conductivity in near-surface aquifers by complementing cross-borehole induced polarization with hydraulic experiments, *Advances in Water Resources*, 170, 104322.
- Römhild, L., Sonntag, M., Kiyani, D., Rogers, R., Rath, V., & Börner, J. H., 2022b. Anisotropic broadband spectral induced polarization (sip) data of black shale and mudstone from the moffat shale group (ireland), *GFZ Data Services*.
- Römhild, L., Ringel, L. M., Liu, Q., Hu, L., Ptak, T., & Bayer, P., 2024a. Hybrid discrete fracture network inversion of hydraulic tomography data from a fractured-porous field site, *Water Resources Research*, 60, e2023WR036035.
- Römhild, L., Fiandaca, G., & Bayer, P., 2024b. Joint inversion of induced polarization and hydraulic tomography data for hydraulic conductivity imaging, *Geophysical Journal International*, 238(2), 960–973.

- Rücker, C., Günther, T., & Wagner, F. M., 2017. pygimli: An open-source library for modelling and inversion in geophysics, *Computers and Geosciences*, 109, 106–123.
- Schlumberger, C., 1920. Etude sur la prospection électrique du sous-sol, *Gauthier-Villars*.
- Schön, J., 2015. *Physical Properties of Rocks - Fundamentals and Principles of Petrophysics*, vol. 18 of , Elsevier, 2nd edn.
- Schwarz, G., 1962. A theory of the low-frequency dielectric dispersion of colloidal particles in electrolyte solution, *Journal of Physical Chemistry*, 66, 2636–2642.
- Seigel, H., Nabighian, M., Parasnis, D. S., & Vozoff, K., 2007. The early history of the induced polarization method, *The Leading Edge*, 26(3), 312–321.
- Seigel, H. O., 1959. Mathematical formulation and type curves for induced polarization, *Geophysics*, 24, 547–565.
- Sharifi, F., Tezkan, B., Ibraheem, I. M., Yogeshwar, P., & Bergers, R., 2024. Ip-distorted transient electromagnetic data modelling, *7th International IP Workshop, Lund (Sweden)*.
- Signora, A., Galli, S., Dauti, F., Sullivan, N. A. L., Lucchelli, A., Gisolo, M., & Fian-daca, G., 2024. Joint inversion of e&em data with ip modelling: The hydrogeosite case study, *7th International IP Workshop, Lund (Sweden)*.
- Singha, K., Day-Lewis, F. D., Johnson, T., & Slater, L. D., 2015. Advances in interpretation of subsurface processes with time-lapse electrical imaging, *Hydrological Processes*, 29(6), 1549–1576.
- Slater, L., 2007. Near surface electrical characterization of hydraulic conductivity: From petrophysical properties to aquifer geometries - a review, *Surv Geophys*, 28, 169–197.
- Slater, L. & Lesmes, D. P., 2002. Electrical-hydraulic relationships observed for unconsolidated sediments, *Water Resources Research*, 38(10), 1213.
- Somogyvari, M. & Bayer, P., 2017. Field validation of thermal tracer tomography for reconstruction of aquifer heterogeneity, *Water Resources Research*, 53(6), 5070–5084.

- Somogyvári, M., Jalali, M., Parras, S. J., & Bayer, P., 2017. Synthetic fracture network characterization with transdimensional inversion, *Water Resources Research*, 53(6), 5104–5123.
- Somogyvári, M., Kühn, M., & Reich, S., 2019. Reservoir-scale transdimensional fracture network inversion, *Advances in Geosciences*, 49, 207–214.
- Song, Y., Hu, R., Liu, Q., Qiu, H., Hou, X., Qi, J., & Konadu-Amoah, B., 2023. Comparison of hydraulic travel time and attenuation inversions, thermal tracer tomography and geostatistical inversion for aquifer characterization: A numerical study, *Water*, 15, 2401.
- Sullivan, N. A. L., Viezzoli, A., & Fiandaca, G., 2024. Eemstudio: a qgis plugin for processing and modelling of electric and electromagnetic data with focus on induced polarization, *7th International IP Workshop, Lund (Sweden)*.
- Sun, Z., Sandoval, L., Crystal-Ornelas, R., Mousavi, S. M., Wang, J., Lin, C., Cristea, N., Tong, D., Carande, W. H., Ma, X., Rao, Y., Bednar, J. A., Tan, A., Wang, J., Purushotham, S., Gill, T. E., Chastang, J., Howard, D., Holt, B., Gangodagamage, C., Zhao, P., Rivas, P., Chester, Z., Orduz, J., & John, A., 2022. A review of earth artificial intelligence, *Computers and Geosciences*, 159, 105034.
- Sánchez-León, E., Leven, C., Erdal, D., & Cirpka, O. A., 2020. Comparison of two ensemble-kalman filter based methods for estimating aquifer parameters from real 3-d hydraulic and tracer tomographic tests, *Geosciences (Switzerland)*, 10(11), 1–30.
- Tarasov, A. & Titov, K., 2013. On the use of the cole-cole equations in spectral induced polarization, *Geophysical Journal International*, 195, 352–356.
- Taylor, R. G., Scanlon, B., Döll, P., Rodell, M., van Beek, R., Wada, Y., Lounguevergne, L., Leblanc, M., Famiglietti, J. S., Edmunds, M., Konikow, L., Green, T. R., Chen, J., Taniguchi, M., Bierkens, M. F. P., MacDonald, A., Fan, Y., Maxwell, R. M., Yechieli, Y., Gurdak, J. J., Allen, D. M., Shansudduha, M., Hiscock, K., Yeh, P. J.-F., Holman, I., & Treidel, H., 2013. Ground water and climate change, *Nature Climate Change*, 3, 322–329.
- Thalund-Hansen, R., Troldborg, M., Levy, L., Christiansen, A. V., Bording, T. S., & Bjerg, P. L., 2023. Assessing contaminant mass discharge uncer-

- tainty with application of hydraulic conductivities derived from geoelectrical cross-borehole induced polarization and other methods, *Water Resources Research*, 59, WR034360.
- Thibaut, R., Laloy, E., & Hermans, T., 2021. A new framework for experimental design using bayesian evidential learning: The case of wellhead protection area, *Journal of Hydrology*, 603(A), 126903.
- Tiedeman, C. R. & Barrash, W., 2020. Hydraulic tomography: 3d hydraulic conductivity, fracture network, and connectivity in mudstone, *Groundwater*, 58(2), 238–257.
- Titov, K., Tarasov, A., Ilyin, Y., Seleznev, N., & Boyd, A., 2010. Relationships between induced polarization relaxation time and hydraulic properties of sandstone, *Geophysical Journal International*, 180, 1095–1106.
- Tsang, C.-F., Neretnieks, I., & Tsang, Y., 2015. Hydrologic issues associated with nuclear waste repositories, *Water Resources Research*, 51(9), 6923–6972.
- Turco, F., Azevedo, L., Grana, D., Crutchley, G., & Gorman, A., 2021. Characterization of gas hydrate systems on the hikurangi margin (new zealand) through geostatistical seismic and petrophysical inversion, *Geophysics*, 86(6), R825–R838.
- Ulrych, T. J., Sacchi, M. D., & Woodbury, A., 2001. A bayes tour of inversion: A tutorial, *Geophysics*, 66(1), 14–357.
- van der Walt, S., Schönberger, J., Nunez-Iglesias, J., Boulogne, F., Warner, J., Yager, N., Gouillart, E., & Yu, T., 2014. scikit-image: Image processing in python, *PeerJ*, 2, e453.
- Vasco, D. W., Keers, H., & Karasaki, K., 2000. Estimation of reservoir properties using transient pressure data: An asymptotic approach, *Water Resources Research*, 36(12), 3447–3465.
- Vazaios, I., Vlachopoulos, N., & Diederichs, M. S., 2019. Assessing fracturing mechanisms and evolution of excavation damaged zone of tunnels in interlocked rock masses at high stresses using a finite-discrete element approach, *Journal of Rock Mechanics and Geotechnical Engineering*, 11(4), 701–722.
- Vesnaver, A. & Böhm, G., 2000. Staggered or adapted grids for seismic tomography?, *The Leading Edge*, pp. 944–950.

- Vilhelmsen, T. N., Behroozmand, A. A., Christensen, S., & Nielsen, T. H., 2014. Joint inversion of aquifer test, mrs, and tem data, *Water Resources Research*, 50, 3956–3975.
- Vinegar, H. J. & Waxman, M. H., 1984. Induced polarization of shaly sands, *Geophysics*, 49(8), 1267–1287.
- Wagner, K. W., 1914. Erklärung der dielektrischen nachwirkungsvorgänge auf grund maxwellscher vorstellungen, *Archiv für Elektrotechnik*, 2, 371–387.
- Wang, C., Briggs, M. A., Day-Lewis, F. D., & Slater, L. D., 2021a. Characterizing physical properties of streambed interface sediments using in situ complex electrical conductivity measurements, *Water Resources Research*, 57(2), e2020WR027995.
- Wang, H., Cui, Y.-J., Vu, M. N., Talandier, J., & Conil, N., 2022. Fracture effect on the hydro-mechanical behaviour of callovo-oxfordian claystone, *Engineering Geology*, 303, 106674.
- Wang, W., Zhao, W., Qian, J., Ma, L., Wang, D., & Hou, X., 2021b. Potential of hydraulic tomography in exploring the preferential flowpaths of water inrush in coal mine areas, *Journal of Hydrology*, 602, 126830.
- Wang, Z., Bovik, A., Sheik, H., & Simoncelli, E., 2004. Image quality assessment: From error visibility to structural similarity, *IEEE Transactions on Image Processing*, 13(4), 600–612.
- Weigand, M. & Kemna, A., 2016. Relationship between cole–cole model parameters and spectral decomposition parameters derived from sip data, *Geophysical Journal International*, 205, 1414–1419.
- Weller, A., Seichter, M., & Kampke, A., 1996. Induced-polarization modelling using complex electrical conductivities, *Geophysical Journal International*, 127, 387–398.
- Weller, A., Slater, L., & Nordsiek, S., 2013. On the relationship between induced polarization and surface conductivity: Implications for petrophysical interpretation of electrical measurements, *Geophysics*, 78(5), D315–D325.
- Weller, A., Slater, L., Binley, A., Nordsiek, S., & Xu, S., 2015. Permeability prediction based on induced polarization: Insights from measurements on sandstone and

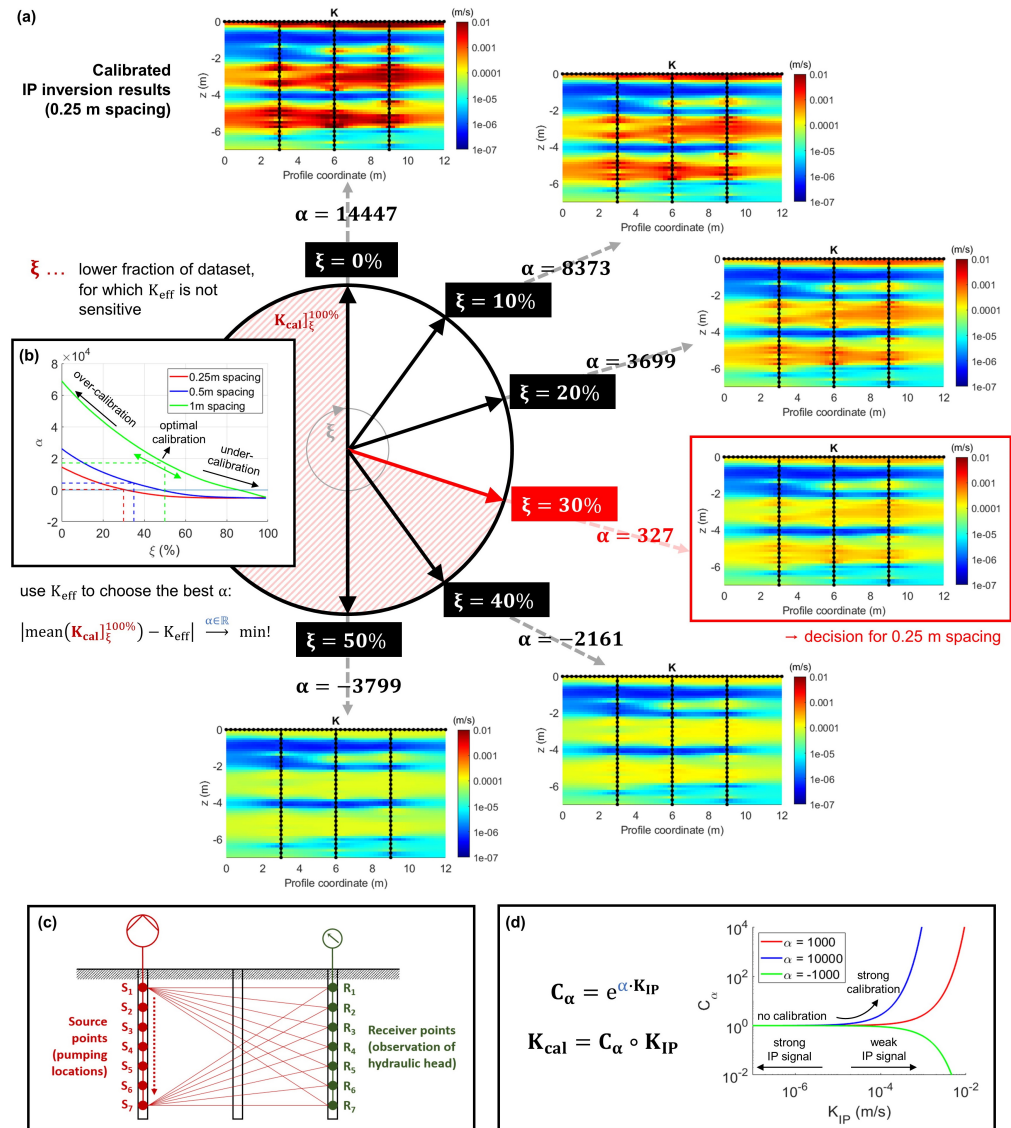
- unconsolidated samples spanning a wide permeability range, *Geophysics*, 80(2), D161–D173.
- Weller, A., Zhang, Z., Slater, L., Kruschwitz, S., & Halisch, M., 2016. Induced polarization and pore radius - a discussion, *Geophysics*, 81(5), D519–D526.
- Werner, H., 2013. *Strukturgeologische Charakterisierung eines Geothermietestfeldes auf der Basis bohrlochgeophysikalischer Messdaten und Bohrkerngefügen auf dem Göttinger Nordcampus*, Master's thesis, University of Göttingen.
- Woodbury, A. & Zhang, K., 2001. Lanczos method for the solution of groundwater flow in discretely fractured porous media, *Advances in Water Resources*, 24(6), 621–630.
- Woodward, S. J. R., Wöhling, T., & Stenger, R., 2016. Uncertainty in the modelling of spatial and temporal patterns of shallow groundwater flow paths: The role of geological and hydrological site information, *Journal of Hydrology*, 534, 680–694.
- Wu, C. M., Yeh, T. C. J., Zhu, J., Tim, H. L., Hsu, N. S., Chen, C. H., & Sancho, A. F., 2005. Traditional analysis of aquifer tests: Comparing apples to oranges?, *Water Resources Research*, 41(9), 1–12.
- Wu, X., 2017. Structure-, stratigraphy- and fault-guided regularization in geophysical inversion, *Geophysical Journal International*, 210(1), 184–195.
- Xia, R., Liang, Y., Yeh, T.-C. J., Dang, X., Gu, X., & Xu, B., 2023. Characterizing hydraulic heterogeneity of bayin river basin using river stage tomography, *Journal of Hydrology*, 621, 129547.
- Yang, H., Hu, R., Qiu, P., Liu, Q., Xing, Y., Tao, R., & Ptak, T., 2020. Application of wavelet de-noising for travel-time based hydraulic tomography, *Water*, 12(6), 1533.
- Yeh, J. & Lee, C. H., 2007. Time to change the way we collect and analyze data for aquifer characterization, *Groundwater*, 45, 116–118.
- Yeh, J. & Liu, S., 2000. Hydraulic tomography: Development of a new aquifer test method, *Water Resources Research*, 36(8), 2095–2105.
- You, X., Liu, S., Dai, C., Guo, Y., Zhong, G., & Duan, Y., 2020. Contaminant occurrence and migration between high- and low-permeability zones in groundwater systems: A review, *Science of The Total Environment*, 743, 140703.

- Yu, S. & Ma, J., 2021. Deep learning for geophysics: Current and future trends, *Reviews of Geophysics*, 59, e2021RG000742.
- Yu, X. & Michael, H. A., 2022. Impacts of the scale of representation of heterogeneity on simulated salinity and saltwater circulation in coastal aquifers, *Water Resources Research*, 58(1), e2020WR029523.
- Yue, W., 2019. Pore-scale explanation of the archie's cementation exponent: Microstructure, electrical anisotropy, and numerical experiments, *Geophysical Research Letters*, 46, 5799–5807.
- Zarif, F., Kessouri, P., & Slater, L., 2017. Recommendations for field-scale induced polarization (ip) data acquisition and interpretation, *Journal of Environmental and Engineering Geophysics*, 22(4), 395–410.
- Zech, A., Zehner, B., Kolditz, O., & Attinger, S., 2016. Impact of heterogeneous permeability distribution on the groundwater flow systems of a small sedimentary basin, *Journal of Hydrology*, 532, 90–101.
- Zelt, C. A. & Smith, R. B., 1992. Seismic travelttime inversion for 2-d crustal velocity structure, *Geophysical Journal International*, 108, 16–34.
- Zha, Y., Yeh, T.-C. J., Illman, W. A., Tanaka, T., Bruines, P., Onoe, H., & Saegusa, H., 2015. What does hydraulic tomography tell us about fractured geological media? a field study and synthetic experiments, *Journal of Hydrology*, 531, 17–30.
- Zhang, N., Sun, H., Liu, D., & Liu, S., 2024. Bayesian inversion and uncertainty analysis, *Near Surface Geophysics*, 22.
- Zhang, Y., Wang, L., Li, H., Zhang, Y., & Fu, G., 2020. Experimental study of the permeability of fractured sandstone under complex stress paths, *Energy Science & Engineering*, 8, 3217–3227.
- Zhao, Z. & Illman, W. A., 2018. Three-dimensional imaging of aquifer and aquitard heterogeneity via transient hydraulic tomography at a highly heterogeneous field site, *Journal of Hydrology*, 559, 392–410.
- Zhao, Z. & Ilman, W. A., 2022. Improved high-resolution characterization of hydraulic conductivity through inverse modeling of hpt profiles and steady-state hydraulic tomography: Field and synthetic studies, *Journal of Hydrology*, 612, 128124.

-
- Zhao, Z., Illman, W. A., Yeh, T.-C. J., Berg, S. J., & Mao, D., 2015. Validation of hydraulic tomography in an unconfined aquifer: A controlled sandbox study, *Water Resources Research*, 51, 4137–4155.
- Zhao, Z., Illman, W. A., Zha, Y., Yeh, J., Mok, C. M. B., Berg, S. J., & Han, D., 2019. Transient hydraulic tomography analysis of fourteen pumping tests at a highly heterogeneous multiple aquifer-aquitard system, *water*, 11(9), 1864.
- Zhao, Z., Lin, Y.-F., Stumpf, A., & Wang, X., 2022. Assessing impacts of ground-water on geothermal heat exchangers: A review of methodology and modeling, *Renewable Energy*, 190, 121–147.
- Zhao, Z., Luo, N., & Illman, W. A., 2023. Geostatistical analysis of high-resolution hydraulic conductivity estimates from the hydraulic profiling tool and integration with hydraulic tomography at a highly heterogeneous field site, *Journal of Hydrology*, 617, 129060.
- Zhdanov, M. S., 2015. *Inverse Theory and Applications in Geophysics, Second Edition*, Elsevier.
- Zisser, N., Kemna, A., & Nover, G., 2010. Relationship between low-frequency electrical properties and hydraulic permeability of low-permeability sandstones, *Geophysics*, 75(3), 1MJ–Z72.

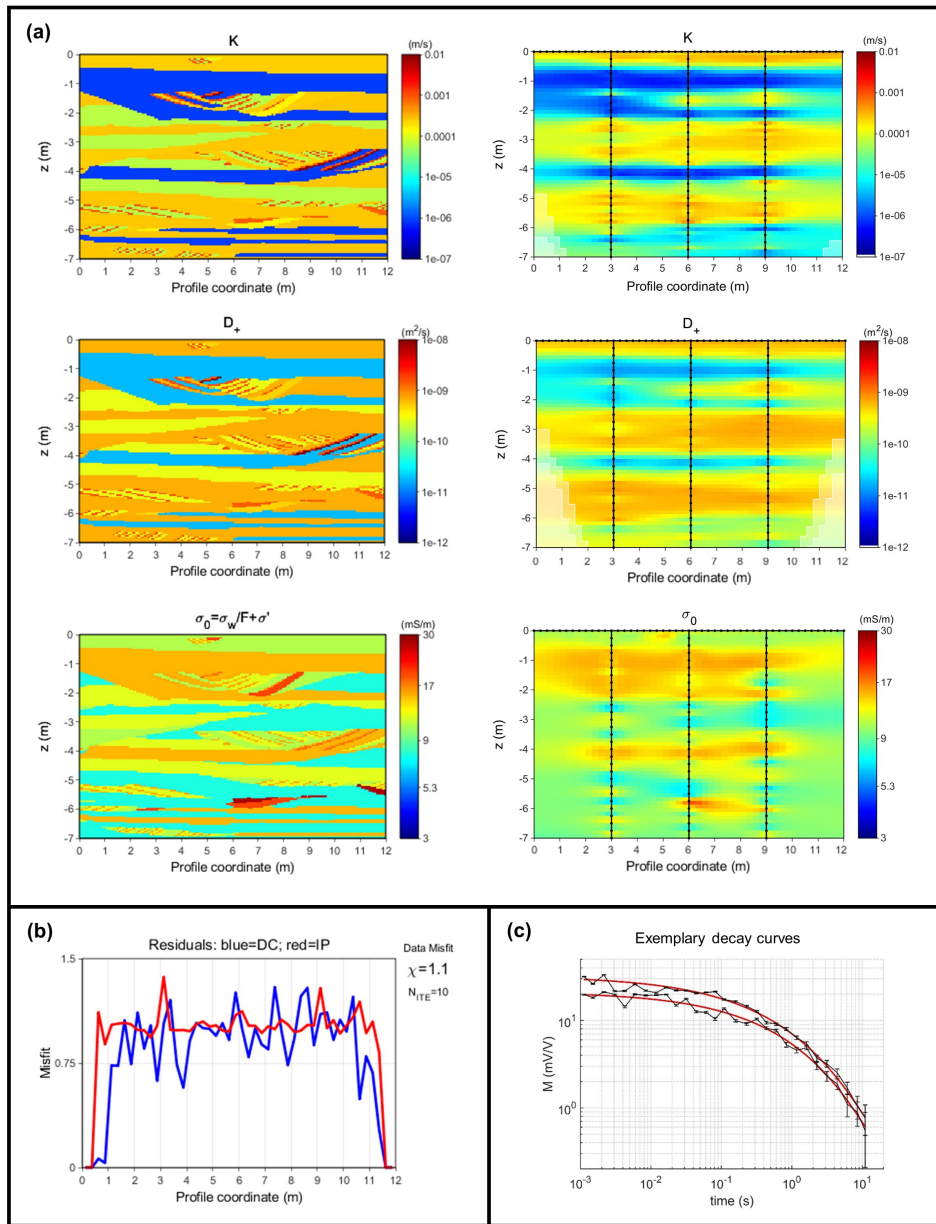
Appendix

A.1 Strategy of the exponential calibration



Visualization of the concept of the exponential calibration of IP inversion results by incorporating pumping test data. **(a)** The selection of a suitable ξ -percentile influences the resulting value for α , thereby determining the overall strength and direction of the calibration. **(b)** The function $\alpha(\xi)$ for the three different spacings using $K_{\text{eff}} = 7 \cdot 10^{-5} \text{ ms}^{-1}$ as retrieved from the pumping test data. This plot is typically helpful to find a reasonable value for ξ . It should usually be higher for larger electrode spacings (e.g., green line - 1 m spacing) since smoothing effects lead to more extensive areas of low K . **(c)** Setup of pumping tests for the derivation of K_{eff} . The source-receiver combinations used for this procedure are a subset of the full HT data set. **(d)** The dependence of C_α on the respective K -values of the inversion result, visualizing the exponential law inspired by the strength of the IP signal and the effect of different α -values.

A.2 Full forward model and IP inversion result



(a) Left part: Bolstern aquifer analog data including the parameters hydraulic conductivity K , diffusion coefficient D_+ and total electrical conductivity σ_0 as a combination of water conductivity σ_w , formation factor F and the real part of interface conductivity σ'_{int} . The frequency exponent c is assumed to be homogeneous and is therefore not shown here. The forward modeling was performed in the Why-CDF model space. Right part: IP inversion result, performed in the ThyCD model space with 0.25 m electrode spacing. The transparent parts (lower corners) indicate areas with low sensitivity. **(b)** Misfit of the inversion result along the whole profile. The misfits of the DC data (blue line) and the IP data (red line) end up to be very balanced and the overall data misfit $\chi = 1.1$ indicates that after the inversion the data are fitted closely to the noise level. The final result was achieved after ten iterations. **(c)** Exemplary decay curves of the forward simulation with added Gaussian noise (black lines) including error bars of the assumed standard deviation model and fitted decay curves of the inversion result (red lines).

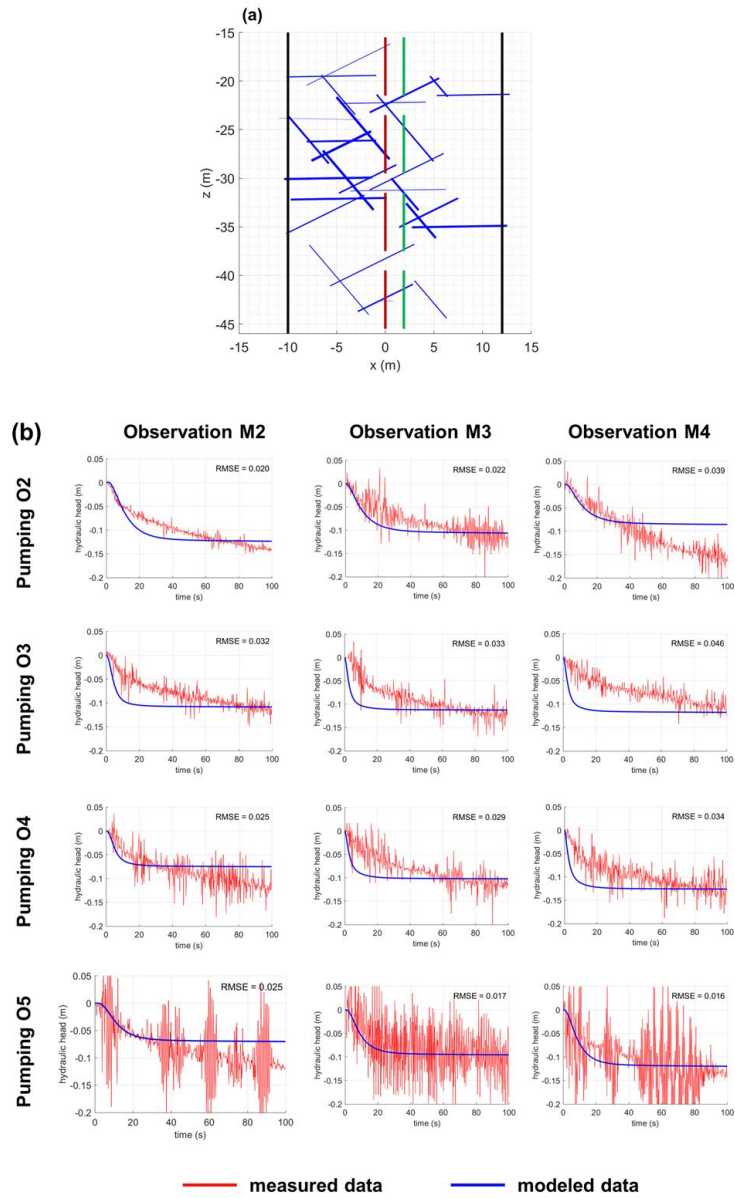
A.3 Supporting Information on Römhild et al. (2024a)

The following supporting information show results of the hybrid DFN inversion with an alternative matrix permeability of $K = 10^{-8}$ m/s (S1), as well as results from a pure DFN inversion neglecting matrix permeability (S2). This information mainly refers to section 3.3.4 of this thesis and was originally published as online supporting information for (Römhild et al., 2024a).

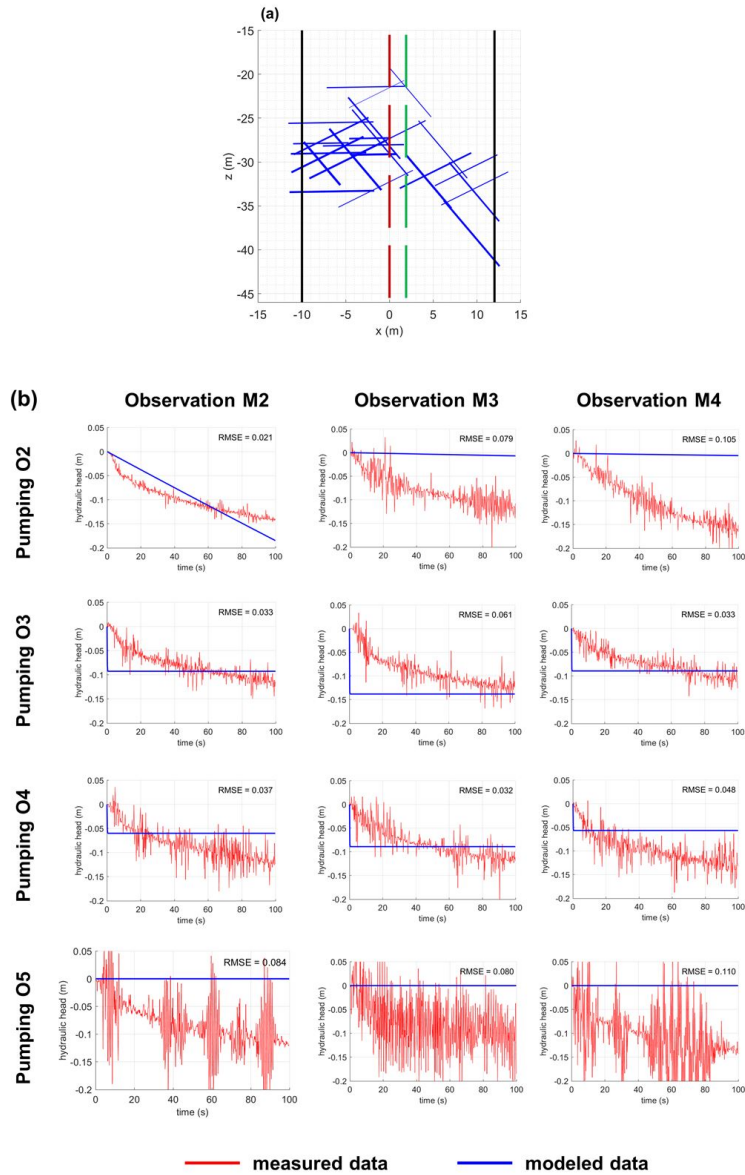
For both of these inversion cases, the misfit between measured and modeled data had remained almost constant for several thousands of iterations. It is thereby ensured that a stationary level had been reached and no better fit is possible, meaning that the shown DFN realization must be part of the posterior ensemble.

We show that although a different matrix permeability actually produces seemingly reasonable DFN realizations, the data cannot be fitted with the same accuracy (higher overall RMSE), and therefore the inversion results are characterized by a lower likelihood compared to the main results shown in the paper.

When neglecting matrix permeability completely, it is not possible to fit the measured data with reasonable accuracy at all. This shows that a classical DFN inversion is not suitable for this data set, and that the hybrid DFN inversion approach is necessary for this site, and probably at other fractured-porous field sites.



S1: Hybrid DFN inversion result for hydraulic conductivity of the matrix of $K = 10^{-8}$ m/s. **(a)** Fracture set of the last iteration of the inversion - similar to Figure 3.3a in the main manuscript. **(b)** Measured (raw) data of the HT experiments (red lines) and modeled pressure response curves for the last iteration of the inversion (blue lines) - similar to Figure 3.4 in the main manuscript.



S2: DFN inversion result neglecting matrix permeability. **(a)** Fracture set of the last iteration of the inversion - similar to Figure 3.3a in the main manuscript. **(b)** Measured (raw) data of the HT experiments (red lines) and modeled pressure response curves for the last iteration of the inversion (blue lines) - similar to Figure 3.4 in the main manuscript.

The original supporting information is available through the online version of (Römhild et al., 2024a).

Acknowledgements

First of all, I would like to thank my supervisor Peter Bayer for giving me the opportunity to work on these topics, for his valuable ideas and feedback, and for keeping me motivated throughout the years of my PhD project.

I am also very grateful to Gianluca Fiandaca for sharing all of his research ideas, his enthusiasm, his inversion codes, and hence for becoming my second supervisor. I would also like to thank him, and all of his colleagues and students at the University of Milan for their great hospitality during my visits.

Furthermore, I want to thank my other co-authors Lisa Maria Ringel, Linwei Hu, Quan Liu, Thomas Ptak, and Laura Meyer for all their contributions to this work. In addition, there are lots of other people who have been very kind in sharing their knowledge and giving me helpful tips and feedback on different occasions. In particular, I would like to thank Márk Somogyváry for his introduction to hydraulic tomography, Thomas Günther for solving some pygimli issues for me, and Andreas Weller for his insightful criticism and for sharing his IP-related knowledge and experience.

I am also more than happy to have the pleasure of working together with great colleagues and friends in our working group at MLU Halle. These are: Julia Becher, Christoph Bott, Andreas Englert, Hannah Gebhart, Wolfgang Gossel, Hannes Hemmerle, David Hoffmann, Wiebke Lehmann, Laura Meyer, Hesam Soltan Mohammadi, Maximilian Noethen, Lisa Maria Ringel, and Guanyu Yuan. Plus, I want to thank our secretaries Daniela Rothe and Marie Petzold for their great support in overcoming bureaucratic obstacles.

I am still very thankful to all the people at TU Freiberg who have been, and continue to be, very inspirational for me, in particular Jana Börner, Martin Sonntag, Klaus Spitzer, and Stefan Buske.

Lastly, I would also like to thank the students taking part in my courses over the past five years for giving me the feeling of occasionally being useful despite working on a PhD.

Curriculum vitae

Personal information

- Name: Lukas Römhild
- Date of birth: [REDACTED]
- Place of birth: [REDACTED]

Professional experience

- 01/2020 - Current: **Research Assistant**, Applied Geology, Institute of Geosciences and Geography, Martin-Luther-Universität Halle-Wittenberg, Halle (Saale), Germany

Education

- 01/2020 - Current: **PhD Student**, Applied Geology, Institute of Geosciences and Geography, Martin-Luther-Universität Halle-Wittenberg, Halle (Saale), Germany.
- 10/2016 - 02/2019: **M.Sc. Geophysics**, TU Bergakademie Freiberg, Germany. *Thesis: Petrophysical Characterization of Highly Polarizable Rocks from the Moffat Shale Group (Ireland)*
- 10/2013 - 09/2016: **B.Sc. Geoinformatics and Geophysics**, TU Bergakademie Freiberg, Germany. *Thesis: Kleinskalige geoelektrische Kartierung an einem Erzgang in der Reichen Zeche (Freiberg)*
- 07/2013: **Abitur**, Staatliches Gymnasium Arnstadt, Germany.

List of Publications

Peer-reviewed publications

Römhild, L., Fiandaca, G. and Bayer, P. (2024b): Joint inversion of induced polarization and hydraulic tomography data for hydraulic conductivity imaging. *Geophysical Journal International*, 238(2), 960–973. <https://doi.org/10.1093/gji/ggae197>

Römhild, L., Ringel, L.M., Liu, Q., Hu, L., Ptak, T. and Bayer, P. (2024a): Hybrid discrete fracture network inversion of hydraulic tomography data from a fractured-porous field site. *Water Resources Research*, 60, e2023WR036035. <https://doi.org/10.1029/2023WR036035>

Römhild, L., Fiandaca, G., Hu, L., Meyer, L. and Bayer, P. (2022a): Imaging hydraulic conductivity in near-surface aquifers by complementing cross-borehole induced polarization with hydraulic experiments. *Advances in Water Resources*, 170, 104322. <https://doi.org/10.1016/j.advwatres.2022.104322>

Römhild, L., Sonntag, M., Kiyani, D., Rogers, R., Rath, V. and Börner, J.H. (2019): Anisotropic complex electrical conductivity of black shale and mudstone from the Moffat Shale Group (Ireland). *Near Surface Geophysics*, 17, 675–690. <https://doi.org/10.1002/nsg.12073>

Data publications

Römhild, L., Sonntag, M., Kiyani, D., Rogers, R., Rath, V., and Börner, J. H. (2022b): Anisotropic broadband spectral induced polarization (SIP) data of black shale and mudstone from the Moffat Shale Group (Ireland). V. 1.0. *GFZ Data Services*. <https://doi.org/10.5880/fidgeo.2022.034>

Conference contributions

Römhild, L., Fiandaca, G., and Bayer, P. (2024): Tackling petrophysical ambiguities in IP-K relations by joint inversion of hydraulic tomography and induced polarization data. *7th International IP workshop*, Lund, Sweden, 28-30 May.

Römhild, L., Ringel, L.M., Liu, Q., Hu, L., Ptak, T. and Bayer, P. (2024): Inversion of hydraulic tomography data from a fractured-porous field site in Göttingen by a hybrid discrete fracture network model. *29. Tagung der Fachsektion Hydrogeologie e.V. in der DGGV e.V.*, Aachen, Germany, 20-23 March 2024.

Römhild, L., Fiandaca, G., and Bayer, P. (2024): Joint inversion of hydraulic tomography and cross-borehole induced polarization data for hydraulic conductivity imaging. *84. Jahrestagung der Deutschen Geophysikalischen Gesellschaft*, Jena, Germany, 10-14 March 2024.

Römhild, L., Fiandaca, G., and Bayer, P. (2023): Joint Inversion of Induced Polarization and Hydraulic Tomography Data for Imaging Hydraulic Conductivity. *Workshop des Arbeitskreises Induzierte Polarisation der DGG*, Kassel, Germany, 4-5 October 2023.

Römhild, L., Fiandaca, G., and Bayer, P. (2023): Hydraulic conductivity imaging by induced polarization and hydraulic tomography. *30. Schmucker-Weidelt-Kolloquium für Elektromagnetische Tiefenforschung*, St. Marienthal (Ostritz), Germany, 25-29 September 2023.

Römhild, L., Fiandaca, G., Hu, L., and Bayer, P. (2023): Direct inversion of cross-borehole induced polarization data for hydraulic conductivity: Synthetic examples, hydraulic calibration and implications for transport modelling. *83. Jahrestagung der Deutschen Geophysikalischen Gesellschaft*, Bremen, Germany, 5-9 March 2023.

Römhild, L., Fiandaca, G., Hu, L., and Bayer, P. (2022): Imaging hydraulic conductivity by cross-borehole induced polarization - a novel inversion procedure. *Computational Methods in Water Resources*, Gdańsk, Poland, 19-23 June 2022.

Römhild, L., Fiandaca, G., Hu, L., and Bayer, P. (2021): Imaging hydraulic conductivity in near-surface aquifers by cross-borehole Induced Polarization. *48th IAH Congress*, Brussels, Belgium, 6-10 September 2021.

Römhild, L., Börner, J. and Spitzer, K. (2017): Kleinskalige geoelektrische Kartierung an einem Erzgang in der Reichen Zeche (Freiberg). *77. Jahrestagung der Deutschen Geophysikalischen Gesellschaft*, Potsdam, Germany, 27-30 March 2017.

Declaration

Ich erkläre an Eides statt, dass ich die Arbeit selbstständig und ohne fremde Hilfe verfasst, keine anderen als die von mir angegebenen Quellen und Hilfsmittel benutzt und die den benutzten Werken wörtlich oder inhaltlich entnommenen Stellen als solche kenntlich gemacht habe.

I declare under penalty of perjury that this thesis is my own work entirely and has been written without any help from other people. I used only the sources mentioned and included all the citations correctly both in word or content.

Datum / Date

Unterschrift des Antragstellers / *Signature of the Applicant*

